Title:
Clues in the Quest for the Invisible Universe

Author:
Mardon, Jeremy

Acceptance Date:
2011

Series:
UC Berkeley Electronic Theses and Dissertations

Degree:
Ph.D., PhysicsUC Berkeley

Advisor(s):
Nomura, Yasunori

Committee:
Bousso, Raphael, Borcherds, Richard E

Permalink:
http://escholarship.org/uc/item/35q8g6xf

Abstract:

Clues in the Quest for the Invisible Universe

by

Jeremy Mardon

A dissertation submitted in partial satisfaction of the
requirements for the degree of
Doctor of Philosophy
in
Physics
in the
Graduate Division
of the
University of California, Berkeley

Committee in charge:

Professor Yasunori Nomura, Chair
Professor Raphael Bousso
Professor Richard E. Borcherds

Spring 2011

Clues in the Quest for the Invisible Universe

Abstract

Clues in the Quest for the Invisible Universe

by

Jeremy Mardon

Doctor of Philosophy in Physics

University of California, Berkeley

Professor Yasunori Nomura, Chair

The particle nature of dark matter is one of the most longstanding mysteries of particle physics. In this dissertation I study several potential clues, both experimental and theoretical, in the quest to understand this invisible component of the universe. In the last few years, data collected by the PAMELA, ATIC, FERMI and H.E.S.S. experiments has revealed several unexpected features in the fluxes of electron and positron cosmic rays. I investigate an interpretation of these anomalies in terms of dark matter annihilating in our galaxy through a "cascade" into electrons or muons. I find good ability to reproduce the data whilst evading other experimental constraints. Inspired by these anomalies, I also investigate a simple framework for dark matter, with many similarities to QCD and well motivated in the context of dynamical solutions to the hierarchy problem. In this framework dark matter decays to standard model particles through a cascade, and I again find that it can provide an excellent fit to cosmic-ray data whilst evading other constraints. I consider the implications at the LHC and in future gamma-ray measurements.

More generally, astrophysical and cosmological considerations have a strong interplay with models of physics Beyond the Standard Model and their implications for collider experiments. I investigate the cosmology of the "Goldstini" framework in this context. I find that the tensions seen in standard gravitino cosmology are relaxed, and that either gravitinos or goldstinos may be dark matter. I also find that such cosmologically preferred theories may also have the most striking signatures at colliders. The LHC has the potential to observe a "smoking gun" signal, in which the Goldstini framework is unambiguously confirmed.

Contents

List of Figures

List of Tables

Acknowledgments

I am immensely grateful to my advisor, Yasunori Nomura, whose guidance and mentorship have put me in the wonderful position I am now in, and whose style and taste in physics continue to be an inspiration to me. Many thanks. It has been a great pleasure working with all my other collaborators; Dan, Cliff, Jesse and Tomer, you guys are great fun as well as great physicists. Thanks to John March-Russell who pointed me towards Berkeley in the first place. Thanks to everyone in the CTP for making it such a great place to be a grad student, and particularly to my office mates Chris, Gilly, Kevin, Dan and David. Beem Machine, you are an unstoppable force for awesomeness. Thanks Mum and Dad for always being so interested in what I do even though it sounds like nonsense. Katie, I'm so happy that you can make sense of it when I tell you about my research. Thanks, I really mean it.

Chapter 1

Introduction

Dark matter lays a strong claim to being the most outstanding mystery in particle physics. Despite overwhelming astrophysical evidence for its existence, and concerted efforts to observe it scattering with nuclei in direct-detection experiments, evidence of its particle properties remains elusive. Indeed, all that is known of its particle properties are those that are excluded by observation: it does *not* consist of Standard Model particles, it is *not* charged or strongly interacting, it has *not* been seen to interact with itself, it has *not* been observed in colliders, it does *not* scatter elastically by Z-boson exchange, etc. One of the main hopes for observing the particle nature of dark matter lies in indirect detection – the observation of the annihilation or decay products of dark matter in our galaxy. Another is the possibility that discoveries at collider experiments, combined with strongly motivated theoretical models, will allow an inference of the cosmological abundance of new invisible particles, and hence an understanding of dark matter. In this dissertation I pursue developments in both of these avenues of investigation.

In the last few years, data collected by the PAMELA [5], ATIC [6], FERMI [86] and H.E.S.S. [42, 87] experiments has revealed several unexpected features in the fluxes of electron and positron cosmic rays. The coincidence of these anomalous observations points to a possible interpretation in terms of annihilation[9, 10, 11, 12, 13] or decay [8] of dark matter in our galaxy. In chapter 2 I investigate this dark-matter interpretation, analyzing a class of annihilating dark-matter models in which the annihilation "cascades" through light intermediate bosons into standard-model particles. I find this class of models can provide a good explanation for the cosmic-ray anomalies while evading constraints from cosmic antiproton, photon and neutrino measurements. The best agreement with all data is found to be for dark matter that cascade-annihilates into electrons, providing an indirect glimpse into the possible nature of the dark-matter sector. This work was carried out in collaboration with Yasunori Nomura, Daniel Stolarski and Jesse Thaler, and has been previously published in [2].

In chapter 3 I continue my investigation into dark-matter interpretations of the cosmic-ray anomalies. In particular, consideration of the high energy scale (a few TeV) and broad spectrum of the anomalous fluxes seen by FERMI and H.E.S.S. hints at dark matter with a mass well above the electroweak scale, decaying into standard model particles via a new light boson. Such a setup is far from the usual WIMP paradigm. With this motivation I study another simple framework for dark matter: that dark matter is a composite state, with mass around 10 TeV, arising in a dynamical sector responsible for stabilizing the electroweak scale. In this framework, the stability of dark matter is the result of an accidental symmetry, which is broken by dimension 6 operators. The dark matter consequently decays, with a lifetime naturally of the right size to explain the cosmic ray anomalies. The decay products are the pseudo-Goldstone-bosons of a spontaneously broken $U(1)$ symmetry, and themselves decay into light standard model particles via mixing with the higgs boson. The framework is natural, with all its features having analogues in QCD. It is well motivated in the context of a supersymmetric solution to the hierarchy problem, with a low-scale dynamical supersymmetry-breaking sector to avoid cosmological problems with the gravitino. The mass, lifetime and decay spectrum of dark matter in this framework naturally coincide with those indicated by a dark matter explanation of the cosmic ray anomalies. I analyze this point in detail, and find an excellent ability to reproduce the data whilst avoiding all constraints. I study the possibility that the pseudo-Goldstone-boson decays to muons and may be discovered in the near future at the LHC. I also study the potential gamma-ray signatures that may be seen by the FERMI telescope if the pseudo-Goldstone-boson decays to pions or taus. This work was carried out in collaboration with Yasunori Nomura and Jesse Thaler, and has been previously published in [3].

More generally, astrophysical and cosmological considerations have a strong interplay with models of physics Beyond the Standard Model and their implications for collider experiments. A particularly clear case of this interplay can be seen in the “Goldstini” framework proposed in [134]. In this framework, supersymmetry is independently broken in multiple sequestered sectors. A remarkable result is the existence of many pseudo-Goldstone-fermions, or “goldstini”, which under fairly general assumptions all have a mass equal to twice that of the gravitino, but with potentially much stronger or weaker couplings to standard-model sector particles. A striking consequence is the possibility of observing the decays of charged, long-lived standard-model superpartners to both gravitinos and to goldstinos at colliders. Reconstruction of the masses and lifetimes of the decaying particles, and the masses of their decay products, would allow a stunning verification of the Goldstini setup. In chapter 4 I investigate how the possibility of this observation at the LHC or a future collider is affected by the cosmology of the Goldstini framework. I find that in this framework, the tensions seen in standard gravitino cosmology are relaxed, with a reheating temperature as high at 10^9 GeV allowed, consistent with thermal leptogenesis, and that either gravitinos or goldstinos may be dark matter. I also find that such cosmologically safe theories may also give rise to the most striking signatures at colliders.

The LHC has the potential to observe a “smoking gun” signal, in which the Goldstini framework is confirmed. This work was carried out in collaboration with Cliff Cheung, Yasunori Nomura and Jesse Thaler, and has been previously published in [4].

Chapter 2

Dark Matter Signals from Cascade Annihilations

2.1 Introduction

Recent observations by PAMELA [5] and ATIC [6] strongly suggest a new primary source of galactic electrons and positrons. Three leading interpretations of the PAMELA/ATIC excesses are astrophysical sources [7], decay of dark matter [8], and annihilation of dark matter [9, 10, 11, 12, 13]. While the current PAMELA/ATIC data cannot distinguish between these possibilities, one expects that the correct scenario will ultimately be determined with the help of complementary data from synchrotron, gamma ray, and neutrino telescopes, as well as collider and direct detection experiments.

One piece of data that points toward an annihilation interpretation is the WMAP Haze [14], an apparent excess of synchrotron radiation coming from the galactic center. Dark matter annihilation into charged particles is uniquely positioned to explain the Haze [15, 16]. If n is the dark matter number density near the galactic center, then the synchrotron signal for dark matter annihilation scales like n^2, while the signal for dark matter decay scales only as n. (Astrophysical signals also roughly scale like n.) Given the normalization of the PAMELA/ATIC excess, the n^2 scaling is favored to explain the size of the Haze anomaly [17].

On the other hand, the same n^2 versus n logic implies that the dark matter annihilation interpretation is more strongly constrained by the *absence* of gamma ray or neutrino excesses from the galactic center. While these constraints are dependent on the Milky Way dark matter halo profile, there are already strong bounds on the annihilation interpretation for strongly peaked halos [18, 19, 20, 21, 22]. Therefore, it is worth exploring dark matter annihilation scenarios in detail to understand how robust the tension is between explaining PAMELA/ATIC/Haze and satisfying other bounds.

Given the absence of anti-proton [23] or gamma ray [24, 25, 26] excesses, the dark matter annihilation scenarios favored to explain PAMELA/ATIC involve annihilation into electrons and muons. However, dark matter need not annihilate into leptons directly. There are a variety of "cascade annihilation" models where dark matter annihilates into light resonances which in turn decay into electrons or muons. These light resonances can lead to nonperturbative enhancements [27, 28] of the dark matter annihilation rate in the galactic halo, providing the large boost factors necessary to explain PAMELA/ATIC [9, 10, 11]. Also, annihilation into light fields gives a kinematic explanation for why dark matter annihilation preferentially yields light leptons [16, 10, 11]. Previous studies of cascade annihilation models appear in Refs. [12, 20].

In the present context, these cascade annihilation scenarios are interesting because they have the potential to explain PAMELA/ATIC while weakening constraints from gamma rays, as measured by atmospheric Cerenkov telescopes like H.E.S.S. [24, 25, 26]. The reason is that gamma ray experiments are directly sensitive to the primary injection spectra, and cascade annihilations yield softer and smaller injection spectra of gamma rays from final state radiation (FSR). PAMELA/ATIC sees electrons and positrons through the filter of charged cosmic ray transport, a process which introduces large uncertainties. Considering also the uncertainties in the highest energy ATIC data, we find that softer spectra of primary leptons can still explain the PAMELA/ATIC excesses.

For cascade annihilations that terminate in muons, there is also an irreducible source of galactic neutrinos, which can be observed as an upward-going muon flux on earth, for example, by water Cerenkov detectors like Super-Kamiokande (Super-K) [29]. While cascades soften the neutrino spectrum, we will see that the final constraints from neutrinos are rather insensitive to the number of cascade steps, and may provide the most robust bound on muon cascade scenarios.

The organization of this chapter is as follows. In the next section, we define our framework for analyzing signals of dark matter through cascade annihilations, with details of the cascade energy spectra given in Appendix A. In Section 2.3, we find the best fit dark matter masses and annihilation cross sections for various cascade scenarios given the PAMELA/ATIC data. We consider H.E.S.S. gamma ray bounds from FSR in Section 2.4 and Super-K neutrino bounds in Section 2.5. In Section 2.6, we study a particular cascade annihilation scenario called the axion portal [11], and present a less constrained "leptonic" version in Appendix B. Conclusions are given in Section 2.7.

2.2 Cascade Annihilations

If dark matter is a thermal relic, then it will have at least one annihilation mode into standard model fields, since in the early universe, the dark matter annihilation

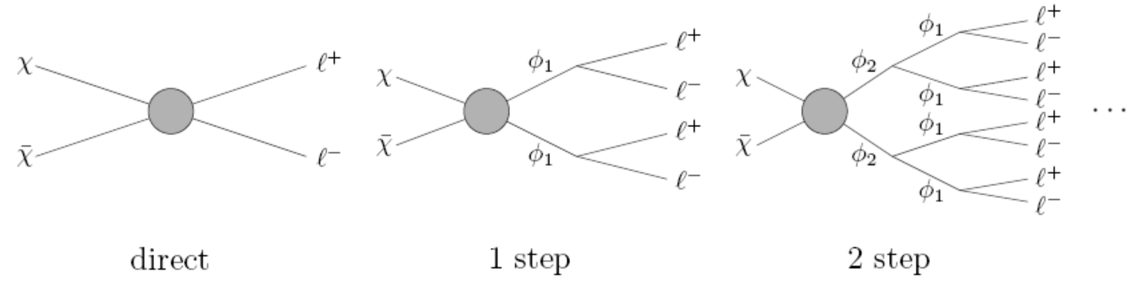

Figure 2.1: For an n-step cascade annihilation, dark matter χ annihilates into $\phi_n\phi_n$. The cascade annihilation then occurs through $\phi_{i+1} \to \phi_i\phi_i$ $(i = 1, \cdots, n-1)$, and in the last stage, ϕ_1 decays into standard model particles. The represents the cases where $\phi_1 \to \ell^+\ell^-$.

channels keep dark matter in thermal equilibrium with the standard model until freezeout. However, dark matter need not annihilate into standard model particles directly; it can annihilate into new (unstable) resonances which in turn decay into standard model fields. As long as the new resonances are sufficiently broad, then dark matter will be in close enough thermal contact with the standard model for a freezeout calculation to be valid.

These "cascade annihilations" can occur in one or more steps, as shown in Figure 2.1, and there are a variety of motivations for such cascade scenarios. Since the direct coupling between dark matter and the standard model can be small while still achieving the desired thermal relic abundance, such models can have reduced direct detection cross sections compared to generic weakly interacting massive particles (WIMPs) [30]. Cascade annihilations can arise whenever new light resonances have large couplings to dark matter, such as in exciting dark matter [31]. In the context of PAMELA/ATIC, there has been interest in using light resonances to provide large enhancement to the galactic annihilation rate through the Sommerfeld effect or bound state (WIMPonium) formation [9, 10, 11]. These light resonances can also explain the lepton-richness of dark matter annihilation through kinematic thresholds [10, 11].

Cascade annihilations give softer primary spectra for the annihilation products than direct annihilation. As reviewed in Appendix A, for (scalar) cascade annihilations involving well-separated kinematic scales, the approximate primary spectra can be calculated using a simple convolution formula. The energy spectra are conveniently parametrized in terms of the energy fraction $x_n \equiv E_n/m_{\rm DM}$, where E_n is the final state energy after the n-th step of the cascade, and $m_{\rm DM}$ is the dark matter mass. If $d\tilde{N}/dx_0$ is the normalized primary spectrum from direct annihilation, then the normalized primary spectrum from a 1-step annihilation $d\tilde{N}/dx_1$ is

$$\frac{d\tilde{N}}{dx_1} \approx \int_{x_1}^{1} \frac{dx_0}{x_0}\, \frac{d\tilde{N}}{dx_0}. \tag{2.1}$$

This convolution formula can be iterated to obtain the normalized primary spectrum for an n-step cascade scenario. Eq. (2.1) is also reasonably representative of non-scalar cascades, since indirect detection measurements are unpolarized.

While cascade annihilations give softer spectra, they typically yield a higher multiplicity of annihilation products. The final primary spectrum dN/dx_n must take into account the multiplicity of annihilation products per dark matter annihilation, and in a typical n-step cascade, the final state multiplicity scales like 2^n.

An important exception, however, is in cases involving singularities, where cascade annihilations yield both a softer spectrum *and* a lower multiplicity. For example, FSR from charged leptons has a collinear singularity that is regulated by the lepton mass. Integrating over the singularity gives a photon spectrum dN_γ/dx that is proportional to $\ln Q/m_\ell$, where Q is the total energy available for radiation. For direct annihilation $Q \simeq 2m_{\rm DM}$, while for cascade annihilations $Q \simeq m_1$, where m_1 is the mass of the resonance in the last stage of the annihilation $\phi_1 \to \ell^+\ell^-$. Light enough ϕ_1 fields can give a dramatic reduction in the $\ln Q/m_\ell$ factor and thus the FSR photon yield.

In this chapter, we only consider cascade annihilations that terminate in electrons or muons. The same analysis, however, could be repeated for charged pions or taus by changing the direct annihilation spectra. We expect the results for an n-step charged pion cascade to be similar to an $(n+1)$-step muon cascade. Cascades involving taus will face stronger gamma ray bounds because of the $O(1)$ fraction of π^0s in tau decays. For simplicity, we only show plots for direct, 1-step, and 2-step cascades.

2.3 PAMELA/ATIC Spectra

The PAMELA satellite experiment [32] observed an anomalous source of galactic positrons in the energy range 10–100 GeV through a measurement of the positron fraction $\Phi_{e^+}/(\Phi_{e^+} + \Phi_{e^-})$ [5]. The ATIC balloon experiment [33] is not capable of charge separation, but observed a peak in the total electron plus positron flux between 100–1000 GeV in a $(\Phi_{e^+} + \Phi_{e^-})$ measurement [6]. Intriguingly, both excesses can be described by a single new source of galactic electrons and positrons, and here we study the goodness of fit for dark matter cascade annihilations. The primary electron/positron spectra for n-step electron and muon cascade annihilations are given in Appendices A.0.1 and A.0.2. Once the primary spectrum is known and a dark matter halo profile assumed, we can propagate the electrons and positrons through the Milky Way and compare with the PAMELA/ATIC data.

We follow the analysis of Ref. [34], which assumes that galactic electrons and positrons can be described by a diffusion-loss process. In the turbulent galactic magnetic fields, electrons/positrons diffuse within a fiducial region around the galactic disk and escape the galaxy outside that region. An energy loss term incorporates the physics of inverse Compton scattering (ICS) and synchrotron radiation. Dark matter annihilation is represented by a source term proportional to the square of the dark

	R (kpc)	L (kpc)	K_0 (kpc^2/Myr)	δ	τ_E (sec)
MED	20	4	0.0112	0.70	10^{16}
M1	20	15	0.0765	0.46	10^{16}
M2	20	1	0.00595	0.55	10^{16}

Table 2.1: Diffusion-loss parameters for the three benchmark models (MED, M1, and M2) for electron/positron propagation.

matter halo density. Since the energy loss time is much shorter than the age of the galaxy, the electron/positron system is assumed to be in steady state.

Taking $\psi_{e^-}(\vec{x}, E)$ to be the galactic electron number density per unit energy, the diffusion-loss equation is

$$K_0\, \varepsilon^\delta\, \nabla^2 \psi_{e^-}(\vec{x}, E) + \frac{\partial}{\partial \varepsilon}\left(\frac{\varepsilon^2}{\tau_E}\, \psi_{e^-}(\vec{x}, E)\right) + q(\vec{x}, E) = 0, \tag{2.2}$$

where $\varepsilon = E/\text{GeV}$, K_0 and δ parametrize the (energy dependent) diffusion, τ_E is a characteristic energy loss time, and $q(\vec{x}, E)$ is the electron source term for dark matter annihilations. The same equation also holds for the positron number density per unit energy $\psi_{e^+}(\vec{x}, E)$. The electron/positron densities $\psi_{e^-/e^+}(\vec{x}, E)$ are assumed to have vanishing boundary conditions on the surface of a cylinder of height $2L$ and radius R. We consider the three benchmark models from Ref. [34], which are summarized in Table 2.1.

The electron/positron source term is given by

$$q(\vec{x}, E) = \frac{1}{2\eta}\langle \sigma v \rangle \left(\frac{\rho(\vec{x})}{m_{\text{DM}}}\right)^2 \frac{dN_e}{dE}, \tag{2.3}$$

where $\rho(\vec{x})$ is an assumed dark matter halo profile, m_{DM} is the dark matter mass, $\langle \sigma v \rangle$ is the average dark matter annihilation cross section in the galactic halo, and dN_e/dE is the electron energy spectrum per dark matter annihilation. $\eta = 1$ if dark matter is self-conjugate (e.g. a Majorana fermion), while $\eta = 2$ if not (e.g. a Dirac fermion). We consider three spherically symmetric benchmark halo profiles (cored isothermal [35], NFW [36], and Einasto [37]) with $r_\odot = 8.5$ kpc and $\rho_\odot = 0.3$ GeV cm^{-3}:

$$\rho(r)_{\text{Isothermal}} = \rho_\odot \frac{1 + (r_\odot/r_c)^2}{1 + (r/r_c)^2}, \qquad r_c = 5 \text{ kpc}, \tag{2.4}$$

$$\rho(r)_{\text{NFW}} = \rho_\odot \frac{r_\odot}{r}\left(\frac{1 + r_\odot/r_c}{1 + r/r_c}\right)^2, \qquad r_c = 20 \text{ kpc}, \tag{2.5}$$

$$\rho(r)_{\text{Einasto}} = \rho_\odot \exp\left\{-\frac{2}{\alpha}\left[\left(\frac{r}{r_c}\right)^\alpha - \left(\frac{r_\odot}{r_c}\right)^\alpha\right]\right\}, \qquad \alpha = 0.17, \quad r_c = 20 \text{ kpc}. \tag{2.6}$$

N-body simulations suggest that Einasto and NFW are more realistic profiles for $r \gtrsim 1$ kpc. Within the inner region, however, there is considerable uncertainty, and we include the cored isothermal profile to explore the possibility of a less peaked distribution.

Once the source term is specified, Eq. (2.2) can be solved using the methods of [34, 38], and the electron/positron intensities (fluxes per energy per solid angle) at the earth due to dark matter annihilations are given by

$$\frac{d\Phi^{(\mathrm{DM})}_{e^-/e^+}}{dE\,d\Omega}(E) = \frac{B_{e,\mathrm{astro}}}{4\pi}\psi_{e^-/e^+}(\vec{x}_\odot, E), \tag{2.7}$$

where $\vec{x}_\odot$ is the location of the solar system and $B_{e,\mathrm{astro}}$ is an astrophysical boost factor. Since the annihilation rate is proportional to the squared density of dark matter ρ^2_{DM}, clumping of dark matter tends to increase the local electron/positron flux, and the $B_{e,\mathrm{astro}}$ factor accounts for differences from the assumed smooth halo profile, as well as uncertainties in $\rho_\odot$. Of course, in the presence of clumpiness, the true electron/positron spectrum is also modified [39].

Galactic cosmic rays are a known source of background primary electrons. Background secondary electrons and positrons arise, e.g., from collisions of cosmic ray protons with interstellar gas. In principle, the spectra of background electrons/positrons are correlated with the diffusion-loss parameters for electrons/positrons, but for simplicity we will use the parameterization of background primaries and secondaries from Ref. [40]:

$$\frac{d\Phi^{(\mathrm{prim})}_{e^-}}{dE\,d\Omega} = \frac{0.16\,\varepsilon^{-1.1}}{1 + 11\,\varepsilon^{0.9} + 3.2\,\varepsilon^{2.15}}\ \mathrm{GeV}^{-1}\,\mathrm{cm}^{-2}\,\mathrm{s}^{-1}\,\mathrm{sr}^{-1}, \tag{2.8}$$

$$\frac{d\Phi^{(\mathrm{sec})}_{e^-}}{dE\,d\Omega} = \frac{0.70\,\varepsilon^{0.7}}{1 + 110\,\varepsilon^{1.5} + 600\,\varepsilon^{2.9} + 580\,\varepsilon^{4.2}}\ \mathrm{GeV}^{-1}\,\mathrm{cm}^{-2}\,\mathrm{s}^{-1}\,\mathrm{sr}^{-1}, \tag{2.9}$$

$$\frac{\Phi^{(\mathrm{sec})}_{e^+}}{dE\,d\Omega} = \frac{4.5\,\varepsilon^{0.7}}{1 + 650\,\varepsilon^{2.3} + 1500\,\varepsilon^{4.2}}\ \mathrm{GeV}^{-1}\,\mathrm{cm}^{-2}\,\mathrm{s}^{-1}\,\mathrm{sr}^{-1}, \tag{2.10}$$

where again $\varepsilon = E/\mathrm{GeV}$. To treat background uncertainties, we will marginalize over the normalization and overall slope of the background in our analysis:

$$\Phi^{(\text{back. fit})}_{e^-} = A_-\varepsilon^{P_-}\left(\Phi^{(\mathrm{prim})}_{e^-} + \Phi^{(\mathrm{sec})}_{e^-}\right), \qquad \Phi^{(\text{back. fit})}_{e^+} = A_+\varepsilon^{P_+}\left(\Phi^{(\mathrm{sec})}_{e^+}\right), \tag{2.11}$$

where we allow $0 < A_\pm < \infty$, $-0.05 < P_\pm < 0.05$, as in [9].

In the limit that Eq. (2.1) holds, any given dark matter cascade topology has just two free parameters: the dark matter mass m_{DM} and the annihilation cross section $\langle\sigma v\rangle$. Following the literature, we normalize the cross section to the value that leads to the right relic thermal abundance $\langle\sigma v\rangle_0 \simeq 3 \times 10^{-26}\,\eta\,\mathrm{cm}^3\,\mathrm{s}^{-1}$ and express our results in terms of an effective boost factor

$$B = B_{e,\mathrm{astro}}\frac{\langle\sigma v\rangle}{\langle\sigma v\rangle_0}, \tag{2.12}$$

	Direct e	1 step e	2 step e	Direct μ	1 step μ	2 step μ
Isothermal	16%	17%	9.8%	12%	8.5%	7.7%
NFW	13%	17%	9.4%	12%	7.7%	7.9%
Einasto	9.0%	18%	8.8%	12%	7.1%	8.1%

Table 2.2: The p-value for the best propagation model for each plot in Figures 2.2 and 2.3.

which includes both the deviation from the naive thermal freezeout cross section and dark matter clumping. Using only the statistical error bars, we perform a chi-squared fit of the derived electron/positron intensities to the PAMELA $e^+/(e^+ + e^-)$ and ATIC $e^+ + e^-$ data, treating $m_{\rm DM}$ and B as free parameters. We use only $E \gtrsim 10$ GeV bins for the PAMELA data, as the lower energy bins are strongly affected by solar modulation effects (see the discussion in [5]).

The results of the fit for direct, 1-step, and 2-step annihilations are shown in the case of electron final states in Figure 2.2 and muon final states in Figure 2.3. (The results do not depend on whether the dark matter particle is self-conjugate or not.) Each plot corresponds to a definite cascade annihilation pattern with a definite halo profile, and shows 1σ and 2σ contours for three propagation models in the $m_{\rm DM}$-B plane. The best fit values for $m_{\rm DM}$ and B, as well as the χ^2 values, are also given, where χ^2 follows the chi-squared distribution with 22 degrees of freedom (7 PAMELA + 21 ATIC − 6 fitting parameters: $m_{\rm DM}, B, A_\pm, P_\pm$). To evaluate goodness of fit, we also give p-values in Table 2.2, where we have chosen the propagation model giving smallest χ^2 for each plot of Figures 2.2 and 2.3. As we can see, the fits are reasonable for all the cases presented.

In Figures 2.4 and 2.5, we show the comparisons of the $e^\pm$ intensities with the PAMELA and ATIC data in the cases of electron and muon final states. Solid, dashed, and dotted lines represent direct, 1-step, and 2-step annihilations, and we have chosen the NFW halo profile and the MED propagation model for illustrative purposes. We clearly see the trend that more steps in cascades lead to flatter $e^\pm$ spectra, but that the fits are good for all cases shown. Note that we have not optimized the propagation model here. Adjusting the propagation model can lead to a better fit in certain cases, especially the 2-step annihilation into $\mu^+\mu^-$.

Summarizing the analysis of the $e^\pm$ data, we find:

- The PAMELA and ATIC data require the dark matter mass and boost factor in the region $m_{\rm DM} = O(\text{TeV})$ and $B = O(1000)$, which is consistent with earlier analyses on the direct [9] and 1-step [12] cases. More steps in the cascade lead to larger values of $m_{\rm DM}$ and B, and roughly speaking, both B and $m_{\rm DM}$ scale as 2^n. The reason is that the peak location in the ATIC data sets the scale for the final state $e^\pm$ energy, and since the average $e^\pm$ energy over $m_{\rm DM}$ in an n-step

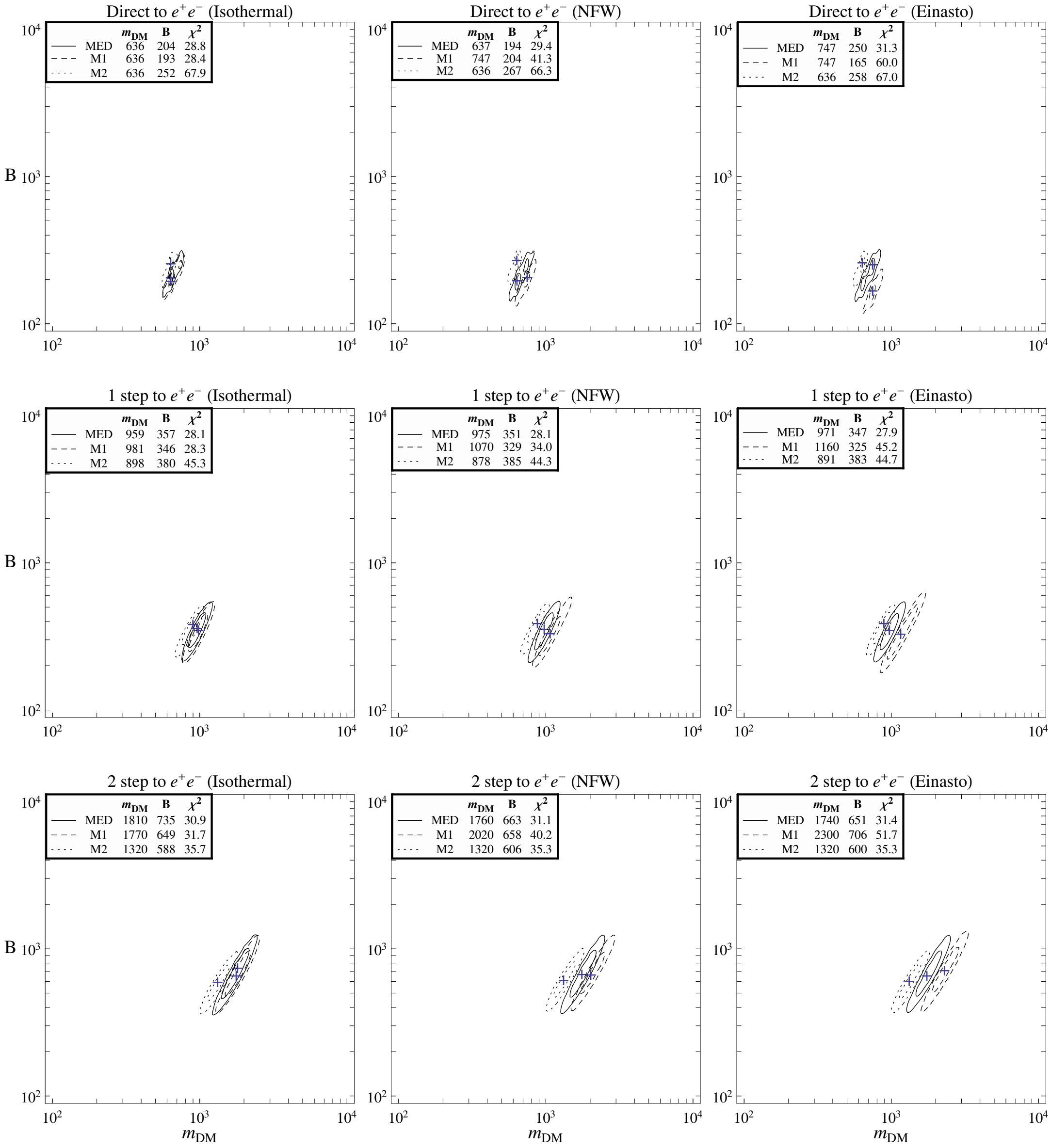

Figure 2.2: The best fit regions for the dark matter mass m_{DM} and boost factor B in the cases of direct, 1-step, and 2-step annihilations into e^+e^- for different halo profiles and propagation models. The best fit values are indicated by the crosses, and the contours are for 1σ and 2σ.

		$m_{\rm DM}$	B	χ^2
—	MED	1410	1580	29.8
– –	M1	1410	1460	30.1
···	M2	1140	1360	42.2

		$m_{\rm DM}$	B	χ^2
—	MED	1410	1500	29.8
– –	M1	1590	1450	35.6
···	M2	1140	1430	41.3

		$m_{\rm DM}$	B	χ^2
—	MED	1400	1460	29.8
– –	M1	1840	1630	46.5
···	M2	1140	1390	41.6

		$m_{\rm DM}$	B	χ^2
—	MED	2410	2710	31.6
– –	M1	2540	2730	32.6
···	M2	1870	2460	34.3

		$m_{\rm DM}$	B	χ^2
—	MED	2550	2850	32.0
– –	M1	2940	2850	41.7
···	M2	1850	2530	34.0

		$m_{\rm DM}$	B	χ^2
—	MED	2510	2750	32.4
– –	M1	3410	3160	53.4
···	M2	1870	2510	34.0

		$m_{\rm DM}$	B	χ^2
—	MED	4370	5110	34.9
– –	M1	4440	4890	36.9
···	M2	3140	4370	32.0

		$m_{\rm DM}$	B	χ^2
—	MED	4370	4890	35.8
– –	M1	5480	5560	47.9
···	M2	3480	5380	31.9

		$m_{\rm DM}$	B	χ^2
—	MED	4370	4890	36.6
– –	M1	6150	5830	59.8
···	M2	3480	5230	31.8

Figure 2.3: The same as Figure 2.2 but for annihilations into $\mu^+\mu^-$.

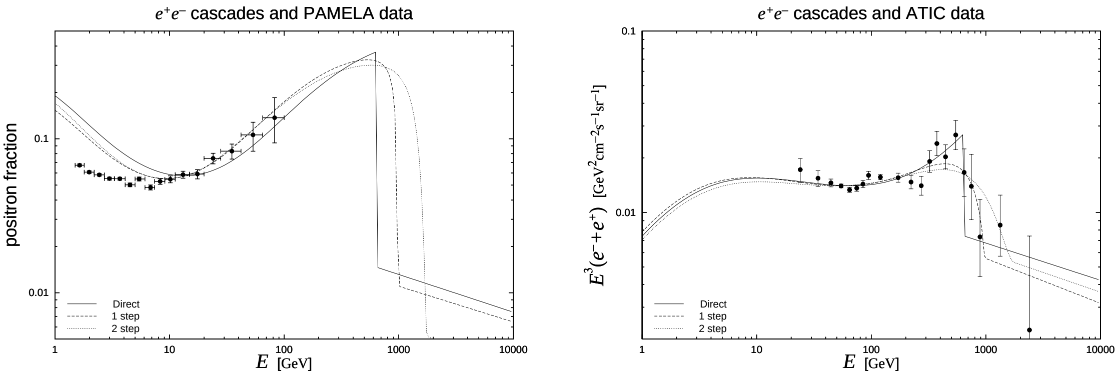

Figure 2.4: The predicted $e^{\pm}$ intensities compared to the PAMELA (left) and ATIC (right) data for direct (solid), 1-step (dashed), and 2-step (dotted) annihilations into electron final states. The NFW halo profile and the MED propagation model are chosen, and the $e^{\pm}$ backgrounds are marginalized as described in Eq. (2.11). Note that we fit the PAMELA data only for $E \gtrsim 10$ GeV because solar modulation effects are important at lower energies.

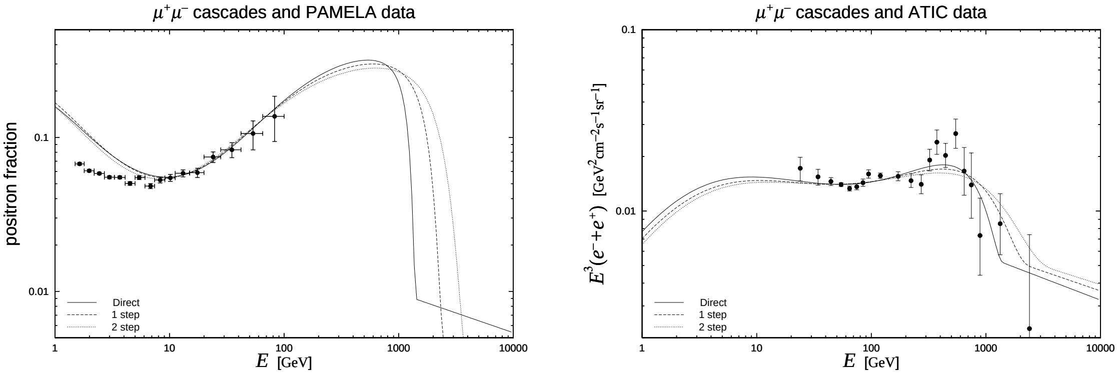

Figure 2.5: The same as Figure 2.4 but for annihilations into muon final states.

cascade scales like $1/2^n$, $m_{\rm DM}$ must increase by 2^n to keep the peak location fixed. Similarly, the annihilation signal scales like $BN_e/m_{\rm DM}^2$ (assuming fixed $\rho_{\rm DM}$), where $N_e = 2^{n+1}$ is the final state $e^\pm$ multiplicity. Thus, to keep the PAMELA/ATIC rate fixed, B must scale like 2^n.

- The fits do not become much worse by going to multiple steps, due to uncertainties in the highest energy ATIC data and uncertainties in the $e^\pm$ propagation model. In particular, 2-step annihilations still fit the data reasonably well for both electron and muon final states. The required boost factors are rather large in the case of muon final states: B of a few thousand. Such large boost factors may come from both astrophysics, e.g. uncertainties in $\rho_\odot$ and nearby clumps of dark matter, and particle physics.
- Uncertainties in halo profiles and propagation models do not significantly affect the dark matter mass and the boost factor. Errors from these uncertainties are mostly of $O(10\%)$ and at most a factor of 2. The 2σ ranges of the fits then determine $m_{\rm DM}$ and B up to a factor of a few.

Recent measurements at H.E.S.S. [41] of the electron plus positron flux above 600 GeV [42] are qualitatively consistent with the ATIC spectrum. Given the large systematic energy uncertainties and hadronic background, we do not use the H.E.S.S. data in our fits, although we remark that the observed steepening of the spectrum places some bounds on very long cascade decays and may disfavor spectra with a hard cutoff such as direct $e^\pm$ annihilation.

2.4 Gamma Ray Constraints

When dark matter annihilates into charged leptons, there is a primary source of gamma rays coming from FSR. Various gamma ray telescopes have looked for excess gamma rays coming from the galactic center, and the null result of such searches puts bounds on dark matter annihilation into charged leptons. An additional effect that is beyond the scope of this chapter is ICS, where electrons/positrons from dark matter annihilation lose energy by upscattering starlight photons into gamma rays. The rate of ICS photon production depends on the modeling of galactic starlight, and we here focus only on the bounds from FSR. For an early analysis of FSR in dark matter annihilation, see [43].

There is negligible energy loss as gamma rays propagate from the galactic center to the earth. The total power (flux per energy) on earth depends on the dark matter halo profile through

$$\frac{d\Phi_\gamma}{dE} = \frac{B_{\gamma,\rm astro}}{8\pi\eta\, m_{\rm DM}^2}\langle\sigma v\rangle \bar{J}\Delta\Omega\,\frac{dN_\gamma}{dE}, \tag{2.13}$$

where $B_{\gamma,\rm astro}$ is an astrophysical boost factor for photons that may differ from $B_{e,\rm astro}$, and dN_γ/dE is the photon energy spectrum per dark matter annihilation. The energy

	GC (on)	GC (off)	GC (eff)	GR (on)	GR (off)	GR (eff)
Isothermal	10	10	0.028	10	10	0.019
NFW	$1.1 \cdot 10^4$	$3.6 \cdot 10^2$	$1.1 \cdot 10^4$	$1.8 \cdot 10^3$	$4.3 \cdot 10^2$	$1.4 \cdot 10^3$
Einasto	$5.8 \cdot 10^3$	$7.3 \cdot 10^2$	$5.1 \cdot 10^3$	$2.3 \cdot 10^3$	$8.7 \cdot 10^2$	$1.5 \cdot 10^3$

Table 2.3: $\bar{J}$ values for GC and GR gamma ray observations (on-source, off-source, and effective) in units of $\mathrm{GeV}^2\,\mathrm{cm}^{-6}\,\mathrm{kpc}$.

spectrum from FSR is reviewed in Appendix A.0.3, and we also include the effect of radiative muon decays as described in Appendix A.0.4. $\Delta\Omega$ is the solid angle integration region, and $\bar{J}$ is the average line-of-sight-integrated squared dark matter density for a given halo model

$$\bar{J} = \frac{1}{\Delta\Omega} \int_{\Delta\Omega} d\Omega \int_{\mathrm{line-of-sight}} ds\, \rho(\vec{x})^2. \tag{2.14}$$

The strongest bounds on FSR gamma rays come from atmospheric Cerenkov telescopes, but the way these experiments extract gamma ray signals affects the final dark matter annihilation bounds. To enable background subtraction, these telescopes operate either in on-off mode or wobble mode, meaning the effective $\bar{J}$ exposure is [44]

$$\bar{J}_{\mathrm{eff}} = \bar{J}_{\mathrm{on-source}} - \bar{J}_{\mathrm{off-source}}. \tag{2.15}$$

By definition, $\bar{J}_{\mathrm{eff}}$ is smaller than $\bar{J}_{\mathrm{on-source}}$, and neglecting the $\bar{J}_{\mathrm{off-source}}$ contribution gives bounds that are too aggressive. This means that one must know both the on- and off-source integration regions to derive a bound on the cross section. For shallow dark matter halo profiles, there can be large cancellations in the value of $\bar{J}_{\mathrm{eff}}$, and in principle a stronger bound could be obtained using the raw unsubtracted data.

We set bounds on FSR using three H.E.S.S. gamma ray data sets. The first two are observations of the Galactic Center (GC) [24] and the Galactic Ridge (GR) [25]. Neither is ideal for dark matter observations because of the large contamination from gamma ray point sources and molecular gas, and in principle one should put bounds on a dark matter signal after subtracting both these foregrounds. Since such subtractions are not available, we derive conservative bounds by insisting that the dark matter signal does not exceed any of the H.E.S.S. data points by more than 2σ. For the GC and GR samples, values of $\bar{J}$ for the three dark matter halos in Eqs. (2.4, 2.5, 2.6) are shown in Table 2.3 for both the on-source and off-source regions.

The GC data set comes from the inner 0.1° of the galaxy with a solid angle integration of $\Delta\Omega = 1 \times 10^{-5}$, corresponding to the gamma ray source HESS J1745-290. This sample was taken in wobble mode, and the off-source region corresponds to a ring at a distance of 1.4° from the GC. Apart from the off-source subtraction, no other corrections were made to the data, so the data points include both the HESS J1745-290 point source as well as any putative dark matter signal.

The GR data set comes from the region $|\ell| < 0.8^\circ$, $|b| < 0.3^\circ$ in galactic coordinates, with foreground point sources HESS J1745-290 and $G0.9+0.1$ subtracted. The GR sample was taken in on-off mode, and the region $|\ell| < 0.8^\circ$, $0.8^\circ < |b| < 1.5^\circ$ was used for background subtraction. In the GR data, H.E.S.S. finds that the gamma ray emissions are spatially correlated with molecular gas traced by CS emission lines, but a molecular gas foreground component is not subtracted from the data. The GR bounds are expected to strengthen if one were to subtract a molecular gas component.

H.E.S.S. looked more directly for dark matter annihilation in the Sagittarius dwarf spheroidal galaxy (Sgr dSph) [26]. Sgr dSph has negligible foregrounds and is thought to be dark matter dominated. A 95% C.L. model-independent bound on the gamma ray flux was obtained for $E_\gamma > 250$ GeV:

$$\Phi_\gamma(E_\gamma > 250 \text{ GeV}) < 3.6 \times 10^{-12} \text{ cm}^{-2}\,\text{s}^{-1}, \tag{2.16}$$

with a solid angle integration of $\Delta\Omega = 2 \times 10^{-5}$. Since the Sgr dSph data was taken in wobble mode and the contribution from the Sgr dSph halo is negligible in a 1.4° ring, we use $\bar{J}_{\text{eff}} = \bar{J}_{\text{on-source}}$. The value of $\bar{J}_{\text{eff}}$ strongly depends on the halo profile of Sgr dSph. For example, an NFW profile, a large core profile, and a small core profile quoted in [19] lead to

$$\bar{J}^{\text{Sgr dSph}}_{\text{NFW}} = 7.8 \times 10^2, \qquad \bar{J}^{\text{Sgr dSph}}_{\text{Large Core}} = 1.1 \times 10^2, \qquad \bar{J}^{\text{Sgr dSph}}_{\text{Small Core}} = 2.4 \times 10^4, \tag{2.17}$$

in units of $\text{GeV}^2\,\text{cm}^{-6}\,\text{kpc}$. To derive bounds, we consider NFW and large core profiles.

In Figures 2.6 and 2.7, we show the resulting constraints from the GC, GR, and Sgr dSph gamma ray observations in the m_{DM}-B plane. We also superimpose the 1σ and 2σ contours reproducing the PAMELA/ATIC data for the MED propagation model; see Figures 2.2 and 2.3. In order to plot the Sgr dSph and Milky Way bounds on the same plane, we associate the Sgr dSph small core profile with the Milky Way cored isothermal profile, and the Sgr dSph NFW profile with the Milky Way NFW and Einasto profiles. The ragged lines in the GC and GR constraints come from the binning of the H.E.S.S. data.

We note that here we have drawn the gamma ray constraints and $e^\pm$ contours assuming a common $B_{\gamma,\text{astro}}$ and $B_{e,\text{astro}}$. This is most likely not the case. For example, if dark matter clumping decreases toward the galactic center, then the gamma ray flux will decrease compared to the local positron flux. If the astrophysical boost factor for $e^\pm$ is larger than that for γ, then the gamma ray constraints become weaker by a factor of $B_{e,\text{astro}}/B_{\gamma,\text{astro}}$ compared to those shown in Figures 2.6 and 2.7.

The bounds from Sgr dSph can be modified if there are nonperturbative enhancements to the dark matter annihilation cross section. Since the velocity dispersion of dark matter in Sgr dSph is $v_{\text{Sgr}} \sim 10$ km/s [45], as opposed to $v_{\text{MW}} \sim 200$ km/s in the Milky Way, the boost factor relevant for Sgr dSph may be larger than that for electrons/positrons if part of the boost factor arises from the Sommerfeld or bound

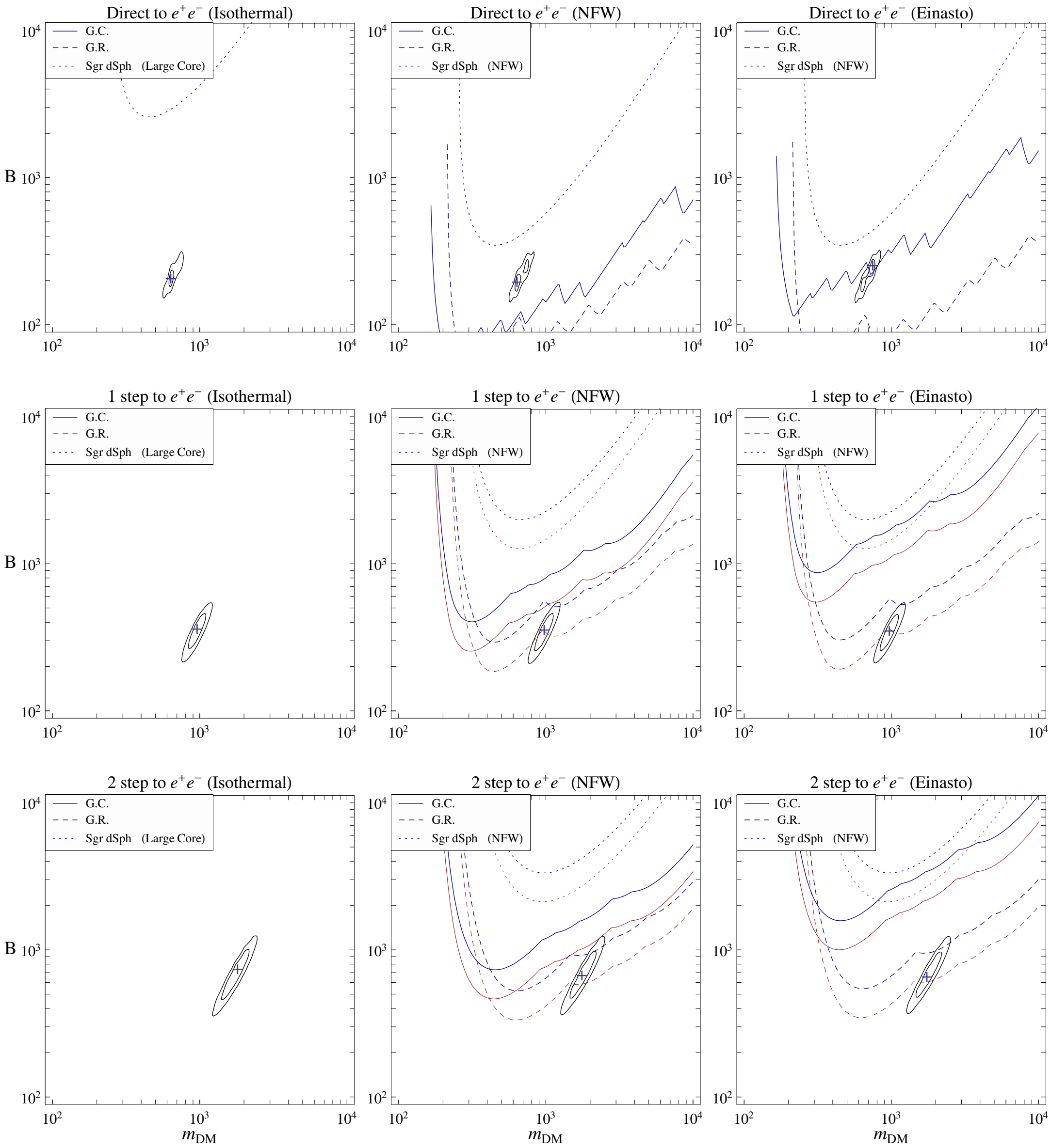

Figure 2.6: Constraints from gamma ray observations, GC (solid), GR (dashed), and Sgr dSph (dotted), in the m_{DM}-B plane for direct, 1-step, and 2-step annihilations into electron final states. All the constraints, as well as the best fit region for PAMELA/ATIC (MED propagation), are plotted assuming $B_{e,\mathrm{astro}} = B_{\gamma,\mathrm{astro}}$. For cascade annihilations, each of the GC, GR, and Sgr dSph constraints consist of two curves, with the upper (blue) and lower (red) curves corresponding to $m_1 = 100$ MeV and 1 GeV, respectively. Note that the constraint lines in the cored isothermal case are above the plot region, and that the halo profiles for Sgr dSph are given in the legends.

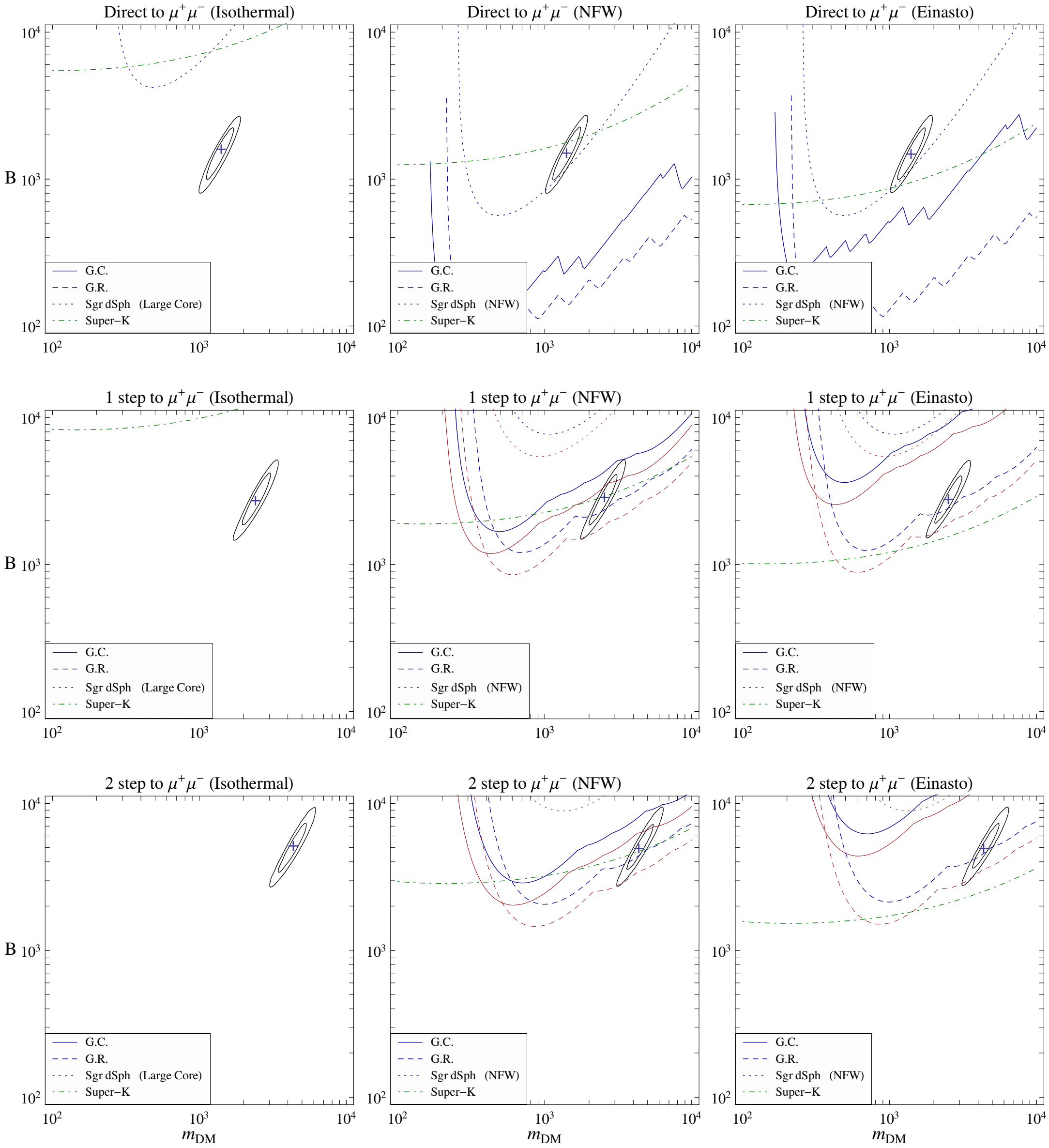

Figure 2.7: The same as Figure 2.6 but for muon final states. Also included are constraints from neutrino observations (dot-dashed) assuming $B_{\nu,\mathrm{astro}} = B_{e,\mathrm{astro}}$. For cascade annihilations, the upper (blue) and lower (red) curves now correspond to $m_1 = 600$ MeV and 1 GeV, respectively.

state enhancement. This would make the Sgr dSph constraint stronger than what is naively read from Figures 2.6 and 2.7.

Summarizing the analysis of the gamma ray constraints, we find:

- For FSR gamma rays from the galactic center region, the GR data gives somewhat stronger constraints than the GC data. For direct annihilation, this disfavors the NFW and Einasto profiles, as also seen in Refs. [18, 19]. The Sgr dSph data is not constraining unless we were to take a highly peaked halo such as the small core profile.

- The constraints from FSR photons are weaker in the cascade annihilation case than in the direct annihilation case. This is because cascade annihilations give smaller photon yield at high energies, as discussed in Appendix A.0.3. The smaller the ϕ_1 mass is, the weaker the constraints become. The constraints, however, do not become weaker by increasing the number of steps, as can be seen by comparing the best fit region for the $e^{\pm}$ data with the gamma ray constraints. This is because the reduction in the photon yield depends only on the ϕ_1 mass and not on the number of cascade steps, and the softening of the gamma ray spectra is compensated by the increase in the best fit dark matter mass and boost factor.

- The constraints are very weak for shallow halo profiles such as the cored isothermal profile for the Milky Way in Eq. (2.4). This is particularly true for the GC and GR data because the background subtraction due to on-off or wobble mode operation also subtracts (most of) the signals from dark matter annihilations. The constraints from these data, therefore, are rather weak as long as the halo profile is relatively flat within about 100 pc of the galactic center. A better bound may be obtained if we could use the unsubtracted data.

While we have focused only on FSR photons in our analysis, we wish to make a few comments about ICS, the WMAP Haze, and radio bounds. In the context of dark matter, the WMAP Haze arises because electrons from dark matter annihilation emit synchrotron radiation in the galactic magnetic fields. The total synchrotron power—and hence the size of the predicted WMAP Haze signal—depends on whether these electrons can lose energy via non-synchrotron channels. Ref. [12] found that in order to be consistent with the large boost factors necessary to explain PAMELA/ATIC, one had to assume a larger rate for ICS compared to earlier Haze analyses [15]. Given the uncertainty in galactic starlight and the dark matter halo profile, it is consistent to conservatively ignore potential bounds from ICS, but since the WMAP Haze is one of the motivations for considering dark matter annihilation, strictly speaking one should verify that the assumed electron energy loss mechanisms can yield the WMAP Haze while satisfying ICS photon bounds.

That said, we do not expect much variation in the ICS bounds between direct and cascade annihilation scenarios. ICS is calculated from a steady state configuration of charged particles, so to the extent that the PAMELA/ATIC data already normalizes the steady state electron/positron densities, the ICS yield should be similar regardless of the annihilation scenario. Therefore, the recent analysis of Ref. [12] should be representative of generic multi-step cascade annihilation scenarios. This is similar in spirit to the WMAP Haze, in that the Haze requires a source of charged particles to generate the synchrotron signal, but the precise particle energy distribution has only a secondary effect.

Finally, there has also been recent suggestions [19, 20] of a possible tension between a dark matter annihilation interpretation of the WMAP Haze and bounds from 408 MHz radio observations in the inner $4''$ of the Milky Way [46]. Such bounds assume that the steep halo profiles necessary to generate the Haze at a latitudinal distance between 5° and 30° can be extrapolated to sub-parsec distances away from the galactic center. There are a number of reasons to distrust such an extreme extrapolation of the dark matter halo, including possible effects of baryons [47] and hierarchical mergers [48] to soften cuspy behavior. At minimum, N-body simulations [49] do not have resolution to such small scales. Therefore, we find no reason to disfavor a dark matter annihilation scenario on the basis of the 408 MHz radio bound. Note that the analysis of Ref. [50] using an all-sky radio model [51] finds only relatively mild synchrotron constraints on TeV-scale dark matter after masking the inner $15^\circ \times 15^\circ$ of the galaxy.

2.5 Neutrino Constraints

When dark matter annihilates into muons, there is an irreducible source of neutrinos. Neutrinos produced in the galactic center oscillate as they travel towards earth, and if they are muon-type neutrinos when they collide with rock in the earth's crust, they can create an upward-going flux of muons. These muons could be observed by water Cerenkov detectors, and the absence of such observations puts bounds on the dark matter annihilation rate into muons. For muon cascades, there is no high energy neutrino source from dark matter that accretes in the sun and earth, because the muons from dark matter annihilation are stopped before they decay [52].

Since neutrinos have negligible energy losses as they traverse the galaxy, the muon-neutrino flux incident on earth is

$$\frac{d\Phi_{\nu_\mu}}{dE_\nu} = \sum_i P_{\nu_i \nu_\mu} \frac{B_{\nu,\mathrm{astro}}}{8\pi\eta\, m_{\mathrm{DM}}^2} \langle \sigma v \rangle \bar{J} \Delta\Omega \, \frac{dN_{\nu_i}}{dE}, \tag{2.18}$$

where i runs over the neutrino flavors, $B_{\nu,\mathrm{astro}}$ is the astrophysical boost factor for the neutrino signal which could differ from $B_{e,\mathrm{astro}}$, and $P_{\nu_i \nu_\mu}$ is the probability that ν_i has oscillated into ν_μ [53]:

$$P_{\nu_\mu \nu_\mu} = 0.39, \qquad P_{\nu_e \nu_\mu} = 0.21. \tag{2.19}$$

	3°	5°	10°	15°	20°	25°	30°
Isothermal	10	10	9.7	9.0	8.2	7.4	6.6
NFW	340	190	84	51	35	26	20
Einasto	640	370	160	91	60	43	32
Super-K (95% C.L.)	2.70	4.82	6.43	10.6	11.2	17.6	19.5

Table 2.4: $\bar{J}$ values for neutrino observations in units of $\mathrm{GeV}^2\,\mathrm{cm}^{-6}\,\mathrm{kpc}$, and Super-K 95% C.L. flux limits in units of $10^{-15}\ \mathrm{cm}^{-2}\,\mathrm{s}^{-1}$.

There is an analogous formula for $\bar{\nu}_\mu$, but in dark matter annihilations the ν_μ and $\bar{\nu}_\mu$ fluxes are equal. The primary neutrino spectra are given in Appendix A.0.2.

We now calculate the resulting upward-going muon flux following the analysis of Ref. [54]. An incident neutrino of energy E_ν creates muons of energy E_μ according to the neutrino-nucleon scattering cross sections $\sigma_{\nu N \to \mu X}$. For the propagation of created muons, we use an approximate energy loss parameterization

$$\frac{dE}{dL} = \rho_{\mathrm{mat}}(-\alpha - \beta E), \tag{2.20}$$

with "standard rock" values $\alpha = 2 \times 10^{-6}$ TeV cm^2/g and $\beta = 4 \times 10^{-6}$ cm^2/g; ρ_{mat} will cancel in the final muon flux expression. In this approximation, a muon of starting energy E_μ can travel a distance

$$L(E_\mu, E_{\mathrm{thres.}}) = \frac{1}{\rho_{\mathrm{mat}}\beta} \ln\left(\frac{\alpha + \beta E_\mu}{\alpha + \beta E_{\mathrm{thres.}}}\right) \tag{2.21}$$

before its energy drops below the muon detection threshold $E_{\mathrm{thres.}}$.

For a given $d\Phi_{\nu_\mu}/dE_\nu$, the observed muon flux is

$$\Phi_\mu = \int_{E_{\mathrm{thres.}}}^{m_{\mathrm{DM}}} dE_\mu \int_{E_\mu}^{m_{\mathrm{DM}}} dE_\nu\, n_N \left(\frac{d\Phi_{\nu_\mu}}{dE_\nu}\frac{d\sigma_{\nu_\mu N \to \mu^- X}}{dE_\mu} + \frac{d\Phi_{\bar{\nu}_\mu}}{dE_\nu}\frac{d\sigma_{\bar{\nu}_\mu N \to \mu^+ X}}{dE_\mu}\right) L(E_\mu, E_{\mathrm{thres.}}), \tag{2.22}$$

where $n_N = \rho_{\mathrm{mat}}/m_N$ is the nucleon number density in the earth's crust, and N refers to an average nucleon. We calculate the neutrino-nucleon scattering cross sections assuming an equal fraction of protons and neutrons in rock, using CTEQ5M parton distribution functions [55] to include the effect of sea quarks, and retaining the full W boson propagator in the cross section.

Super-K [56] placed 90% confidence bounds on the upward-going muon flux [29] in various cone sizes ranging from 3° to 30° around the galactic center, with $E_{\mathrm{thres.}} = 1.6$ GeV. To be more conservative, we consider 95% confidence bounds [57], as shown in Table 2.4. The relevant values of $\bar{J}$ for the three dark matter halos in Eqs. (2.4, 2.5, 2.6) are also shown in Table 2.4. To derive a bound on the annihilation rate, we insist that the predicted flux does not exceed the 95% confidence bound for any of the Super-K cone sizes. The neutrino constraints for muon cascade scenarios appear in Figure 2.7, assuming a common boost factor for the electron, gamma ray, and neutrino signals.

As observed in Ref. [52], for sufficiently small dark matter masses, the observed muon flux is nearly independent of the dark matter mass. The reason is that both the neutrino-nucleon scattering cross section and the muon range scale like energy, but the dark matter number density squared (and hence the annihilation signal) scales like $1/m_{\mathrm{DM}}^2$, so the final observed flux is simply related to the normalized second-moment of the neutrino energy spectrum. Hence the exclusion limit for the neutrino boost factor is approximately flat in m_{DM} for small enough dark matter masses. As the dark matter mass increases, the average neutrino gets harder, and the neutrino-nucleon cross section grows less steeply because of the W boson propagator. In addition, the energy-dependent term in dE/dL begins to take effect, relaxing the neutrino bounds for high dark matter masses.

Summarizing the analysis of the neutrino constraints, we find:

- Since the neutrinos are softer in cascade annihilations, the bounds on the boost factor are weaker than for direct annihilation. However, the electrons are also softer in cascade annihilations, so the PAMELA/ATIC best fit mass and boost factor rise. Put together, the neutrino tension increases marginally as the number of cascade steps increase. For direct annihilation, our results agree qualitatively with [21, 22].

- Super-K considered solid angles as large as 30°, so a large fraction ($\simeq 30\%$ to $\simeq 70\%$) of the total dark matter annihilation signal is contained within the observed region. While the Einasto profile is less peaked than NFW toward the galactic center, the Einasto bound happens to be stronger because of the large integration region. For the NFW and Einasto profiles, the dominant bounds come from the 10° cone, while for the cored isothermal profile they come from the 30° cone.

- Since the gross structure of the dark matter halo is better understood than the halo density at the galactic center, the Super-K neutrino constraints are in some sense more robust than the H.E.S.S. gamma ray constraints. As in the case of gamma rays, the bounds are rather weak for the cored isothermal profile. They are, however, significantly stronger in the more realistic NFW and Einasto profiles. For cascade decays, the neutrino constraints are comparable to or stronger than the FSR gamma ray constraints, and highlight the tension in muon cascade scenarios. As with the gamma ray bounds, however, differences between the astrophysical boost factors $B_{e,\mathrm{astro}}$ and $B_{\nu,\mathrm{astro}}$ could alleviate the tension.

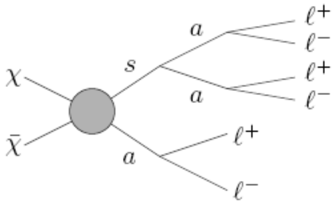

Figure 2.8: In the axion portal, fermionic dark matter annihilates dominantly into a scalar s and a pseudoscalar "axion" a. The scalar then decays as $s \to aa$, and the axion decays as $a \to \ell^+\ell^-$. In the minimal axion portal, the axion dominantly decays into muons, but in the leptonic axion portal it can dominantly decay into electrons. These models are partway between a 1-step and a 2-step cascade annihilation scenario.

2.6 The Axion Portal

One well-motivated example of a cascade annihilation scenario is the axion portal [11]. In this scenario, dark matter is a TeV-scale particle that obtains a mass from spontaneous symmetry breaking. The spontaneous breaking of $U(1)_X$ yields a pseudoscalar "axion" a and a scalar "Higgs" s, and for fermionic dark matter the dominant annihilation channel is

$$\chi\bar{\chi} \to sa \tag{2.23}$$

($\chi\chi \to sa$ if χ is a Majorana fermion). The scalar s dominantly decays as $s \to aa$, and if standard model leptons carry axial $U(1)_X$ charges, then $a \to \ell^+\ell^-$. Since a is a pseudoscalar, helicity suppression implies a will decay into the heaviest kinematically allowed lepton, which we assume is either an electron or muon. An exchange of s can also provide the necessary enhancement of the annihilation cross section through the Sommerfeld and/or bound state effect. As shown in Figure 2.8, the axion portal effectively gives a one-and-a-half step cascade annihilation in the language used here.

The simplest model for the axion portal—the minimal axion portal—is obtained if we identify $U(1)_X$ with a Peccei-Quinn symmetry rotating two Higgs doublets. In this case, a has large hadronic couplings, and there are strong constraints on the axion mass from beam dump experiments and rare meson decays. Ref. [11] found that the preferred axion mass range was 360 MeV $\lesssim m_a \lesssim$ 800 MeV, in which case a preferentially decays into muons. In the analysis here, we also consider a variant of the axion portal—the leptonic axion portal—where only leptons are charged under $U(1)_X$. This possibility was mentioned in [11], and is described in more detail in Appendix B. Dark matter in this model annihilates through the axion a_ℓ associated with the leptonic symmetry, which does not have a coupling to hadrons. The absence of hadronic couplings allows the parameter range $2m_e < m_{a_\ell} < 2m_\mu$, so a_ℓ can

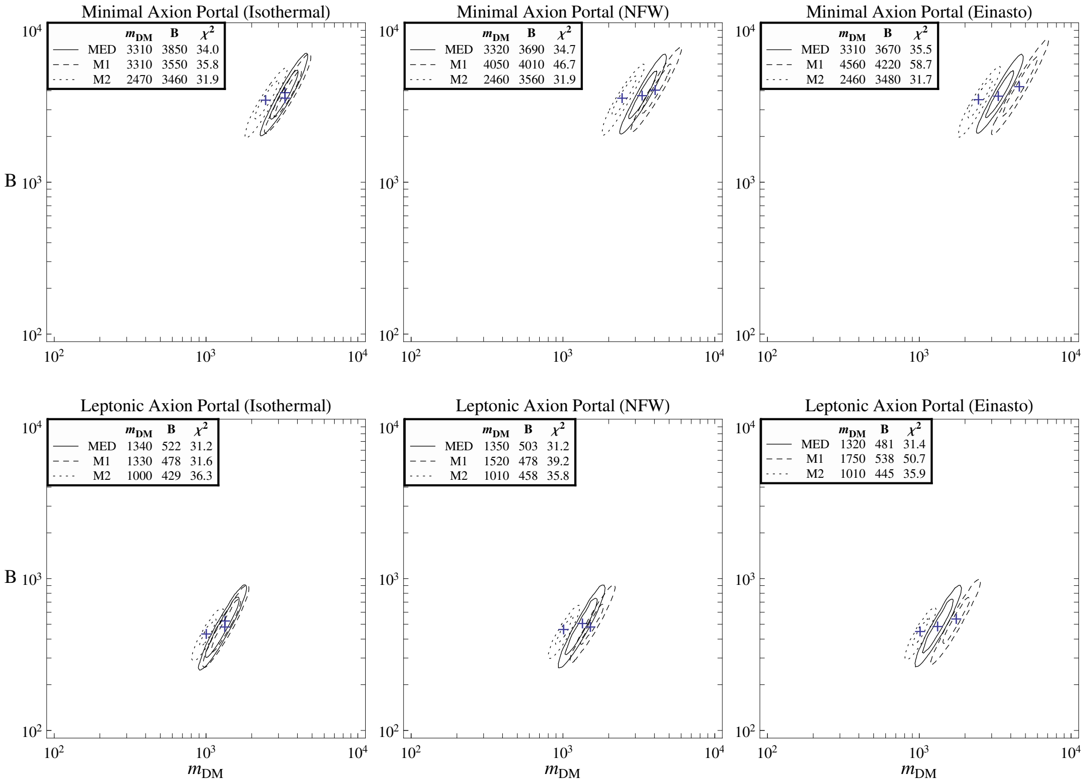

Figure 2.9: The best fit regions for the dark matter mass m_{DM} and boost factor B in the minimal axion portal (top row, $a \to \mu^+\mu^-$) and leptonic axion portal (bottom row, $a_\ell \to e^+e^-$) for different halo profiles and propagation models. The best fit values are indicated by the crosses, and the contours are for 1σ and 2σ.

preferentially decay into electrons. Note that the nonperturbative enhancement of the halo cross section is caused by the exchange of another scalar s_ℓ and not by the axion a_ℓ, so the bound of Ref. [58] does not exclude a_ℓ masses smaller than ≈ 100 MeV.

In Figure 2.9, we show the best fit values for m_{DM} and B for the PAMELA/ATIC data for the three different diffusion models and three different halo profiles. In Figure 2.10, we compare the best fit regions to FSR and neutrino constraints. Here we assume that B is common for electron, gamma ray, and neutrino signals, so that the same qualifications as Figures 2.6 and 2.7 apply. To account for the fact that smaller masses for a_ℓ are allowed, we are considering smaller values of m_{a_ℓ} in Figure 2.10 than those of m_1 in Figure 2.6. For completeness, we also show the best fit spectra to the PAMELA and ATIC data in Figure 2.11, and the p-values of the fit in Table 2.5. As expected, the best fit values and qualitative features of the plots are partway between a 1-step and a 2-step cascade scenario.

Depending on the axion mass, there are also potential gamma ray constraints from rare $a \to \gamma\gamma$ and $a \to \pi^+\pi^-\pi^0$ decay modes, and we can place bounds on the

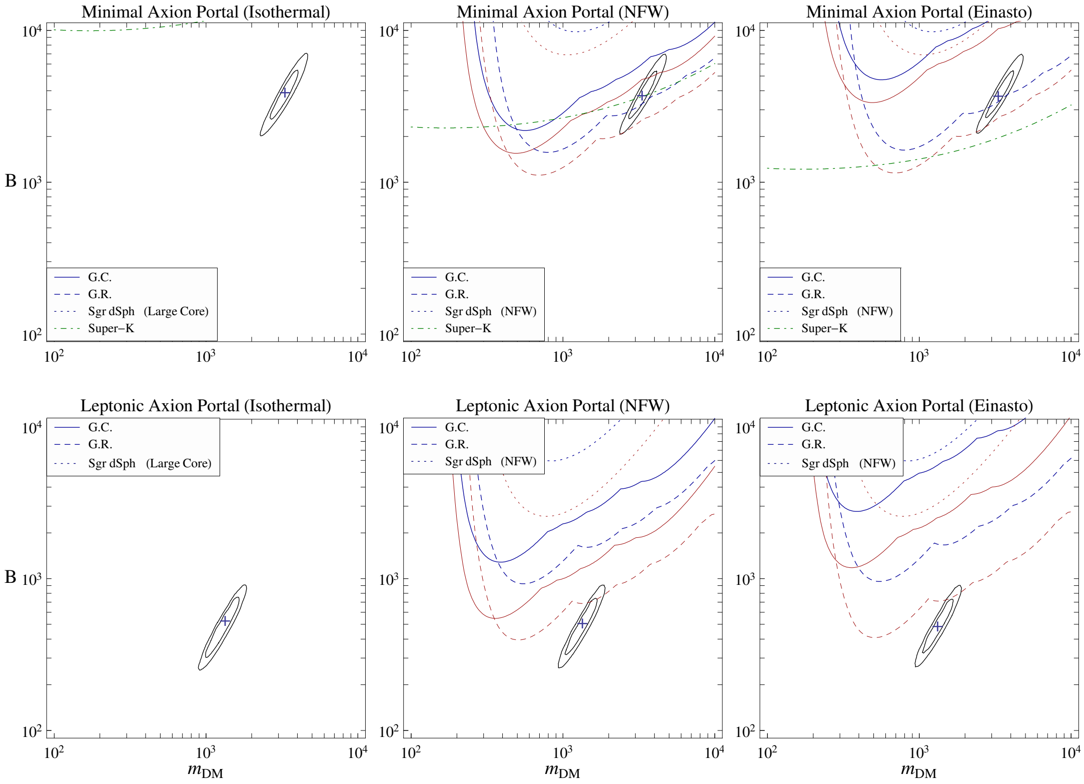

Figure 2.10: Constraints from gamma ray, GC (solid), GR (dashed), and Sgr dSph (dotted), and neutrino (dot-dashed) observations in the m_{DM}-B plane in the minimal axion portal (top row, $a \to \mu^+\mu^-$) and leptonic axion portal (bottom row, $a_\ell \to e^+e^-$). All the constraints, as well as the best fit region for PAMELA/ATIC (MED propagation), are plotted assuming that B is common. Each of the GC, GR, and Sgr dSph constraints consist of two curves. For the minimal axion portal, the upper (blue) curve is $m_a = 600$ MeV and the lower (red) curve is $m_a = 1$ GeV. For the leptonic axion portal, the upper (blue) curve is $m_{a_\ell} = 10$ MeV and the lower (red) curve is $m_{a_\ell} = 100$ MeV, which differs from the choice in Figure 2.6. Note that the constraint lines in the cored isothermal case are above the plot region, and that the halo profiles for Sgr dSph are given in the legends.

	Minimal Axion Portal	Leptonic Axion Portal
Isothermal	7.9%	9.2%
NFW	7.9%	9.2%
Einasto	8.3%	8.8%

Table 2.5: The p-values for the best propagation model for each plot in Figure 2.9.

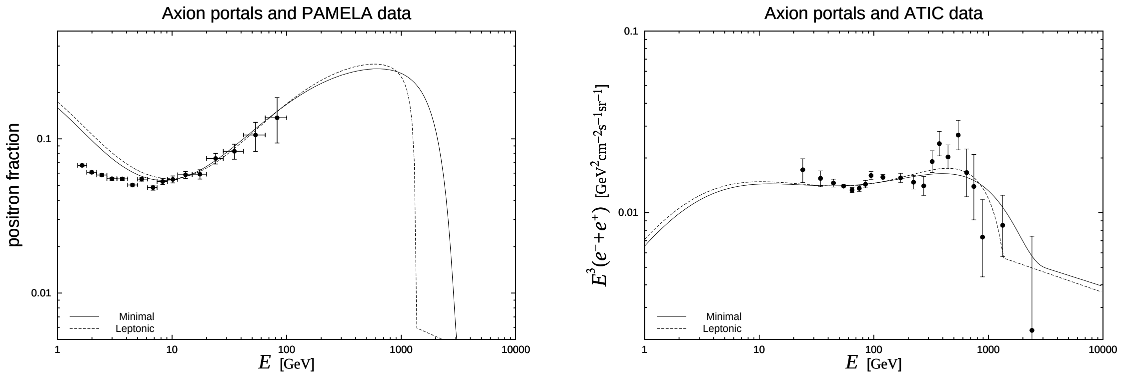

Figure 2.11: The predicted $e^{\pm}$ intensities compared to the PAMELA (left) and ATIC (right) data for the minimal axion portal (solid, $a \to \mu^+\mu^-$) and leptonic axion portal (dashed, $a_\ell \to e^+e^-$). The NFW halo profile and the MED propagation model are chosen, and the $e^{\pm}$ backgrounds are marginalized as described in Eq. (2.11). Note that we fit the PAMELA data only for $E \gtrsim 10$ GeV because solar modulation effects are important at lower energies.

branching fractions to these modes. The $a \to \gamma\gamma$ mode is potentially dangerous for the entire axion mass range, but the $a \to \pi^+\pi^-\pi^0$ mode only when $m_a > 3m_\pi$. The gamma ray spectra for these rare decays are given in Appendix A.0.5. For each halo profile and for the three H.E.S.S. data sets, we turn off FSR and find the values of the branching ratios where the H.E.S.S. bound is saturated for the best fit values of m_{DM} and B and the best propagation model (assuming B is common for $e^{\pm}$ and gamma rays).

The branching ratio bounds are shown in Tables 2.6 and 2.7. The constraints from Sgr dSph match the estimates in [11], but the GC and GR data imply a factor of 5–10 stronger bound. In the minimal axion portal, $\mathrm{Br}(a \to \gamma\gamma) \sim 10^{-5}$–$10^{-4}$, which is safe from the bounds. There is somewhat more tension for $a \to \pi^+\pi^-\pi^0$ where the estimated branching fraction was $\sim 10^{-2}$. Note, however, that the constraints from the GC and GR data are weak for any halo profile relatively flat within about 100 pc of the galactic center. In particular, there is no meaningful branching ratio constraint for the cored isothermal profile in Eq. (2.4).

Gamma ray and radio bounds on the axion portal were also considered in Ref. [20], where potential $s \to b\bar{b}$ and $s \to \tau^+\tau^-$ decay modes were included. Since these additional s decay modes depend on details of the model, we do not consider them here. For FSR gamma rays, our results and conclusions agree qualitatively with [20]. As mentioned already, we do not consider 408 MHz radio observations to place any meaningful constraint on the axion portal.

$\mathrm{Br}(a \to \gamma\gamma)$	GC	GR	Sgr dSph
NFW Best	$2.2 \cdot 10^{-3}$	$1.1 \cdot 10^{-3}$	$2.5 \cdot 10^{-2}$
Einasto Best	$4.8 \cdot 10^{-3}$	$1.2 \cdot 10^{-3}$	—

$\mathrm{Br}(a \to \pi^+\pi^-\pi^0)$	GC	GR	Sgr dSph
NFW Best	$1.3 \cdot 10^{-2}$	$7.5 \cdot 10^{-3}$	$5.2 \cdot 10^{-2}$
Einasto Best	$3.0 \cdot 10^{-2}$	$7.9 \cdot 10^{-3}$	—

Table 2.6: Bounds from gamma rays on the branching fractions of $a \to \gamma\gamma$ and $a \to \pi^+\pi^-\pi^0$ in the minimal axion portal ($a \to \mu^+\mu^-$). These are obtained neglecting all other sources of gamma rays and correspond to the best fit values for m_{DM} and B and the propagation model giving smallest χ^2. The bounds assume an equal boost factor for $e^\pm$ and gamma rays, and should be multiplied by $B_{e,\mathrm{astro}}/B_{\gamma,\mathrm{astro}}$ if the boost factors differ.

$\mathrm{Br}(a_\ell \to \gamma\gamma)$	GC	GR	Sgr dSph
NFW Best	$8.2 \cdot 10^{-3}$	$4.6 \cdot 10^{-3}$	$6.5 \cdot 10^{-2}$
Einasto Best	$1.8 \cdot 10^{-2}$	$4.9 \cdot 10^{-3}$	—

Table 2.7: The same as Table 2.6, but for the leptonic axion portal ($a_\ell \to e^+e^-$). The $a \to \pi^+\pi^-\pi^0$ mode is irrelevant in this case.

2.7 Conclusions

The possibility of indirect detection of dark matter has been considered for over 25 years [59], but the annihilation rates expected from WIMP thermal relics are typically too small to give appreciable gamma ray or neutrino fluxes from the galactic center unless a very peaked dark matter halo profile is assumed. If the PAMELA/ATIC data is indicative of dark matter annihilation, however, then the galactic annihilation rate must be boosted by $O(1000)$. This large boost factor considerably enhances the potential for galactic gamma ray and neutrino signals from the dark sector. In this context, hints from the WMAP Haze may also point towards an annihilation explanation of PAMELA/ATIC.

In this chapter, we have explored the robustness of dark matter annihilation predictions by considering cascade scenarios where dark matter annihilates into new resonances that in turn decay in one or more steps into standard model leptons. These cascade annihilation scenarios are directly motivated by the PAMELA/ATIC data, since light resonances can enhance the galactic annihilation rate through nonperturbative effects and explain the lepton-richness of the annihilation through kinematic thresholds.

We have shown that electron and muon cascades give reasonable fits to the PAMELA/ATIC data. As a rule of thumb, the best fit dark matter mass and boost factor both scale as 2^n for n-step cascade decays. We then compared these best fit values to constraints from gamma rays and neutrinos. The gamma ray bounds from FSR can be weakened by an order of magnitude through cascade decays, although increasing the length of cascades does not further weaken the bounds. Neutrino bounds for dark matter annihilating into muons are robust to changing the length of the cascade, which is particularly relevant for models with large branching fractions to muons such as the minimal axion portal.

Assuming standard NFW or Einasto halo profiles, there is tension between a dark matter annihilation interpretation of PAMELA/ATIC and the non-observation of galactic gamma rays or neutrinos. Such tension does not invalidate a dark matter annihilation hypothesis since there is considerable uncertainty in the dark matter halo distribution and velocity profile, and the constraints are uniformly weaker for shallower halo profiles. For gamma rays in particular, the galactic center and galactic ridge constraints assume an understanding of the dark matter halo profile in the inner 100 pc of the galaxy, where there is considerable uncertainty. The dark matter halo profile in the inner $4''$ of the galaxy is even more uncertain, so we do not consider radio measurements of synchrotron to be constraining. Also, for both gamma rays and neutrinos, the bounds can be weakened if the astrophysical boost factor for electrons/positrons is larger than those for gamma rays and neutrinos.

If a dark matter annihilation scenario is realized in nature with the boost factor suggested by PAMELA/ATIC, then one would expect future experiments to see a gamma ray or neutrino flux given standard halo assumptions. ANTARES [60], Ice-

Cube [61], and KM3NeT [62] will greatly increase current sensitivity to upward-going muons resulting from galactic neutrinos. Future atmospheric Cerenkov telescopes as envisioned in Ref. [63] will also improve the prospects of finding gamma rays from dark matter annihilation. While we did not include the effect of ICS in our gamma ray analysis, ICS is expected to be a dominant dark matter annihilation signal in the energy range available to the Fermi Gamma-ray Space Telescope [64]. Ultimately, one hopes that future experiments could probe the detailed energy spectra of dark matter annihilation products to distinguish between direct annihilation and the cascade scenarios considered here.

Chapter 3

Cosmic Signals from the Hidden Sector

3.1 Introduction and Summary

Weak scale supersymmetry is a very attractive candidate for physics beyond the standard model. It stabilizes the weak scale against potentially large radiative corrections, leads to successful gauge coupling unification, and predicts a plethora of new particles accessible at the LHC. This framework, however, also suffers from several generic cosmological problems, associated with overproduction of gravitinos or late decay of the field responsible for supersymmetry breaking [68, 69, 70, 71]. In many supersymmetry breaking scenarios, this requires a rather low reheating temperature after inflation, making it difficult to explain the observed baryon asymmetry of the universe.

A simple way to avoid these cosmological problems is to assume that the gravitino is very light. If the gravitino mass satisfies

$$m_{3/2} \lesssim O(10\ \mathrm{eV}), \tag{3.1}$$

then the gravitino is in thermal equilibrium with the standard model down to the weak scale. The resulting gravitino abundance is small [72] and consistent with structure formation [73]. This allows for an arbitrarily high reheating temperature, and thus baryogenesis at high energies such as thermal leptogenesis [74].

It is remarkable that this simple cosmological picture is precisely the one suggested by arguably the simplest scheme for supersymmetry breaking. Suppose that supersymmetry is dynamically broken at a scale

$$\sqrt{F} \approx O(10 - 100\ \mathrm{TeV}), \tag{3.2}$$

giving $m_{3/2} = F/\sqrt{3}M_{\mathrm{Pl}} \approx O(0.1 - 10\ \mathrm{eV})$, where $M_{\mathrm{Pl}} \simeq 2.4 \times 10^{18}$ GeV is the reduced Planck scale. Then, if the sector breaking supersymmetry is charged under the standard model gauge group, gaugino and scalar masses of order $(g^2/16\pi^2)\sqrt{F} \approx O(100\ \mathrm{GeV} - 1\ \mathrm{TeV})$ can be generated through standard model gauge loops [75, 76]. The generated squark and slepton masses are flavor universal, and thus solve the supersymmetric flavor problem. The supersymmetric Higgs mass (μ term) can also be generated through direct interactions between the Higgs fields and the supersymmetry breaking sector [77, 78] or by the vacuum expectation value of a singlet field [79].

What are the experimental signatures of this simple supersymmetry breaking scenario beyond its indirect implications on the superparticle spectrum? In this chapter we advocate that the scenario may lead to distinct astrophysical and collider signatures, due to the following features of the dynamical supersymmetry breaking sector that may appear under rather generic conditions:

Quasi-stable states: One immediate consequence of the present framework is that dark matter cannot be the lightest supersymmetric particle, which is the very light gravitino. Dark matter, however, can arise naturally as a (quasi-)stable state in the supersymmetry breaking sector [80]. Let m_{DM} be the mass of this state. The annihilation cross section is then naturally $\langle\sigma v\rangle \approx (1/8\pi)(\kappa^4/m_{\mathrm{DM}}^2)$, where κ represents typical couplings between states in the strong sector. For $m_{\mathrm{DM}} \approx O(10 - 100\ \mathrm{TeV})$, natural values for the coupling $\kappa \approx O(3 - 10)$ give $\langle\sigma v\rangle \approx (1/8\pi)(1/\mathrm{TeV}^2)$, which leads to the correct thermal abundance for dark matter, $\Omega_{\mathrm{DM}} \simeq 0.2$.

In general, a strongly interacting sector of a quantum field theory often possesses enhanced global symmetries, such as baryon number and flavor symmetries. These symmetries can lead to "stable" states if they are not broken by the strong dynamics. It is, however, quite possible that these symmetries are not respected by physics at (much) higher energies, such as at the gravitational scale. The "stable" states then become quasi-stable states, decaying through higher dimension operators on cosmological timescales.

Light axion-like states: A light state appears as a pseudo Nambu-Goldstone boson when an approximate global symmetry is spontaneously broken in the strongly interacting sector. Since our strong sector is supposed to break supersymmetry, a generic argument of Ref. [81] suggests that it may possess an accidental $U(1)$ R symmetry which is dynamically broken (even if supersymmetry is broken in a local minimum). This then leads to a light R axion, whose mass is typically of $O(1 - 100\ \mathrm{MeV})$ if the mass dominantly arises from a constant term in the superpotential canceling the vacuum energy of order F^2 [82].

More generally, it is not hard to imagine that the sector possesses enhanced approximate global symmetries. If these symmetries are spontaneously broken, light axion-like states with masses much smaller than the dynamical scale will appear. The masses of these states are then controlled by the size of explicit breaking of the corresponding symmetries.

- **Couplings to the Higgs fields:** If the supersymmetry breaking sector yields an R axion, it generically couples to, and thus mixes with, the Higgs fields. This is, in fact, the case even if the Higgs fields are not directly coupled to the supersymmetry breaking sector because the holomorphic Higgs mass-squared ($B\mu$ term) obtains loop contributions from gaugino masses, which are necessarily R-violating. For other axion-like states, mixing with the Higgs fields can arise if the Higgs fields are directly coupled to the supersymmetry breaking sector, making the corresponding symmetries Peccei-Quinn (PQ) symmetries. This is well motivated, since such couplings are often needed to generate the μ term.

It is interesting to note that all the ingredients above appear in QCD, a known strongly coupled system in nature. For the first two, one should simply think of protons, neutrons, pions, and kaons (in the appropriate limits where quark masses are small or weak interactions are superweak). Even direct Higgs couplings do exist, although the Higgs boson is much heavier than the dynamical scale of QCD, while it is much lighter than the dynamical scale considered here.

The structures described above could be manifested in various experiments. In particular, couplings between the Higgs and axion-like states provide a potential window to probe the supersymmetry breaking sector directly. Since the sector may contain dark matter as well as light states, possible signatures may appear both in astrophysical and collider physics data, and in this chapter we consider the following two classes of signatures:

- **Cosmic ray signals from decaying dark matter:** If dark matter is a quasi-stable state in the supersymmetry breaking sector, its decay may lead to various astrophysical signatures. Assuming the decay occurs through the light states, the final states can be mainly leptons, explaining the excess of the positron to electron ratio observed in the PAMELA experiment [5], along the lines of [83, 11, 84]. The required lifetime of order 10^{26} sec is obtained if the decay is caused by a dimension six operator suppressed by the unification or gravitational scale [85].

  There are characteristic features for this explanation of the PAMELA excess which are being tested in current observations. First, since the decay occurs through light states, it typically involves (long) cascade chains. Second, the mass of dark matter is rather large, $m_{\rm DM} \approx O(10\text{ TeV})$, since it arises as a quasi-stable state in the supersymmetry breaking sector. These lead to a rather broad structure in the electron plus positron spectrum in the sub-TeV region after propagation to the earth. Remarkably, we find that such a structure beautifully reproduces the spectra recently reported by the FERMI [86] and H.E.S.S. [42, 87] experiments.

- **Collider signals of light axion-like states:** The couplings between the Higgs and axion-like states imply that the axion-like states also couple to the standard model gauge fields at the loop level. Such couplings may also arise from

Symmetry	Spontaneous Breaking?	Explicit Breaking?	Consequences
R or PQ	Yes	Supergravity or $d = 5$ at M_I	Axion-like state with: $m_a \approx O(1 \text{ MeV} - 10 \text{ GeV})$ $f_a \approx O(1 - 100 \text{ TeV})$
B or F	No	$d = 6$ at M_*	Quasi-stable dark matter with: $m_{\text{DM}} \approx O(10 \text{ TeV})$ $\tau_{\text{DM}} \approx O(10^{26} \text{ sec})$

Table 3.1: The symmetry structure necessary to realize the scenario presented in this chapter. A light axion-like state emerges from spontaneous breaking of an R or PQ (Peccei-Quinn) symmetry, which then mixes with the Higgs sector of the standard model. Composite states in the strong sector are quasi-stable because of a B ("baryon number") or F ("flavor") symmetry. The R or PQ symmetry is explicitly broken by supergravity effects or by dimension five operators suppressed by $M_I \approx O(10^9 - 10^{18} \text{ GeV})$. This gives a sufficiently large mass to the axion-like state. Explicit breaking of B or F is due to dimension six operators suppressed by $M_* \approx O(10^{16} - 10^{18} \text{ GeV})$, leading to dark matter decay through the light states.

> contributions from the supersymmetry breaking sector. This leads to the possibility of producing the light states at the LHC, which subsequently decay into standard model fields through mixings with the Higgs fields [88]. The final states are most likely leptons, if recent cosmic ray data are explained as described above. This may provide a relatively clean signal to discover the light states.
>
> The couplings of the Higgs to light states also raises the possibility that the Higgs boson decays into two axion-like states. If the axion-like state decays mainly into two leptons, then this leads to a four lepton final state, whose invariant mass peaks at the Higgs boson mass. If the rate is sufficiently large, this leads to a way of seeing the axion-like state (and the Higgs boson) at hadron colliders.

The symmetry structure necessary to produce the signatures described above is summarized in Table 3.1. While this structure is strongly motivated by the low energy supersymmetry breaking scenario, all that is actually required is some strong dynamics at $\approx O(10 - 100 \text{ TeV})$ satisfying the properties given in the table. Given that QCD already has more or less all the desired ingredients, we expect that the required structure may arise naturally in wide classes of strongly interacting gauge theories, including non-supersymmetric theories. (For a non-supersymmetric theory, the symmetry leading to a light state must be a PQ symmetry. This implies that the theory must have two Higgs doublets.) The dynamical scale of $O(10 - 100 \text{ TeV})$

then suggests that this sector is related to the weak scale through a loop factor. This feature is automatic in low energy supersymmetry breaking theories.

A remarkable thing is that the first signature may have already been seen in the recent cosmic ray electron/positron data. The PAMELA experiment found an unexpected rise in the positron fraction in the energy range between 10 and 100 GeV, while the FERMI experiment saw an excess of the electron plus positron flux over standard diffuse cosmic ray backgrounds in the sub-TeV region. These results suggest a new source of primary electrons and positrons with a broad spectrum extending up to a few TeV. We find that these features are very well explained by dark matter in our framework: a quasi-stable state with mass of $O(10\text{ TeV})$, cascading into leptons through light axion-like states with lifetime of $O(10^{26}\text{ sec})$. We perform a detailed analysis for the cosmic ray data and find that a wide range for the mass is allowed for the axion-like state: it can take any value between $2m_e \simeq 1.0$ MeV and $2m_b \simeq 8.4$ GeV except for a small window between $2m_p \simeq 1.9$ GeV and $2m_\tau \simeq 3.6$ GeV.

These data, therefore, point to the setup of Table 3.1 as a new paradigm for dark matter, which can be beautifully realized in the framework of low energy supersymmetry breaking. Since the precise structure of the supersymmetry breaking sector is highly model dependent, one might worry that the signatures considered here may depend on many details of the supersymmetry breaking sector, which leads to large uncertainties. This is, however, not the case. As emphasized above, the existence of the signatures depends only on basic symmetry properties of the supersymmetry breaking sector, and their characteristics are determined only by a few parameters such as the mass of dark matter and the mass and decay constant of the axion-like state. While we will provide an illustrative model as a proof-of-concept, many details of the model are unimportant for the signatures. Of course, the flip side of this is that we cannot probe the detailed structure of the supersymmetry breaking sector solely by studying these signatures. We may, however, still explore some features by carefully studying cosmic ray spectra.

The signatures described here are complementary to the information we can obtain in other methods. In the framework of low energy supersymmetry breaking, the LHC will be able to measure some of the superparticle masses. This, however, may not determine, e.g., the scale of supersymmetry breaking, since the most general supersymmetry breaking sector provides little definite prediction on superparticle masses, as recently elucidated in Ref. [89]. The existence of the very light gravitino can give specific signals, for example, those in Ref. [90]. The signatures considered here can add even more handles. In addition to indicating the specific symmetry structure of Table 3.1, different final states for the axion-like state decay may also be discriminated, e.g., by future measurements of the diffuse γ-ray flux at FERMI. These will provide valuable information in exploring the structure of the supersymmetry breaking sector.

The organization of the chapter is as follows. In the next section, we describe our supersymmetric setup in detail. We explain that quasi-stable states with the desired lifetimes and light axion-like states with the desired masses can naturally arise. We also discuss constraints on axion-like states, and find that a wide range for the masses and decay constants are experimentally viable and can lead to leptonic decays. In Section 3.3, we present an example model that illustrates some of these general points. Dark matter is a stable "meson" state in the hidden sector that decays into R axions with a lifetime of $O(10^{26}$ sec). In Section 3.4, we perform a detailed analysis of the recent cosmic ray data, and find that the results of PAMELA, FERMI, and H.E.S.S. are very well explained. We present a general analysis in the case where dark matter decays into e^+e^-, $\mu^+\mu^-$, $\pi^+\pi^-\pi^0$, or $\tau^+\tau^-$ either directly or through 1-step or 2-step cascades. Implications for future diffuse γ-ray measurements are also discussed. In Section 3.5, we briefly discuss collider signatures associated with the existence of light states. Finally, discussion and conclusions are given in Section 3.6, where we mention related alternative scenarios.

3.2 Framework

We consider a supersymmetry breaking sector which consists of fields and interactions characterized by a scale

$$\Lambda \approx O(10 - 100 \text{ TeV}). \tag{3.3}$$

The actual spectrum of this sector could span an order of magnitude or so due to its nontrivial structure. The scale of Eq. (3.3) is supposed to arise dynamically through some strong gauge interactions in order to explain why the supersymmetry breaking scale, and thus the weak scale, is hierarchically smaller than the Planck scale [91]. We assume the sector contains fields charged under the standard model gauge group which directly feel supersymmetry breaking. Standard model gauge loops then generate gaugino and scalar masses in the supersymmetric standard model (SSM) sector through gauge mediation [75, 76].

The supersymmetry breaking sector may also directly interact with the Higgs fields in the superpotential. A possible form for these interactions is

$$W = \lambda_u H_u \mathcal{O}_u + \lambda_d H_d \mathcal{O}_d, \tag{3.4}$$

or

$$W = \lambda N H_u H_d + N \mathcal{O}_N, \tag{3.5}$$

where $H_{u,d}$ and N are two Higgs doublet and singlet chiral superfields, respectively, and $\mathcal{O}_{u,d,N}$ represent operators in the supersymmetry breaking sector. These interactions can generate the μ term, and thus lead to realistic electroweak symmetry breaking [77, 78]. A schematic picture for the current setup can be seen in Figure 3.1.

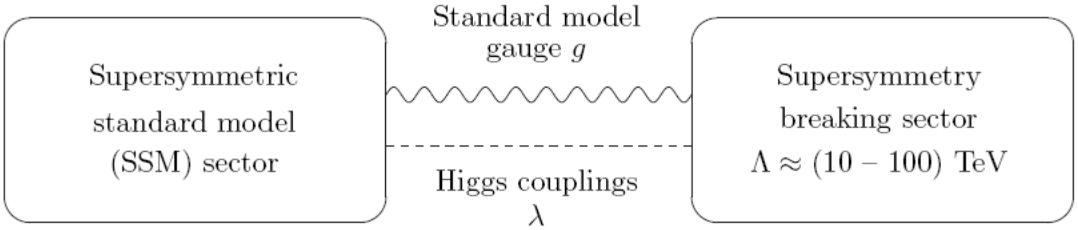

Figure 3.1: A schematic depiction of the setup.

We assume that the entire system of Figure 3.1, including both the supersymmetry breaking and SSM sectors (as well as possible direct Higgs interactions), respects some approximate global symmetry under which *both* the supersymmetry breaking and SSM sector fields are charged. This implies that the two sectors must have an interaction that can transmit charges of the global symmetry from one sector to the other. We find that an R symmetry is a natural candidate for such a symmetry, since interactions generating gaugino masses must always transmit R charges. Another simple candidate is a PQ symmetry. In the presence of direct Higgs couplings to the supersymmetry breaking sector as in Eqs. (3.4, 3.5), charges of the PQ symmetry can be transmitted. Note that R and PQ symmetries are global symmetries of the SSM sector only in the limit of vanishing μ term and gaugino (and holomorphic supersymmetry breaking) masses. To generate the μ term and gaugino masses, therefore, these symmetries must be spontaneously broken by the dynamics of the supersymmetry breaking sector.

The fundamental supersymmetry breaking scale of this class of theories is of order the dynamical scale

$$\sqrt{F} \approx \Lambda, \tag{3.6}$$

yielding a light gravitino, $m_{3/2} \approx \Lambda^2/M_{\rm Pl} \approx O(0.1 - 10\ {\rm eV})$. This solves all the cosmological problems in supersymmetric theories unless the supersymmetry breaking sector introduces its own problems,[1] which we assume not to be the case. The thermal history of the universe is normal up to a very high temperature $T \gg \Lambda$, such that the relic abundances of the quasi-stable states are determined by a standard thermal freezeout calculation.

3.2.1 Quasi-stable states

In addition to the R and PQ symmetries described above, the supersymmetry breaking and SSM sectors can have additional independent global symmetries. For example, the SSM sector has a baryon number symmetry, at least if R parity is

---

[1] Possible problems include the system being trapped in the wrong vacuum or the appearance of stable charged or colored particles.

conserved (which we need not assume here). Similarly, the supersymmetry breaking sector may possess accidental global symmetries, and since this sector is assumed to feel strong gauge interactions, natural possibilities are "baryon number" and "flavor" symmetries. If the global symmetry is not spontaneously broken by the dynamics of this sector, the lightest state charged under that symmetry is stable. This state can then be dark matter, with an abundance determined by its annihilation cross section.

Since dark matter is the lightest state charged under a global symmetry, it sits at the lowest edge of the spectrum of the corresponding charged states. It is therefore natural to expect that the dark matter mass is in the range

$$m_{\rm DM} \approx O(10\ {\rm TeV}). \tag{3.7}$$

In fact, we will see later that a mass of this size reproduces well the observed electron/positron spectrum at PAMELA, FERMI, and H.E.S.S. experiments. The annihilation cross section of dark matter is naturally of order

$$\langle \sigma v \rangle \approx \frac{1}{8\pi} \frac{\kappa^4}{m_{\rm DM}^2}, \tag{3.8}$$

where κ represents typical couplings between states in the strong sector, and we have assumed two-body annihilation. For $\kappa \approx 3$, this gives the cross section needed to reproduce the observed dark matter abundance, $\Omega_{\rm DM} \simeq 0.2$. Such a value for κ is quite natural for couplings between hadronic states in a strongly interacting sector.

The global symmetry ensuring the stability of dark matter is expected to be an accidental symmetry at low energies. This implies that the symmetry is not respected by physics at some higher energy M_*, such as the unification or Planck scale, so that the effective theory at the scale Λ contains higher dimension operators suppressed by powers of M_* that do not respect the global symmetry. This situation is precisely analogous to baryon number in the standard model embedded in grand unified theories (with M_* identified with the unification scale), or strangeness in QCD (with M_* identified with the weak scale). Dark matter can then decay with cosmologically observable timescales, depending on the dimension of the leading symmetry-violating operators.

Consistent with gauge coupling unification, we take M_* to be around the unification or Planck scale, $M_* \approx O(10^{16} - 10^{18}\ {\rm GeV})$. Then, to have observable signatures in cosmic rays, the dimension of relevant symmetry violating operators must be six, as illustrated in Ref. [85] in the case where $m_{\rm DM} \approx O({\rm TeV})$ and $M_* \approx O(10^{16}\ {\rm GeV})$. With dimension six decay operators, we find

$$\tau_{\rm DM} \approx 8\pi \frac{M_*^4}{m_{\rm DM}^5} \simeq 2 \times 10^{25}\ {\rm sec} \left(\frac{M_*}{10^{17}\ {\rm GeV}} \right)^4 \left(\frac{10\ {\rm TeV}}{m_{\rm DM}} \right)^5, \tag{3.9}$$

for two-body decays, and

$$\tau_{\rm DM} \approx 128\pi^3 \frac{M_*^4}{m_{\rm DM}^5} \simeq 3 \times 10^{27}\ {\rm sec} \left(\frac{M_*}{10^{17}\ {\rm GeV}} \right)^4 \left(\frac{10\ {\rm TeV}}{m_{\rm DM}} \right)^5, \tag{3.10}$$

for three-body decays. The required lifetime to fit the PAMELA, FERMI, and H.E.S.S. data through dark matter decay is of order 10^{26} sec, which is consistent with the value of M_* taken here.

3.2.2 Decay of quasi-stable states

There are several possible ways for the decay of dark matter to be caused by dimension six operators. One simply needs small breaking of the global symmetries protecting dark matter, and generically decays will proceed via some kinematically-allowed but symmetry-violating channel. In particular, dark matter can decay into light axion-like states and/or the gravitino. As long as the dimension six operators are suppressed by the unification or Planck scale, they can even explicitly violate the R or PQ symmetry that gives rise to the axion-like state, since such explicit breaking gives very small masses compared to the contributions considered in Section 3.2.3.

Suppose that interactions in the supersymmetry breaking sector are asymptotically free, so that the dimensions of the operators are determined by the canonical dimensions of the elementary fields. Suppose also, for illustrative purposes, that the supersymmetry breaking sector contains a gauge group $SU(N_c)$ $(N_c \geq 3)$ with N_f flavor of "quark" fields $Q^i + \bar{Q}_{\bar{\imath}}$ $(i, \bar{\imath} = 1, \cdots, N_f)$, where Q^i and $\bar{Q}_{\bar{\imath}}$ are chiral superfields in the fundamental and anti-fundamental representations of $SU(N_c)$, respectively. We also assume that the quark fields have generic masses of order Λ (or somewhat smaller) due to some (R-violating) dynamics in the supersymmetry breaking sector.

The $SU(N_c)$ gauge group is supposed to confine at a scale $\approx \Lambda$. This then leads to composite "meson" fields $M^i_{\bar{\jmath}} \sim Q^i \bar{Q}_{\bar{\jmath}}$, and also "baryon" and "antibaryon" fields $B \sim Q^{N_c}$ and $\bar{B} \sim \bar{Q}^{N_c}$ for $N_f \geq N_c$. Because of the nonzero quark masses, these fields have masses of order Λ (or somewhat smaller). Moreover, in the limit that nonrenormalizable operators vanish, the states $M^i_{\bar{\jmath}}$ $(i \neq \bar{\jmath})$, B and $\bar{B}$ can easily be stable (except for B and $\bar{B}$ for $N_c = 3$). These states are therefore good candidates for dark matter.

The lifetimes of the quasi-stable states described above are controlled by the form of higher dimension operators. Let us begin with the case where dark matter is identified with baryons (and antibaryons). The decay of dark matter can then occur through baryon number violating operators in the superpotential. These operators are dimension six if $N_c = 5$:[2]

$$W \sim \frac{1}{M_*^2} QQQQQ + \frac{1}{M_*^2} \bar{Q}\bar{Q}\bar{Q}\bar{Q}\bar{Q}, \tag{3.11}$$

in which case the lifetime of dark matter can be of order 10^{26} sec as needed to reproduce the electron/positron data.[3]

---

[2] In the following equations, any one of the operators is sufficient to cause dark matter decay. In particular, physics at M_* need not respect a $Q \leftrightarrow \bar{Q}$ symmetry.

[3] A long-lived hidden sector baryon with the $SU(5)$ gauge group was considered in Ref. [92] in the

An alternative possibility is that dark matter decays through holomorphic terms in the Kähler potential K, which can also be viewed as superpotential terms suppressed by an extra power of $M_{\rm Pl}$ after performing a Kähler transformation. The required lifetime is obtained for $N_c = 3$:

$$K \sim \frac{1}{M_*} QQQ + \frac{1}{M_*} \bar{Q}\bar{Q}\bar{Q} + \text{h.c.} \quad \Longrightarrow \quad W \sim \frac{\Lambda^2}{M_* M_{\rm Pl}} QQQ + \frac{\Lambda^2}{M_* M_{\rm Pl}} \bar{Q}\bar{Q}\bar{Q}, \tag{3.12}$$

where we have used the fact that the superpotential has a constant term of order $\Lambda^2 M_{\rm Pl}$ to cancel the cosmological constant, and assumed that the renormalizable superpotential term $W \sim QQQ$ is absent, perhaps because of an R symmetry. Note that in both of the cases above, the number of "colors" N_c needs to be chosen appropriately to have dimension six dark matter decay.

We now consider the case where the meson states $M^i_{\bar{\jmath}}$ $(i \neq \bar{\jmath})$ are dark matter. These states exist even for $N_f < N_c$, and the longevity of their lifetime could be ensured by a vector-like $U(1)^{N_f}$ symmetry that may exist in the Lagrangian at the renormalizable level. The decay of these states can be caused by dimension six operators in the Kähler potential:

$$K \sim \frac{1}{M_*^2} Q^\dagger_i Q^j Q^\dagger_k Q^l + \frac{1}{M_*^2} \bar{Q}^{\dagger \bar{\imath}} \bar{Q}_{\bar{\jmath}} \bar{Q}^{\dagger \bar{k}} \bar{Q}_{\bar{l}} + \frac{1}{M_*^2} Q^\dagger_i Q^j \bar{Q}^{\dagger \bar{k}} \bar{Q}_{\bar{l}}. \tag{3.13}$$

Possible lower dimension operators in the superpotential $W \sim (1/M_*) Q^i \bar{Q}_{\bar{\jmath}} Q^k \bar{Q}_{\bar{l}}$ can easily be absent, for example by imposing an R symmetry. An attractive feature of this possibility is that the lifetime does not depend on the number of colors N_c, and that the number of flavors N_f need not be equal to or larger than N_c. This setup, therefore, can naturally be accommodated in a wide variety of gauge theories. In Section 3.3, we present an explicit model realizing this possibility, where the quasi-stable mesons decay via Eq. (3.13) into R axions.

Although we have not considered them in the discussion above, in general the supersymmetry breaking sector also contains states not charged under $SU(N_c)$. Dark matter decay may then occur through these states. For example, mesons may decay through operators of the form $K \sim Q^\dagger_i Q^j \Phi^\dagger \Phi / M_*^2 + \bar{Q}^{\dagger \bar{\imath}} \bar{Q}_{\bar{\jmath}} \Phi^\dagger \Phi / M_*^2$, where Φ represents a generic field in the supersymmetry breaking sector. The existence of singlet fields can also change the requirement on N_c for the baryon dark matter case. As long as the lowest symmetry breaking operators are dimension six, however, the existence of these operators do not affect the basic argument.[4] Below, we assume

---

context that the quarks Q^i are also charged under the standard model gauge group. This model, however, does not preserve the success of perturbative gauge coupling unification, since the extra matter content charged under the standard model gauge group is too large, see e.g. [93]. Here we consider that the quarks Q^i are not charged under the standard model gauge group.

[4] With singlets, some of the accidental symmetries are not as "automatic" as the case without singlets. For example, the low energy $U(1)^{N_f}$ flavor symmetry does not exist if the quarks couple to two or more singlets with arbitrary Yukawa couplings.

for simplicity that operators containing only quarks dominate the decay. Whether this is the case or not is determined by physics at the scale M_*. This also implies that direct interactions between the supersymmetry breaking and SSM sectors, such as $K \sim Q_i^\dagger Q^j \Phi_{\rm SSM}^\dagger \Phi_{\rm SSM}/M_*^2 + \bar{Q}^{\dagger\bar{\imath}}\bar{Q}_{\bar{\jmath}}\Phi_{\rm SSM}^\dagger \Phi_{\rm SSM}/M_*^2$, are relatively suppressed. Here, $\Phi_{\rm SSM}$ represents SSM fields. We will comment on the case where these interactions are relevant in Section 3.6.

3.2.3 Light axion-like states

Spontaneous breaking of an approximate R or PQ symmetry in the supersymmetry breaking sector leads to a pseudo Nambu-Goldstone boson. The phenomenology associated with this particle is determined largely by its mass m_a and decay constant f_a. Suppose that relevant interactions in the supersymmetry breaking sector obey naive dimensional analysis for a generic strongly coupled theory [94]. In this case, we find that the decay constant is naturally somewhat ($\approx 4\pi$) smaller than the dynamical scale $\Lambda \approx O(10 - 100~{\rm TeV})$:

$$f_a \approx O(1 - 10~{\rm TeV}). \tag{3.14}$$

According to naive dimensional analysis, the generic size for expectation values of the lowest and highest components of a chiral superfield Φ are given by $\langle\Phi\rangle \approx \Lambda/4\pi$ and $\langle F_\Phi\rangle \approx \Lambda^2/4\pi$, respectively, and a generic coupling constant has the size $\kappa \approx 4\pi$. (Here we have ignored a possible N_c or N_f factor associated with the multiplicity of fields, but this does not affect the basic discussion.) This implies that a generic supersymmetric mass and supersymmetry breaking mass-squared splitting in the supersymmetry breaking sector are of order $M_{\rm mess} \approx \kappa\langle\Phi\rangle \approx \Lambda$ and $F_{\rm mess} \approx \kappa\langle F_\Phi\rangle \approx \Lambda^2$, respectively, so that the gaugino and scalar masses generated in the SSM sector are of order $(g^2/16\pi^2)F_{\rm mess}/M_{\rm mess} \approx (g^2/16\pi^2)\Lambda$, which is consistent with Eq. (3.3). On the other hand, the decay constant of an axion-like state scales as $f_a \approx \langle\Phi\rangle \approx \Lambda/4\pi$, giving Eq. (3.14). Note that the suppression of f_a over Λ here is precisely analogous to the fact that in QCD the pion decay constant, $f_\pi \approx O(100~{\rm MeV})$, is an order of magnitude smaller than the characteristic QCD scale, i.e. the rho meson mass $m_\rho \approx O(1~{\rm GeV})$.[5]

The mass of a light axion-like state is determined by the size of explicit symmetry breaking. Let us first consider the state associated with an R symmetry—an R axion. An interesting feature of an R axion is that it has an irreducible contribution to its mass from supergravity, whose size can be determined by the strength of fundamental

---

[5] In general, it may not be true that all the couplings in the supersymmetry breaking sector are strong. In this case, the decay constant need not obey Eq. (3.14); for example, it can be easily of $O(100~{\rm TeV})$. In particular, if the messenger fields (fields in the supersymmetry breaking sector charged under the standard model gauge group) feel R-breaking effects though perturbative interactions, then f_a for an R axion needs to be of $O(10~{\rm TeV})$ or larger to generate sufficiently large gaugino masses.

supersymmetry breaking F. This is because to cancel the cosmological constant, the superpotential must have a constant piece $\langle W\rangle \approx FM_{\rm Pl} \approx O(\Lambda^2 M_{\rm Pl})$, which is necessarily R-violating. Since $\langle W\rangle \gg \Lambda^3$, the constant piece must come from a sector other than the supersymmetry breaking sector, implying that it appears as explicit breaking from the perspective of the supersymmetry breaking sector. This provides the following contribution to the R axion mass [82]

$$m_a^2 \approx 4\pi \frac{F\langle\Phi\rangle^3}{M_{\rm Pl} f_a^2} \approx \frac{\Lambda^3}{4\pi M_{\rm Pl}} \approx O(10\text{ MeV})^2 \left(\frac{\Lambda}{100\text{ TeV}}\right)^3, \tag{3.15}$$

where $\langle\Phi\rangle$ is a generic vacuum expectation value in the supersymmetry breaking sector, and we have used $\langle\Phi\rangle \approx \Lambda/4\pi$, $f_a \approx \Lambda/4\pi$, and $F \approx \Lambda^2/4\pi$. The uncertainty of the estimate, however, is very large, so that we can easily imagine m_a in the range $O(1 - 100\text{ MeV})$. Unless the supersymmetry breaking sector contains another explicit breaking of the R symmetry, the R axion mass is given by Eq. (3.15).

We now consider the case of a PQ symmetry, or of additional explicit breaking of an R symmetry. If the symmetry is violated by dimension five operators in the supersymmetry breaking sector, then we expect

$$m_a^2 \approx \frac{f_a^3}{M_I} \approx O(100\text{ MeV})^2 \left(\frac{\Lambda}{100\text{ TeV}}\right)^3 \left(\frac{10^{14}\text{ GeV}}{M_I}\right), \tag{3.16}$$

where we have introduced the scale M_I for physics causing the explicit breaking. We imagine M_I to take a value between an intermediate scale and the gravitational scale, $M_I \approx O(10^9 - 10^{18}\text{ GeV})$, giving $m_a \approx O(1\text{ MeV} - 10\text{ GeV})$. While smaller masses are possible, they are in conflict with astrophysical measurements as we will see later. The origin of the intermediate scale might be associated, for example, with the Peccei-Quinn scale for the QCD axion, the scale of the constant term in the superpotential, or the $B-L$ breaking scale generating right-handed neutrino masses.[6] Alternatively, the explicit breaking may be due to a tiny dimensionless coupling in the supersymmetry breaking sector. Note that a possible contribution from the QCD anomaly, $m_a \approx m_\pi(f_\pi/f_a) \approx O(1\text{ keV})(100\text{ TeV}/\Lambda)$, is small.

3.2.4 Couplings of axion-like states

The couplings of the axion-like states to the SSM sector are completely determined by the symmetry structure. We are considering the case in which the Higgs bilinear $h_u h_d$ is charged under the symmetry that leads to the light state, where $h_{u,d}$ are the lowest components of $H_{u,d}$. This is almost always true for an R symmetry (unless direct couplings of the Higgs to the supersymmetry breaking sector force vanishing

---

[6] If we use $f_a \approx \Lambda$ instead of $\Lambda/4\pi$, we obtain $m_a^2 \approx O(100\text{ MeV})^2(\Lambda/100\text{ TeV})^3(10^{17}\text{ GeV}/M_I)$. This gives $m_a \approx O(1\text{ MeV} - 1\text{ GeV})$ for $M_I \approx M_*$.

charges for $H_{u,d}$), and is by definition true for a PQ symmetry. In both cases, we can take a field basis in which the axion-like state a is mixed into the $h_{u,d}$ fields:

$$h_u = v_u\, e^{i\frac{\cos^2\!\beta}{\sqrt{2}f_a}a}, \tag{3.17}$$

$$h_d = v_d\, e^{i\frac{\sin^2\!\beta}{\sqrt{2}f_a}a}, \tag{3.18}$$

where $v_{u,d} = \langle h_{u,d}\rangle$ and $\tan\beta = \langle h_u\rangle/\langle h_d\rangle$. The distribution of a inside $h_{u,d}$ is determined by the condition that a is orthogonal to the mode absorbed by the Z boson, and we have arbitrary chosen the $O(1)$ normalization for f_a. The expressions of Eqs. (3.17, 3.18) completely determine the leading-order couplings of a to the standard model quarks and leptons. For example, the couplings to the up quark, down quark, and electron relevant for a decay are given by

$$\mathcal{L} = -i\frac{m_u\cos^2\!\beta}{\sqrt{2}f_a}\, a\,\bar{\Psi}_u\gamma_5\Psi_u - i\frac{m_d\sin^2\!\beta}{\sqrt{2}f_a}\, a\,\bar{\Psi}_d\gamma_5\Psi_d - i\frac{m_e\sin^2\!\beta}{\sqrt{2}f_a}\, a\,\bar{\Psi}_e\gamma_5\Psi_e, \tag{3.19}$$

where $m_{u,d,e}$ are the up quark, down quark, and electron masses. The couplings to heavier generation fermions are similar.

The couplings of a to the Higgs boson h can be obtained by replacing $v_{u,d}$ as

$$v_u \to v_u + \frac{\cos\alpha}{\sqrt{2}}h, \qquad v_d \to v_d - \frac{\sin\alpha}{\sqrt{2}}h, \tag{3.20}$$

in Eqs. (3.17, 3.18) and plugging the resulting expressions into the Higgs kinetic terms $\mathcal{L} = |\partial_\mu h_u|^2 + |\partial_\mu h_d|^2$. Here, α is the Higgs mixing angle. This leads to

$$\mathcal{L} = \frac{c_1 v}{\sqrt{2}f_a^2}\, h(\partial_\mu a)^2 + \frac{c_2}{4f_a^2}\, h^2(\partial_\mu a)^2, \tag{3.21}$$

where $v = \sqrt{v_u^2 + v_d^2}$, $c_1 = \sin\beta\cos\beta(\cos^3\!\beta\cos\alpha - \sin^3\!\beta\sin\alpha)$, and $c_2 = \cos^4\!\beta\cos^2\!\alpha + \sin^4\!\beta\sin^2\!\alpha$. In the decoupling limit, $\alpha \approx \beta - \pi/2$, this equation reduces to

$$\mathcal{L} = \frac{v\sin^2\!2\beta}{4\sqrt{2}f_a^2}\, h(\partial_\mu a)^2 + \frac{\sin^2\!2\beta}{16f_a^2}\, h^2(\partial_\mu a)^2. \tag{3.22}$$

The first term is responsible for Higgs decay into two axion-like states.

There are also couplings between a and the standard model gauge bosons. Their precise values depend on the matter content of the entire theory. At a given energy scale E, effective direct interactions between a and the gauge bosons are given by

$$\mathcal{L} = \sum_A \frac{g_A^2 c_A}{32\pi^2\sqrt{2}f_a}\, aF^A_{\mu\nu}\tilde{F}^{A\mu\nu}, \tag{3.23}$$

where A runs over the gauge groups accessible at the scale E, and g_A and c_A are the gauge coupling and a coefficient of order unity. The coefficient c_A encodes the contributions from physics above E, and is determined by the symmetry properties of the fields integrated out to obtain the effective theory. At the electroweak scale or below, we generically expect $c_A \neq 0$ for color, $A = SU(3)_C$, and electromagnetism, $A = U(1)_{\rm EM}$. The interaction with gluons ($A = SU(3)_C$) is responsible for direct production of a at hadron colliders.

3.2.5 Constraints on axion-like states

The axion-like states for the R and PQ symmetries considered here couple to the standard model fields as the DFSZ axion [95], except for possible differences in the numerical coefficients c_A. Their masses, however, are much heavier because of explicit symmetry breaking, so that the experimental constraints on them are quite different from those on the DFSZ axion. Here we summarize the constraints on m_a and f_a for the region relevant to our discussions. For previous related analyses, see Refs. [11, 96].

The constraints on an axion-like state a depend strongly on its decay mode. The decay width of a into two fermions is given by

$$\Gamma(a \to f\bar{f}) = \frac{n_f c_f^2}{16\pi} \frac{m_f^2 m_a}{f_a^2} \left(1 - \frac{4m_f^2}{m_a^2}\right)^{1/2}, \tag{3.24}$$

where $n_f = 1$ and 3 for leptons and quarks, respectively, and $c_f = \sin^2\!\beta$ for $f = e, \mu, \tau, d, s, b$ while $c_f = \cos^2\!\beta$ for $f = u, c, t$. The decay width into two photons is

$$\Gamma(a \to \gamma\gamma) = \frac{c_\gamma^2 e^4}{32\pi(16\pi^2)^2} \frac{m_a^3}{f_a^2}, \tag{3.25}$$

where c_γ represents the c_A coefficient for $U(1)_{\rm EM}$ at energies below m_e, and e is the electromagnetic gauge coupling.

For $m_a < 2m_e$, a decays mainly into two photons with the decay width of Eq. (3.25), giving

$$c\tau_{a\to\gamma\gamma} \simeq 5.9 \times 10^9 \text{ m } \frac{1}{c_\gamma^2} \left(\frac{1 \text{ MeV}}{m_a}\right)^3 \left(\frac{f_a}{10 \text{ TeV}}\right)^2. \tag{3.26}$$

A possible decay of an R axion into two gravitinos has the width $\Gamma(a \to \tilde{G}\tilde{G}) \approx (1/16\pi) m_{3/2}^2 m_a / f_a^2$, and is thus negligible unless $m_a \lesssim (4\pi/\alpha) m_{3/2}$. For $2m_e \lesssim m_a \lesssim 2m_\mu$, a decays dominantly into e^+e^- with the decay width of Eq. (3.24), giving

$$c\tau_{a\to e^+e^-} \simeq 3.8 \times 10^2 \text{ m } \frac{1}{\sin^4\!\beta} \left(\frac{10 \text{ MeV}}{m_a}\right) \left(\frac{f_a}{10 \text{ TeV}}\right)^2 \left(1 - \frac{4m_e^2}{m_a^2}\right)^{-1/2}. \tag{3.27}$$

For $2m_\mu < a \lesssim 800$ MeV, the $a \to \mu^+\mu^-$ mode dominates with

$$c\tau_{a\to\mu^+\mu^-} \simeq 3.0 \times 10^{-4} \text{ m } \frac{1}{\sin^4\!\beta} \left(\frac{300 \text{ MeV}}{m_a}\right) \left(\frac{f_a}{10 \text{ TeV}}\right)^2 \left(1 - \frac{4m_\mu^2}{m_a^2}\right)^{-1/2}. \tag{3.28}$$

In this region, the $a \to \pi\pi$ mode is suppressed by CP invariance, and $a \to \pi\pi\pi$ has the width of order $(1/128\pi^3)(m_\pi^4 m_a/f_\pi^2 f_a^2)$, which is much smaller than $\Gamma(a \to \mu^+\mu^-)$. For $m_a \gtrsim 800$ MeV, the $a \to \rho^*\pi \to \pi\pi\pi$ and $a \to \eta\pi\pi$ modes become important, but the final states still contain a significant fraction of leptons from charged pion decay, unless $m_a \gtrsim 2$ GeV where nucleon modes start dominating. For $2m_\tau < m_a < 2m_b$, a will decay dominantly into taus with

$$c\tau_{a\to\tau^+\tau^-} \simeq 6.3 \times 10^{-8}\ \mathrm{m}\ \frac{1}{\sin^4\beta}\left(\frac{5\ \mathrm{GeV}}{m_a}\right)\left(\frac{f_a}{10\ \mathrm{TeV}}\right)^2\left(1-\frac{4m_\tau^2}{m_a^2}\right)^{-1/2}. \qquad (3.29)$$

The branching ratio into $c\bar{c}$ is $\approx 3m_c^2/m_\tau^2 \tan^4\beta$, which is highly suppressed for $\tan\beta \gtrsim 2$. For $m_a > 2m_b$ the $a \to b\bar{b}$ mode dominates.

Rare decays of mesons provide strong constraints on axion-like states. In particular, the $K^+ \to \pi^+ a$ process gives significant constraints on the region of interest. The theoretical estimate for the branching ratio is $\mathrm{Br}(K^+ \to \pi^+ a) \gtrsim 1.1 \times 10^{-8}(10\ \mathrm{TeV}/f_a)^2$ [97]. For $m_a < 2m_\mu$, the a decay length is large enough that a appears as an invisible particle in K decay experiments. The experimental bound on the branching ratio is then $\mathrm{Br}(K^+ \to \pi^+ a) \lesssim 7.3 \times 10^{-11}$ [98]. While the theoretical estimate has large uncertainties, this gives the rough bound

$$f_a \gtrsim 100\ \mathrm{TeV} \quad \text{for} \quad m_a < 2m_\mu. \qquad (3.30)$$

For $2m_\mu < m_a < m_K - m_\pi$, a decays quickly into $\mu^+\mu^-$, so that the relevant experimental data is $\mathrm{Br}(K^+ \to \pi^+\mu^+\mu^-) \simeq 1 \times 10^{-7}$ [99], which is consistent with standard model expectations. Considering that the dimuon invariant mass would be peaked at m_a for a decay, $\mathrm{Br}(K^+ \to \pi^+ a)$ should be somewhat smaller than this number, giving a conservative bound of

$$f_a \gtrsim \text{a few TeV} \quad \text{for} \quad 2m_\mu < m_a < m_K - m_\pi. \qquad (3.31)$$

Radiative decay of Υ also provides constraints, but the bounds are typically $f_a \gtrsim O(\mathrm{TeV})$ (for $a \to \mu^+\mu^-$ [100]) or weaker (for $a \to \tau^+\tau^-$ [101]), and do not significantly constrain the parameter region considered here.

There are constraints from beam-dump experiments. For example, the experiment of Ref. [102] excludes $f_a \lesssim (10 - 100)$ TeV for $2m_e < m_a < 2m_\mu$. None of these experiments, however, gives as strong bounds as the ones from kaon decay given above, except for possible small islands in parameter space. Constraints from reactor experiments are also similar. They are not as strong as those from kaon decay, except that the experiment of Ref. [103] excludes a region of f_a somewhat above 100 TeV for $2m_e < m_a \lesssim 10$ MeV.

Astrophysics provides strong constraints on very light axion-like states [67]. A combination of the bounds from the dynamics of the sun, white dwarfs, and horizontal branch stars excludes $m_a \lesssim 300$ keV for the relevant region of $f_a \approx O(1 - 100\ \mathrm{TeV})$.

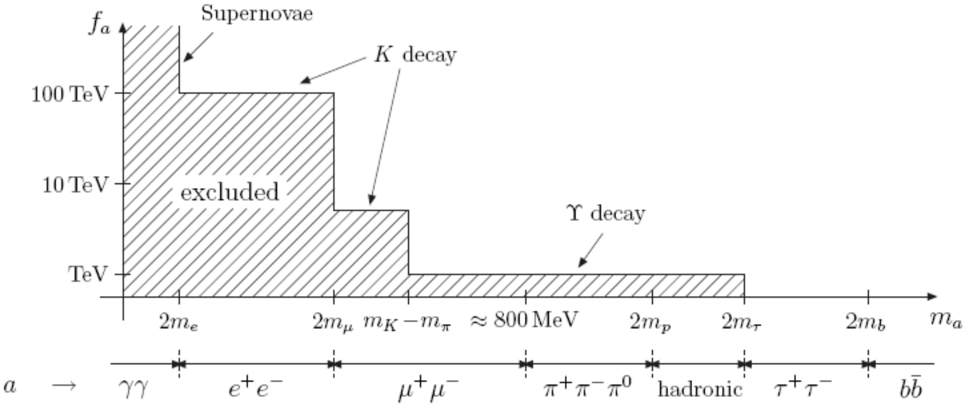

Figure 3.2: A schematic picture for the constraints on the m_a-f_a plane, with the shaded region corresponding to the excluded region. Note that the actual limits on f_a have $O(1)$ uncertainties, as explained in the text. The dominant a decay mode for a given value of m_a is also depicted.

Supernova 1987A could also provide potentially strong constraints. If an a produced in a supernovae were to freely escape, then its mass would be excluded up to $\approx O(1\text{ GeV})$ with the a production rates corresponding to the f_a values considered here.[7] This is, however, not the case. For $f_a \approx O(1 - 100\text{ TeV})$, the produced a is either trapped inside the supernovae or decays quickly, so that it does not carry away significant energy. In particular, for $m_a > 2m_\mu$, a immediately decays into muons, which are then thermalized quickly. Supernova 1987A, therefore, does not strongly constrain the parameter space considered here, except that the region $m_a < 2m_e$ is excluded by nonobservation of γ rays from a decays [104].

A schematic diagram summarizing the bounds on m_a and f_a is depicted in Figure 3.2, together with the dominant a decay modes. For $f_a \approx O(1 - 100\text{ TeV})$, the most natural region avoiding all the constraints are $m_a > 2m_\mu$, although $m_a < 2m_e$ is still allowed for $f_a \approx O(100\text{ TeV})$. For the range $m_a \approx O(1\text{ MeV} - 10\text{ GeV})$ considered in Eqs. (3.15, 3.16), a natural a decay mode will be either $\mu^+\mu^-$, $\tau^+\tau^-$, $\pi^+\pi^-\pi^0$, or hadronic (or e^+e^- for $f_a \approx O(100\text{ TeV})$). As we will see in Section 3.4, a decay into $\mu^+\mu^-$, $\tau^+\tau^-$, or $\pi^+\pi^-\pi^0$ (or e^+e^-) can provide a spectacular explanation for the recently observed electron/positron signals in cosmic rays.

3.3 Illustration

In this section, we present an example model which illustrates some of the general points discussed above. The model has quasi-stable meson fields carrying nontrivial flavor, which we identify with dark matter. We find that this dark matter, in fact,

---

[7] We thank Savas Dimopoulos for discussion on this point.

decays dominantly into R axions (an R axion and a gravitino if the lightest meson field is a fermion) through dimension six operators. The lifetime of dark matter can therefore be naturally of $O(10^{26}\ \text{sec})$. The resulting R axion decays into standard model particles as shown in Section 3.2.4, leading to astrophysical signatures discussed below in Section 3.4. We also show that under reasonable assumptions, the correct thermal abundance for dark matter can be obtained through a standard freezeout calculation.

3.3.1 Setup in supersymmetric QCD

Ideally, one would want to construct a complete model where supersymmetry (and R symmetry) is dynamically broken and successfully mediated to the SSM sector. It is, however, notoriously difficult to realize such explicit constructions [105]. Here, we will use the example of supersymmetric QCD to show that quasi-stable dark matter candidates can arise from strong dynamics with spontaneous R-symmetry breaking. In Section 3.3.4, we will show that this strong sector can be consistently coupled to supersymmetry breaking dynamics and to messenger fields, and we will comment on the parametric difference between the dark matter mass and the scale of supersymmetry breaking.

Our starting point here is supersymmetric QCD where the number of flavors N_f is less than the number of colors N_c. In the ultraviolet, the matter content consists of quark fields Q^i and $\bar{Q}_{\bar{\imath}}$ $(i, \bar{\imath} = 1, \cdots, N_f)$. We couple these fields to a singlet field S in the superpotential:

$$W = \lambda_i^{\bar{\jmath}} S Q^i \bar{Q}_{\bar{\jmath}}. \tag{3.32}$$

With only one singlet, these couplings can always be diagonalized by rotations of the quark fields, $\lambda_i^{\bar{\jmath}} = \lambda_i \delta_i^{\bar{\jmath}}$, and we can then easily see that this theory has an accidental $U(1)^{N_f}$ flavor symmetry, where each $U(1)$ factor corresponds to a vector-like rotation of the quark fields of a given flavor. The theory also possesses a non-anomalous $U(1)_R$ symmetry with

$$R(Q) = R(\bar{Q}) = 1 - \frac{N_c}{N_f}, \qquad R(S) = \frac{2N_c}{N_f}. \tag{3.33}$$

To realize our setup, the R symmetry must be spontaneously broken. Here we treat its effect through the background expectation value of the S field, which is sufficient to understand the properties of dark matter. We will eventually allow S to be a dynamical field in Section 3.3.4.

Below the dynamical scale of QCD, which we take to be close to the scale charactering the entire supersymmetry breaking sector,[8] the appropriate degrees of freedom to describe the dynamics are composite meson fields $M^i_{\bar{\jmath}} \sim Q^i \bar{Q}_{\bar{\jmath}}$ interacting via a

---

[8] We discuss a potential difference between the dynamical scale Λ appearing here and the scale that breaks supersymmetry in Section 3.3.4.

non-perturbative superpotential [106]. Together with the couplings of Eq. (3.32), this leads to the effective superpotential

$$W = \tilde{\lambda}_i \Lambda S M_i + \lambda_M (N_c - N_f)\Lambda^3 \left(\frac{\Lambda^{N_f}}{\det M} \right)^{\frac{1}{N_c - N_f}} , \tag{3.34}$$

where Λ is the dynamical scale, and $M_i \equiv M^i_{\bar{\imath}}$ $(i = \bar{\imath})$ are the diagonal mesons. The coefficient λ_M is an unknown factor coming from canonically normalizing the meson fields, and a similar factor for the first term is absorbed into the definition of $\tilde{\lambda}_i$. Using naive dimensional analysis, the size of these coefficients are $\lambda_M \approx O((4\pi)^{-(2N_c - N_f)/(N_c - N_f)})$ and $\tilde{\lambda}_i/\lambda_i \approx O(1/4\pi)$. Note that there are no low energy baryon fields when $N_f < N_c$.

Setting $\langle S \rangle \neq 0$ but $\langle F_S \rangle = 0$, the superpotential of Eq. (3.34) has a stable supersymmetry-preserving, R-violating minimum. Defining $m_i = \tilde{\lambda}_i \langle S \rangle$ and $\det m = \prod_i m_i$, the minimum of the potential is at

$$\langle M_i \rangle = \frac{\alpha_M \Lambda^2}{m_i}, \qquad \langle M^i_{\bar{\jmath}} \rangle = 0 \quad (i \neq \bar{\jmath}), \tag{3.35}$$

where for convenience we have defined $\alpha_M = \lambda_M (\det m / \lambda_M^{N_f} \Lambda^{N_f})^{1/N_c}$. According to naive dimensional analysis, $m_i \approx O(\lambda \langle S \rangle / 4\pi)$ and $\alpha_M \approx O((\lambda \langle S \rangle / \Lambda)^{N_f/N_c} / 16\pi^2)$, where λ represents the size of the original couplings in Eq. (3.32). Since $\langle M^i_{\bar{\jmath}} \rangle = 0$ for $i \neq \bar{\jmath}$, the $U(1)^{N_f}$ flavor symmetry is unbroken, making the $M^i_{\bar{\jmath}}$ mesons with $i \neq \bar{\jmath}$ (for now, absolutely) stable. Therefore, the lightest components of these fields, either scalars or fermions, are dark matter candidates.

The diagonal mesons M_i are unstable. Since the R symmetry is assumed to be spontaneously broken, the theory has a light R axion with the decay constant f_a of order Λ. The couplings of the mesons to the R axion are determined by symmetries, and by doing appropriate field redefinitions, these couplings can be read off from the meson kinetic terms.[9] For the scalar components, the kinetic term is $\mathcal{L} = |\partial_\mu M_{ii} + i c_M (\langle M_i \rangle + M_{ii})(\partial_\mu a)/f_a|^2$, where $M_{ii} \equiv M_i - \langle M_i \rangle$ and c_M is an $O(1)$ coefficient that depends on R charges of the fields. Assuming real $\langle M_i \rangle$, this gives a coupling of $\mathrm{Re}(M_{ii})$ to two R axions, and coupling between $\mathrm{Re}(M_{ii})$, $\mathrm{Im}(M_{ii})$, and an R axion. Therefore, $\mathrm{Re}(M_{ii})$ decays promptly into two R axions, while $\mathrm{Im}(M_{ii})$ decays (somewhat less) promptly into three R axions via an off-shell $\mathrm{Re}(M_{ii})$. After supersymmetry breaking, the fermionic component of M_{ii} has a coupling to the corresponding scalar component and a gravitino, suppressed by powers of Λ. This allows the M_{ii} fermion to decay promptly into a gravitino and an R axion.

---

[9] Once the S field becomes dynamical, S will mix with the meson fields. This can introduce extra contributions to the couplings, especially if there is no hierarchy between the scales involved. It, however, does not affect the basic conclusion here.

3.3.2 Thermal relic abundance

Expanding around the minimum of the potential from Eq. (3.35), the mass terms for the mesons are

$$W = \frac{\Lambda}{2\alpha_M}\sum_{ij}\left(M_{ij}M_{ji}\frac{m_i m_j}{\Lambda^2} + \frac{1}{N_c - N_f}M_{ii}M_{jj}\frac{m_i m_j}{\Lambda^2}\right), \qquad (3.36)$$

where we have used the notation $M_{ij} \equiv (M^i_{\bar{j}} - \langle M^i_{\bar{j}}\rangle)|_{\bar{j}=j}$. The stable mesons ($M_{ij}$ with $i \neq j$) do not have mixing terms because of the unbroken $U(1)^{N_f}$ symmetry, while the unstable mesons (M_{ii}) have a mixing term that is suppressed by $1/(N_c - N_f)$. For simplicity of discussion, we will focus on the large N_c limit where there is a simple relationship between the stable and unstable meson masses:

$$\mathrm{mass}(M_{ij}) \simeq \sqrt{\mathrm{mass}(M_{ii})\,\mathrm{mass}(M_{jj})}. \qquad (3.37)$$

Up to $1/(N_c - N_f)$ corrections, the leading interaction term for the mesons is

$$W = -\frac{1}{3\alpha_M^2}\sum_{ijk} M_{ij}M_{jk}M_{ki}\frac{m_i m_j m_k}{\Lambda^3} + \frac{1}{4\alpha_M^3}\sum_{ijkl} M_{ij}M_{jk}M_{kl}M_{li}\frac{m_i m_j m_k m_l}{\Lambda^5}. \qquad (3.38)$$

The superpotential coupling in Eq. (3.38) allows for various annihilation diagrams for stable M_{ij} mesons. By the mass relation in Eq. (3.37), either the ii-type or jj-type mesons will be lighter than the ij-type mesons. Assuming $m_i < m_j$, the annihilation cross section for $M_{ij}M_{ji} \to M_{ii}M_{ii}$ scales like

$$\langle\sigma v\rangle \sim \frac{1}{8\pi}\frac{\kappa^4}{m_{\mathrm{DM}}^2}, \qquad m_{\mathrm{DM}} \sim \frac{1}{\alpha_M}\frac{m_i m_j}{\Lambda}, \qquad \kappa \sim \frac{1}{\alpha_M^2}\frac{m_i^2 m_j}{\Lambda^3}. \qquad (3.39)$$

Using naive dimensional analysis, these quantities can be estimated as

$$m_{\mathrm{DM}} \sim \Lambda\left(\frac{\lambda\langle S\rangle}{\Lambda}\right)^{2-\frac{N_f}{N_c}}, \qquad \kappa \sim 4\pi\left(\frac{\lambda\langle S\rangle}{\Lambda}\right)^{3-\frac{2N_f}{N_c}}, \qquad (3.40)$$

so that the required annihilation rate can naturally be obtained. For example, it is easy to obtain $m_{\mathrm{DM}} \approx O(10\ \mathrm{TeV})$ and κ a factor of a few, which leads to $\langle\sigma v\rangle \sim (1/8\pi)(1/\mathrm{TeV}^2)$, and thus $\Omega_{\mathrm{DM}} \simeq 0.2$. Note that here we have not included possible multiplicity factors in naive dimensional analysis, which will somewhat decrease the value of κ. We therefore do not prefer very large N_c in practice. Note also that, strictly speaking, our analysis is not theoretically very well under control for $\lambda\langle S\rangle \gtrsim \Lambda$, although we expect that the basic dynamics is still as presented for $\lambda\langle S\rangle \sim \Lambda$.

There is subtlety when annihilation occurs into states of comparable mass. If $m_i \simeq m_j$, then the ij-, ii-, jj-type are nearly degenerate for relatively large N_c. In this case, one must use the methods of Ref. [107] to properly calculate the thermally averaged annihilation rate. One can, however, still obtain the right thermal relic abundance with somewhat stronger couplings. If N_f is large, then there is a potential for multiple dark matter components having comparable abundances. The freezeout calculation can then be affected by various co-annihilation channels.

3.3.3 Dark matter decays

The $U(1)^{N_f}$ flavor symmetry which ensures the stability of dark matter arises as an accidental symmetry of the renormalizable interactions of Eq. (3.32). As such, it is plausible that this symmetry is not respected by physics at the unification or gravitational scale. Suppose that the leading operators encoding the high energy physics are the Kähler potential terms

$$K = \frac{1}{M_*^2} \eta^{ik}_{jl} Q_i^\dagger Q^j Q_k^\dagger Q^l, \tag{3.41}$$

with arbitrary flavor structures for η^{ik}_{jl} in the basis where the interactions of Eq. (3.32) are diagonal: $\lambda_i^{\bar\jmath} = \lambda_i \delta_i^{\bar\jmath}$. Below the scale Λ, these operators can then be matched into[10]

$$K = \frac{\Lambda^2}{M_*^2} c^{i\bar l}_{\bar\jmath k} M_i^{\dagger\bar\jmath} M^k_{\bar l}, \tag{3.42}$$

where $c^{i\bar l}_{\bar\jmath k}$ are coefficients. Using naive dimensional analysis, we find $c^{i\bar l}_{\bar\jmath k} \approx O(1/16\pi^2)$ for $\eta^{ik}_{jl} \approx O(1)$ and $\lambda_i \langle S \rangle \approx O(\Lambda)$. In general, one expects $c^{i\bar l}_{\bar\jmath k}$ to have $O(1)$ CP-violating phases.

The existence of the terms in Eq. (3.42) induces mixings between the diagonal and off-diagonal meson states, leading to the decay of dark matter. The decay width has a large suppression from the Λ^2/M_*^2 factor in Eq. (3.42), so that the lifetime of dark matter is very long. One possible decay chain arises through $M_{ii} \to aa$, where a is the R axion. Through the mixing, this leads to

$$M_{ij} \to aa, \tag{3.43}$$

where we have assumed that dark matter M_{ij} is a scalar.[11] For fermionic dark matter, one of the a's must be replaced by a gravitino $\tilde{G}$. Another possibility is that dark matter decays through the meson self interactions of Eq. (3.38). Again, through the mixing, this can lead to

$$M_{ij} \to M_{ii} M_{ii}, \tag{3.44}$$

---

[10] The same argument as below applies to the operator $K = (1/M_*^2)\bar{Q}^{\dagger\bar\imath}\bar{Q}_{\bar\jmath}\bar{Q}^{\dagger\bar k}\bar{Q}_{\bar l}$ or $(1/M_*^2)Q_i^\dagger Q^j \bar{Q}^{\dagger\bar k}\bar{Q}_{\bar l}$.

[11] Because of the CP-violating phases in $c^{i\bar l}_{\bar\jmath k}$, even $\mathrm{Im}(M_{ij})$ dominantly decays into two R axions, not three.

if it is kinematically allowed, $\mathrm{mass}(M_{ij}) > 2\,\mathrm{mass}(M_{ii})$. Here, M_{ii} in the final state can be either a scalar or fermion, which subsequently decays into aa or $a\tilde{G}$, respectively.

For the scalar dark matter decay in Eq. (3.43), the lifetime of dark matter can be estimated as

$$\tau_{\mathrm{DM}} \approx 8\pi \frac{f_a^4}{m_{\mathrm{DM}}^3 \langle M \rangle^2} \left(\frac{M_*^2}{c\Lambda^2} \right)^2 \simeq 3 \times 10^{27}\ \mathrm{sec} \left(\frac{1/16\pi^2}{c} \right)^2 \left(\frac{M_*}{10^{17}\ \mathrm{GeV}} \right)^4 \left(\frac{10\ \mathrm{TeV}}{\Lambda} \right)^5, \tag{3.45}$$

where $\langle M \rangle$ is a typical meson expectation value, c represents a generic size for the coefficients $c^{i\bar{l}}_{\bar{j}k}$ in Eq. (3.42), and we have used $m_{\mathrm{DM}} \approx 4\pi f_a \approx \Lambda$ in the last equation. For M_* of order the unification scale, the lifetime is in the range required to produce observable cosmic ray signatures. While there are different parametric dependences for τ_{DM} if one uses the decay mode in Eq. (3.44) or if one considers fermionic dark matter decay, they all give the same estimate as Eq. (3.45) after using naive dimensional analysis.

3.3.4 Towards a more complete theory

In the above discussion, we assumed that $\langle S \rangle$ could be treated as a spurion for the spontaneous breaking of the R symmetry. In a complete theory, S would be a propagating degree of freedom that is part of a larger supersymmetry breaking sector. Naively coupling S to the mesons as in Eq. (3.34), the F_S-term potential would change the meson vacuum structure. In particular, even if S could be stabilized through terms in the Kähler potential, there is generically a mesonic runaway direction [108].

Therefore, it is important to have a proof-of-concept that a propagating S field can not only obtain an R-violating vacuum expectation value but also couple to the mesons without introducing runaway behavior. In addition, one would like to see that appropriate messenger fields can be added to the theory to communicate supersymmetry breaking to the SSM. While a complete theory would incorporate these two effects in a completely dynamical setting with all scales set by dimensional transmutation, here we consider O'Raifeartaigh-type models in order to treat these effects modularly (with a dynamical model mentioned only briefly towards the end). We leave further model building to future work, although we emphasize that the precise details of supersymmetry breaking are largely irrelevant for the dark matter discussion.

We will also not be concerned by the specific mass hierarchies needed to realize a realistic theory. Typically, the scale of supersymmetry breaking should be closer to $O(100\ \mathrm{TeV})$ to obtain a realistic superparticle spectrum, while the mass scale for dark matter suggested by the cosmic ray data is closer to $O(10\ \mathrm{TeV})$. In a single scale theory with naive dimensional analysis, both mass scales are expected to coincide. However, in a complete dynamical theory of supersymmetry breaking, there may be additional structures that generate such a "little" hierarchy.[12] For example, this can be realized if the $SU(N_c)$ theory in Section 3.3.1 is in a strongly interacting conformal window at high energies. If nontrivial dynamics kicks in at the scale $O(100\text{ TeV})$ to break supersymmetry, the same dynamics can make the $SU(N_c)$ theory deviate from the fixed point, presumably due to decoupling of some degrees of freedom, leading to the dark matter setup considered here. The physics of R breaking will be associated with the higher scale dynamics.

To see how S can be made dynamical, consider adding the following interactions to Eq. (3.34):

$$W = \lambda_X X \left(S\bar{S} - \mu_S^2\right) + m_S S Y + \bar{m}_S \bar{S}\bar{Y}. \tag{3.46}$$

These interactions could be the low energy description of a more complete supersymmetry breaking sector, and so we consider that μ_S, m_S, and $\bar{m}_S$ are roughly of order Λ. Regardless of the R charge of the S field (i.e. regardless of N_f and N_c), there is a unique consistent R charge assignment for the new fields, with

$$R(X) = 2, \qquad R(\bar{S}) = -\frac{2N_c}{N_f}, \qquad R(Y) = 2 - \frac{2N_c}{N_f}, \qquad R(\bar{Y}) = 2 + \frac{2N_c}{N_f}. \tag{3.47}$$

With the inclusion of the m_S term, the F_S equation of motion simply sets the value of Y and does not change the potential for the mesons, so that the global minimum of the meson potential is still given by Eq. (3.35). The λ_X coupling forces S and $\bar{S}$ to obtain vacuum expectation values, and the m_S and $\bar{m}_S$ terms constrain S and $\bar{S}$ from running away to infinity. As long as $\lambda_X^2\mu_S^2 > m_S\bar{m}_S$, this theory has a supersymmetry- and R-breaking global minimum away from the origin, with S vacuum expectation value given by

$$\langle S\rangle = \sqrt{\frac{\bar{m}_S}{m_S}\left(\mu_S^2 - \frac{m_S\bar{m}_S}{\lambda_X^2}\right)}. \tag{3.48}$$

At tree level, the only fields that obtain F-term vacuum expectation values are X, Y, and $\bar{Y}$, so the off-diagonal mesons only feel supersymmetry breaking at loop level. The vacuum expectation value of X is unspecified at tree level, but one expects loop effects to stabilize X, though not necessarily at $\langle X\rangle = 0$. Since supersymmetry and R are both broken regardless of the value of $\langle X\rangle$, this is an example of a model where supersymmetry and R are spontaneously broken at tree level.[13]

In principle, one could calculate the full spectrum of the theory at one loop, allowing one to test whether the stable dark matter is the fermionic or bosonic component of the off-diagonal mesons. In practice, this is a nontrivial exercise given the large

---

[12] This little hierarchy may not be necessary in general if the axion-like state decays into $\pi^+\pi^-\pi^0$ or $\tau^+\tau^-$ (see Figure 3.4) and the number of messenger fields is relatively large.

[13] In the language of Ref. [109], Eq. (3.46) is the "$g = 0$" superpotential which preserves a $U(1)_R$ symmetry and spontaneously breaks a global $U(1)_A$ symmetry. The inclusion of Eq. (3.32) identifies a linear combination of $U(1)_R$ and $U(1)_A$ as the true $U(1)'_R$ symmetry, such that the R symmetry is broken.

amount of mixing between the various new degrees of freedom. If the dynamical sector is truly strongly coupled, then loop counting would not apply, and the mesons could feel $O(1)$ supersymmetry breaking effects depending on the details of the Kähler potential. Therefore, one would not expect a one-loop calculation to get the correct sign for the fermion/boson splitting.

We have seen that Eq. (3.32) can be consistently coupled to the supersymmetry- and R-breaking sector in Eq. (3.46). It is then straightforward to couple messenger fields to the supersymmetry breaking, using an analogous structure to Eq. (3.46). Regardless of how X is stabilized, the Y field obtains vacuum expectation values in both the lowest and highest components, so Y can communicate supersymmetry breaking to the SSM sector through complete $SU(5)_{\rm SM}$ messenger multiplets. Consider adding the superpotential

$$W = \lambda_Y Y F \bar{F} + m_F F \bar{F}' + \bar{m}_F F' \bar{F}, \tag{3.49}$$

where F and F' are $\mathbf{5}$s of $SU(5)_{\rm SM}$, and $\bar{F}$ and $\bar{F}'$ are $\bar{\mathbf{5}}$s, and there is a consistent R charge assignment for the messengers. Taking $m_F \bar{m}_F > \lambda_Y m_S \langle S \rangle$, we can ensure that the messengers do not develop vacuum expectation values. With this kind of messenger sector, the gaugino masses are proportional to F_Y^3 instead of F_Y [110]. They are, therefore, suppressed compared with the scalar masses for $\lambda_Y F_Y \ll m_F \bar{m}_F$, which may not be fully desired. Moreover, one also needs to take $m_F \simeq \bar{m}_F$ to avoid an unwanted large Fayet-Iliopoulos term for $U(1)$ hypercharge. As a proof-of-concept, however, we see that it is possible to couple the dark matter, supersymmetry breaking, and messenger sectors together in a consistent way.

If one desires, the above model can be extended in such a way that all the dimensionful scales μ_S, m_S, $\bar{m}_S$, m_F, and $\bar{m}_F$ are generated dynamically. These scales can be replaced by a single chiral superfield T, which obtains a vacuum expectation value through $W = Z(T^2 - \mu_T^2)$. The new scale μ_T can then be generated from dimensional transmutation, e.g., by replacing μ_T^2 with a quark condensate as in Ref. [110]. For appropriate parameter choices, this extension leaves the O'Raifeartaigh dynamics largely intact. To connect the μ_T scale to the Λ scale of supersymmetric QCD, we can introduce extra quarks Q' and $\bar{Q}'$ of $SU(N_c)$ that make the theory conformal at high energies. The quarks obtain masses from $W = TQ'\bar{Q}'$, triggering the exit from a strongly-coupled fixed point. This provides an existence-proof model where all the scales are generated dynamically associated with single dimensional transmutation. The μ term can also be generated by introducing singlet "messengers" and coupling them, together with the doublet messengers, to the SSM Higgs fields as in Ref. [77].

Note that there is a Z_2 parity in Eq. (3.49) under which all the messenger fields are odd. Such a parity is often present in realistic constructions for the supersymmetry breaking sector. In order to avoid the problem of unwanted colored/charged relics, however, the messenger fields (either elementary or composite) must decay. If the decay occurs through dimension five operators suppressed by M_* and if the decay products contain an SSM state, then this may explain the discrepancy of the measured

^{7}Li abundance from the prediction of standard big-bang nucleosynthesis, along the lines of Ref. [111]. In fact, the lowest dimension for the operators causing messenger decay can easily be five if, for example, the messenger fields are two-body bound states, such as meson states, of some strong dynamics.

3.4 Astrophysical Signatures

We have seen that dark matter in the present scenario naturally has the following features, which are not shared by the standard weakly interacting massive particle (WIMP) scenario:

- The mass of dark matter is of $O(10\text{ TeV})$, which is significantly larger than the weak scale. The correct thermal abundance, however, is still obtained because of the relatively large annihilation cross section.
- Dark matter can decay through dimension six operators, and thus with lifetime of $O(10^{26}\text{ sec})$. This can lead to observable cosmic ray signatures.
- Dark matter can decay into light axion-like states (and to the gravitino if dark matter is a fermion), which in turn decays into standard model particles. The final states can naturally be only e^+e^-, $\mu^+\mu^-$, $\pi^+\pi^-\pi^0$, or $\tau^+\tau^-$.

In fact, these features are precisely what are needed to explain recent electron/positron cosmic ray data from PAMELA, FERMI, and H.E.S.S. In this section, we demonstrate that recent astrophysical data are indeed beautifully explained in the present setup, and provide a fit to the parameters $m_{\rm DM}$ and $\tau_{\rm DM}$ using the observed electron/positron fluxes. We also discuss the diffuse γ-ray flux that could be seen in the near future by experiments such as FERMI.

Let us begin with a summary of the observational situation. The PAMELA experiment has recently reported an unexpected rise in the positron fraction $\Phi_{e^+}/(\Phi_{e^+}+\Phi_{e^-})$ in the energy range between about 10 and 100 GeV [5]. On the other hand, they did not see any deviation from the expected background in the antiproton data [23]. The FERMI experiment is the first to be able to measure the combined electron and positron flux with good precision and control of uncertainties over the entire range from 20 GeV to 1 TeV. Their recent data also show an excess over standard diffuse cosmic ray backgrounds [86], with a broad structure extending up to the highest energies.[14] At higher energies, data from the H.E.S.S. experiment indicates a spectral break in the combined electron and positron flux at around 1 TeV, with the spectral index increasing from ≈ 3.0 to ≈ 4.1 [87].

---

[14] The ATIC [112] and PPB-BETS [113] experiments have also reported an excess in the combined flux at around 600 GeV, although with a peaked spectral shape that does not seem to fully agree with the FERMI data. With their significant statistical and experimental uncertainties, we do not include these results in our analysis.

While there remain experimental uncertainties as well as difficulty in calculating astrophysical background fluxes, taken together these results suggest a new source of primary electrons and positrons with a broad spectrum extending up to a few TeV. An exciting possibility is that these are signals of annihilation or decay of galactic dark matter [9, 85], although astrophysical interpretations, e.g. in terms of nearby pulsars [114], are also possible. When interpreted in terms of dark matter, the data has certain implications:

- The structure around TeV in the combined e^+ and e^- flux is very broad, implying that electrons/positrons do not arise directly from dark matter annihilation or decay; rather, they arise through some cascading processes.
- The spectral cutoff around TeV, together with the broad structure, implies that the mass of dark matter is larger than TeV. In particular, if cosmic rays arise from decay of dark matter, then the mass scale is more like $O(10\text{ TeV})$, especially if the cascade is sufficiently long.
- The absence of signal in the antiproton data implies that dark matter annihilates or decays mainly into leptons, although precisely how much nucleonic final states should be suppressed is not completely clear because of uncertainties in proton/antiproton propagation models.

These interpretations are consistent with detailed analyses performed after the recent FERMI data release [115, 116].

The fact that a naive WIMP dark matter candidate, such as the neutralino lightest supersymmetric particle (LSP), does not satisfy the above criteria is quite suggestive. In the present scenario, dark matter mass is naturally of $O(10\text{ TeV})$, which decays with lifetime of $O(10^{26}\text{ sec})$ producing the observed $e^{\pm}$ signatures. The decay occurs through a light axion-like state (axion portal), so that the final states can selectively be leptons.[15] This also ensures that the final state leptons arise through cascades, making the spectrum consistent with the latest FERMI and H.E.S.S. data. It is also worth mentioning that decaying dark matter is much less constrained than annihilating dark matter [116], which has some tension with γ-ray and neutrino observations [119, 2].

3.4.1 PAMELA, FERMI, and H.E.S.S. electron/positron data

There are various possible decay chains in the present scenario, depending on which state is dark matter and the decay properties of the axion-like state a. Here we consider two representative classes: 1-step cascade ($\phi \to aa$; $a \to \ell^+\ell^-$) and 2-step cascade ($\phi \to \phi'\phi'$; $\phi' \to aa$; $a \to \ell^+\ell^-$), where ϕ and ϕ' represent dark matter and another state in the supersymmetry breaking sector, respectively, and $\ell = e, \mu, \tau$. We

---

[15] An R axion as the portal was mentioned in Ref. [11] and developed further in Ref. [117] in the context of annihilating dark matter. For a related suggestion in dark matter annihilation, see [118].

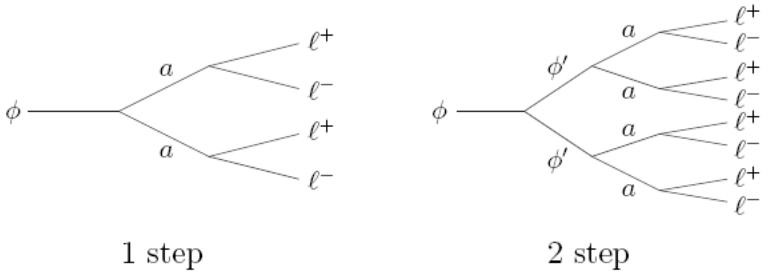

Figure 3.3: Cascade decays of dark matter ϕ through an axion-like state a. Here, ϕ' is an unstable state in the supersymmetry breaking sector, and $\ell^\pm$ $(\ell = e, \mu, \tau)$ are standard model leptons.

also consider $a \to \pi^+\pi^-\pi^0$. An example with a 1-step cascade was already seen in Section 3.3: dark matter is (the scalar component of) the lightest "meson," which decays into two axion-like states. The axion-like state then decays into standard model fields, as seen in Section 3.2.5. A 2-step cascade can easily arise if (the scalar component of) the lightest "baryon" is dark matter. After including dimension six baryon number violating operators, this state can decay into two meson states, each of which then decays into two axion-like states. Alternatively, dark matter may be a meson state which dominantly decays into other meson states, as seen in Section 3.3.3.

The processes just described are depicted in Figure 3.3. In the case where dark matter is a fermionic component, one side of some step of the cascade should be replaced by the gravitino, but this does not change the predicted signals, except that the dark matter lifetime must be rescaled by appropriate factors. Below, we present the fit of the predicted $e^\pm$ fluxes to the PAMELA and FERMI data. We find that good agreements between the predictions and data are obtained for all the cases considered, except that the 1-step $e^\pm$ case may have some tension with the H.E.S.S. data. While we only present the results for $a \to e^+e^-$, $\mu^+\mu^-$ and $\tau^+\tau^-$ here, we also performed the same analyses for $a \to \pi^+\pi^-\pi^0$. We find that the results in this case are very similar to the case of $a \to \tau^+\tau^-$, since the final state $e^\pm$ spectrum arising from charged pion decay is similar to that arising from τ decay.

Our analysis here follows that of Ref. [2], where galactic propagation of $e^\pm$ is treated by the standard diffusion-loss equation. The primary injection spectra are calculated as described there, assuming a large mass hierarchy in each cascade step. In addition, tau decays are simulated using PYTHIA 8.1 [120]. We assume an NFW halo profile [36] and use the MED propagation model parametrization given in [34]. While there is significant uncertainty in the halo profile within a few kpc of the galactic center, its effect on the predicted $e^\pm$ fluxes is small. We treat the astrophysical background as in Refs. [2, 9]: we take the parameterization of [40] and marginalize over the overall slope P and normalization A in the range $-0.05 < P_{e^+,e^-} < 0.05$ and

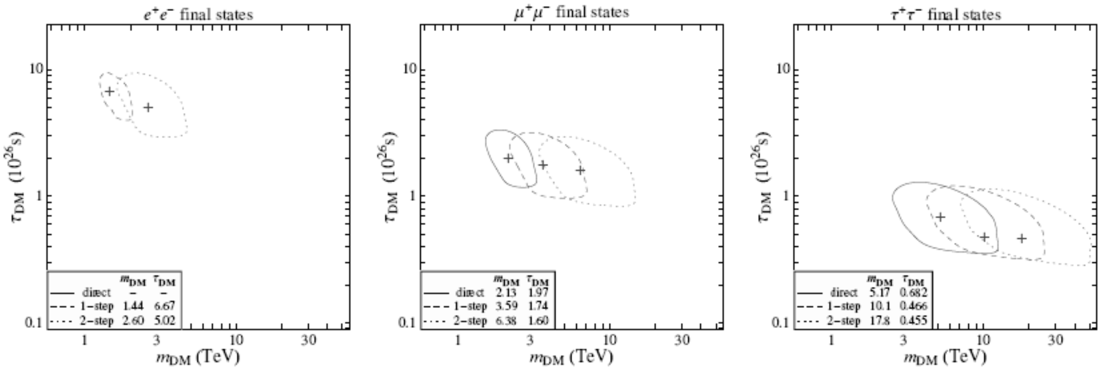

Figure 3.4: Regions of best fit (at 68% C.L.) to the PAMELA and FERMI data for dark matter mass $m_{\rm DM}$ and lifetime $\tau_{\rm DM}$, in the case of direct (solid), 1-step (dashed), and 2-step (dotted) decays into e^+e^-, $\mu^+\mu^-$, and $\tau^+\tau^-$. The best fit values of $m_{\rm DM}$ and $\tau_{\rm DM}$ are indicated by the crosses, and are displayed inset in units of TeV and 10^{26} sec, respectively. Direct decays into e^+e^- does not give a good fit. The case of $\pi^+\pi^-\pi^0$ is similar to that of $\tau^+\tau^-$.

$0 < A_{e^+,e^-} < \infty$. There remain substantial uncertainties in the background at the high energies explored by H.E.S.S., where primary electron fluxes depend strongly on individual sources within ≈ 1 kpc from the Earth. We therefore do not include the H.E.S.S. data in our fit procedure.

We performed a χ^2 analysis of signal plus background fluxes to the PAMELA and FERMI data. The PAMELA data at energies less than 10 GeV is strongly affected by solar modulation, and we exclude it from our analysis. The FERMI experiment released both statistical and systematic errors with their data. We conservatively combine these in quadrature, but note that this is likely an overestimation of the errors. The FERMI data is also subject to an overall systematic uncertainty in energy of $^{+5\%}_{-10\%}$, under which all energies are rescaled as $E \to rE$; we therefore also marginalize over r in the range $0.9 < r < 1.05$. The result for best fit regions of dark matter mass, $m_{\rm DM}$, and lifetime, $\tau_{\rm DM}$ is shown in Figure 3.4, for 1-step and 2-step cascades to electrons, muons and taus. For comparison, we also show the fits for direct decays. With 26 degrees of freedom (7 PAMELA + 26 FERMI − 7 fitting parameters), we plot 68% CL contours, corresponding to $\chi^2 = 28.8$. The best-fit values of $m_{\rm DM}$ and $\tau_{\rm DM}$ are indicated in each case.

We find that good fits are obtained in the region $m_{\rm DM} \approx O(1 - 100 \text{ TeV})$ and $\tau_{\rm DM} \approx O(10^{25} - 10^{27} \text{ sec})$, depending on the decay chain. In Figs. 3.5 and 3.6 we show the predicted $e^\pm$ fluxes compared to the PAMELA and FERMI data, using the best fit parameters obtained from the χ^2 analysis. The H.E.S.S. high energy data [42] is also overlaid, with the energy rescaled in each case to best match the predicted flux, within the ±15% range of overall systematic uncertainty in H.E.S.S.

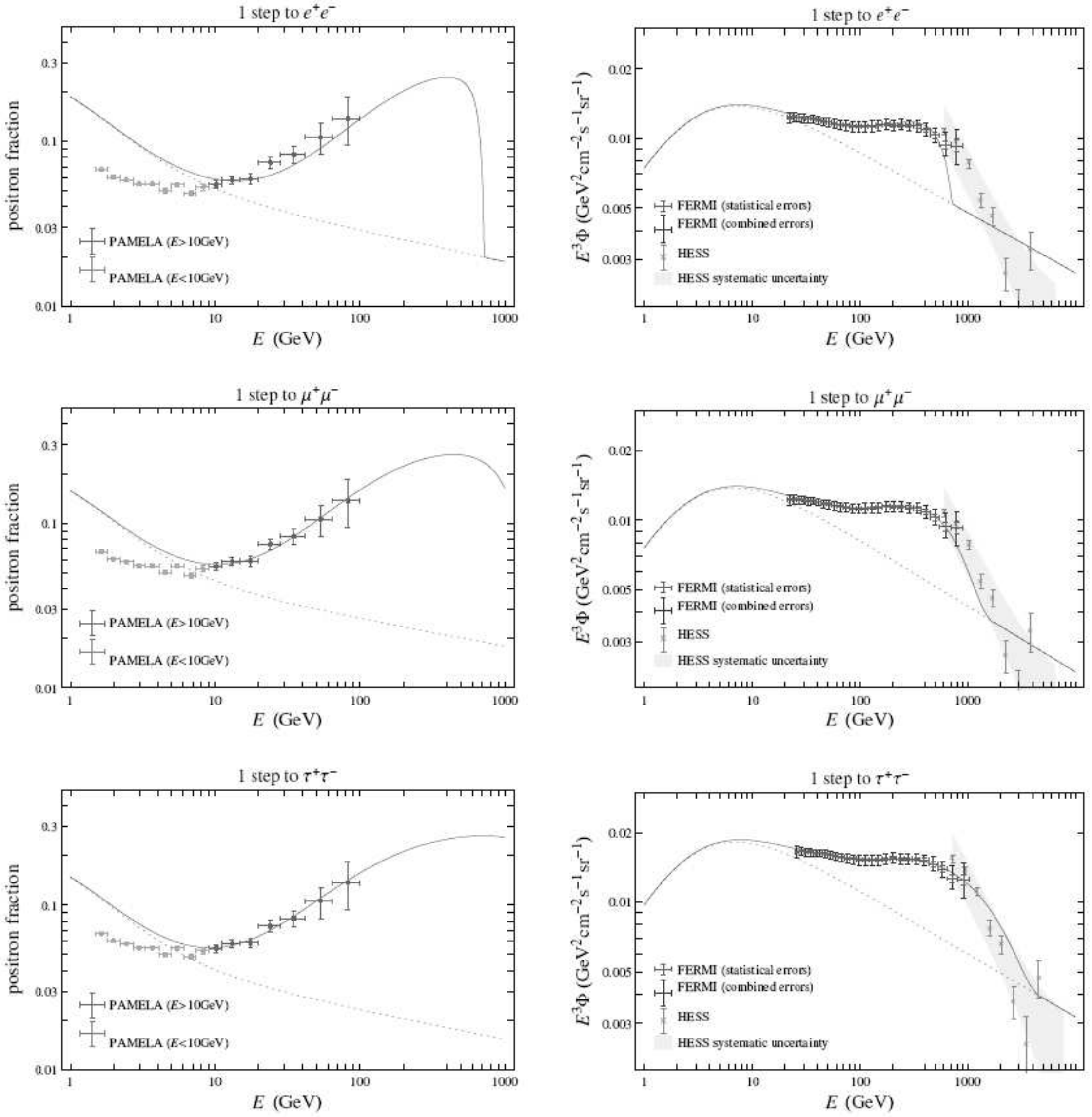

Figure 3.5: The predicted $e^{\pm}$ fluxes compared to the PAMELA and FERMI data for 1-step cascade decays into e^+e^-, $\mu^+\mu^-$, and $\tau^+\tau^-$. In each case, the mass and lifetime of dark matter are chosen at the best fit point indicated in Figure 3.4, with the background (dotted) and FERMI energy-normalization marginalized as described in the text. We overlay the H.E.S.S. data with energy rescaled in the range ±15% to best match the theory. Note that due to considerable uncertainty in the background fluxes at H.E.S.S. energies, direct comparison of predicted fluxes with the H.E.S.S. data may be misleading.

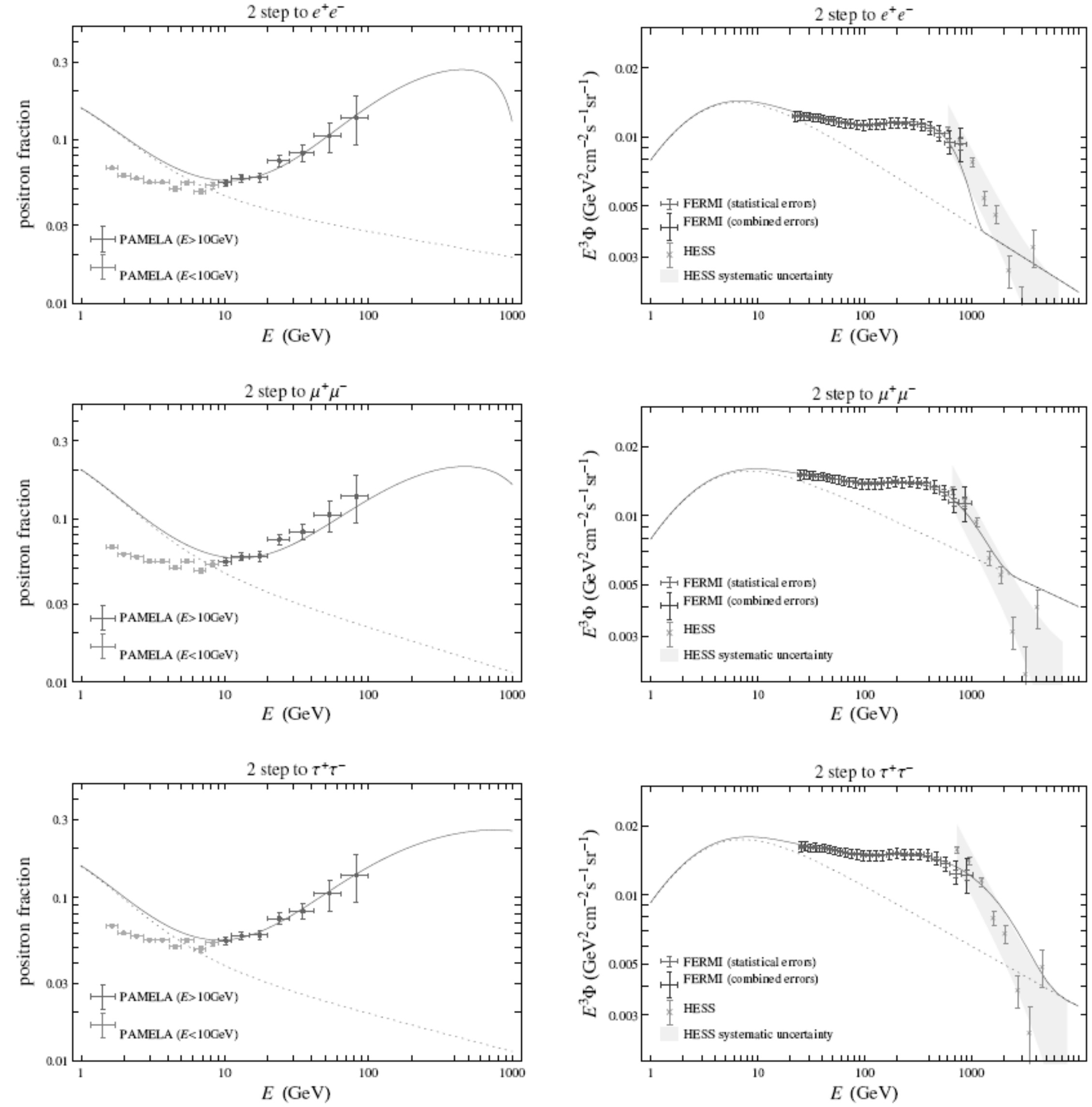

Figure 3.6: The same as Figure 3.5 for 2-step cascade decays into e^+e^-, $\mu^+\mu^-$, and $\tau^+\tau^-$.

energy. The agreement between the predictions and data is remarkable. We find some tension with the H.E.S.S. data in the case of 1-step to e^+e^-, but in all other cases the predicted curves are consistent with the H.E.S.S. data despite the fact that we did not use it in our fit procedure. Note that the background fluxes are very uncertain above ≈ 1 TeV, so that the precise comparison with the H.E.S.S. data may be misleading; for example, the background spectrum adopted here seems a bit too hard at the highest energies to be consistent with the H.E.S.S. data.

To summarize, we find that the electron/positron fluxes observed by PAMELA and FERMI are very well explained by dark matter decay in our scenario. The mass of the axion-like state can take almost any value in the wide range considered in Section 3.2.3, except for a small window at $\simeq 1.9 - 3.6$ GeV where a decays hadronically. More specifically, we find that the regions

$$\begin{array}{llll}
\text{(i)} & a \to e^+e^- & (2m_e < m_a < 2m_\mu) & f_a \approx O(100\ \text{TeV}), \\
\text{(ii)} & a \to \mu^+\mu^- & (2m_\mu < m_a \lesssim m_K - m_\pi) & f_a \approx O(10 - 100\ \text{TeV}), \\
\text{(ii)} & a \to \mu^+\mu^- & (m_K - m_\pi < m_a \lesssim 800\ \text{MeV}) & f_a \approx O(1 - 100\ \text{TeV}), \\
\text{(iii)} & a \to \pi^+\pi^-\pi^0 & (800\ \text{MeV} \lesssim m_a < 2m_p) & f_a \approx O(1 - 100\ \text{TeV}), \\
\text{(iv)} & a \to \tau^+\tau^- & (2m_\tau < m_a < 2m_b) & f_a \approx O(1 - 100\ \text{TeV}),
\end{array} \tag{3.50}$$

can all explain the cosmic ray $e^\pm$ data, without conflicting the bounds discussed in Section 3.2.5.

3.4.2 Diffuse gamma ray signals at FERMI

An immediate consequence of the framework described here is that the decay of dark matter will provide a source of γ rays throughout the dark matter halo, and extending up to energies around a few TeV. If the axion-like state decays into $\tau^+\tau^-$ or $\pi^+\pi^-\pi^0$, photons are produced directly by the decay of π^0s, while for e^+e^- and $\mu^+\mu^-$ modes there is a much smaller but significant source of γ rays from final state radiation (FSR) and inverse Compton scattering (ICS). Although the greatest fluxes would originate from the galactic center, where number densities are highest, the best direction to look for them is away from the galactic plane, where the background is much smaller and the signal still large. The FERMI experiment will measure γ-ray fluxes over the entire sky at energies up to several hundred GeV, which has the potential to resolve spectral features caused by dark matter decays [121, 122].

In Figure 3.7 we plot the contributions to the diffuse γ-ray fluxes for three illustrative decay modes: 1-step to $\tau^+\tau^-$, 1-step to $\pi^+\pi^-\pi^0$, and 2-step to $\mu^+\mu^-$. The first two cases are representative of any cascade to taus or pions, while the $\mu^+\mu^-$ curve illustrates the much lower flux for a decay mode with only FSR photons. Assuming an NFW profile, we average over all galactic latitudes greater than 10° from the galactic plane, representative of a diffuse γ-ray measurement by FERMI. The astrophysical background is modeled by a power law flux, $\propto E^{-2.7}$, taken from [123]. For the $\mu^+\mu^-$

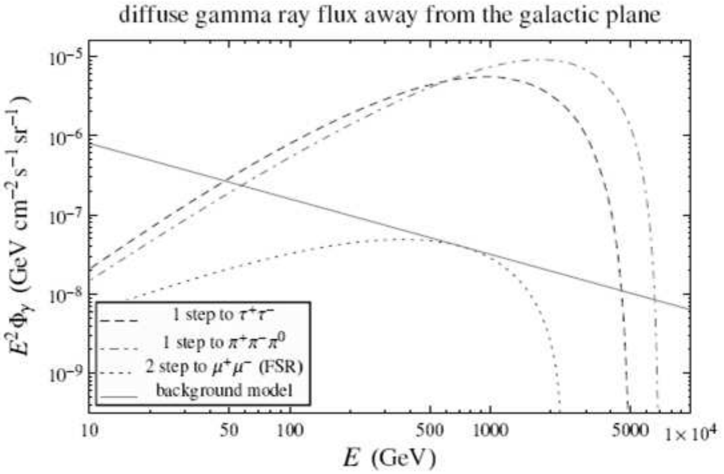

Figure 3.7: The high energy diffuse γ-ray spectrum away from the galactic plane, averaged over galactic latitudes above 10° assuming an NFW profile. Shown are the best fit parameters for 1-step to $\tau^+\tau^-$ (dashed), 1-step to $\pi^+\pi^-\pi^0$ (dot-dashed), and 2-step to $\mu^+\mu^-$ (dotted) dark matter decay modes. The γ-rays are due to π^0 decay in the case of 1-step to $\tau^+\tau^-$ and $\pi^+\pi^-\pi^0$, and to FSR in the case of 2-step to $\mu^+\mu^-$. The $\tau^+\tau^-$ and $\pi^+\pi^-\pi^0$ modes produce a bump in the flux clearly distinguishable from the background.

mode the flux shown is solely due to FSR, and we assume an a mass of 600 MeV. We have not shown the contribution from ICS, which, like FSR, is subdominant to directly produce photons for $\tau^+\tau^-$ and $\pi^+\pi^-\pi^0$ modes. At its peak, the ICS flux-component is expected to be comparable to the background, with a spectral shape somewhat different to that from FSR [116, 122], and could be significant for e^+e^- and $\mu^+\mu^-$ modes.

We find that signals from dark matter in our scenario can be seen in the diffuse γ-ray data. While the background is very uncertain, it is expected to be smooth compared to the strong, peaked fluxes seen for the $\tau^+\tau^-$ and $\pi^+\pi^-\pi^0$ decay modes, which should result in a clearly visible bump in the spectrum. The weaker signals from e^+e^- and $\mu^+\mu^-$ modes may also be seen. Since astrophysical sources are not expected to produce γ-ray fluxes with such prominent spectral features, measurements of diffuse γ-rays may serve to distinguish dark matter as the source of the PAMELA and FERMI excesses. Additionally, the shape and the strength of the γ-ray spectrum would convey information about the mass and decay channels of the dark matter. While the absence of an excess in upcoming FERMI data would not exclude our scenario, especially for the e^+e^- and $\mu^+\mu^-$ cases, a positive result would be a striking signature.

3.5 Collider Signatures

If the PAMELA and FERMI data is indeed indicative of dark matter with an $O(10\text{ TeV})$ mass, then direct production of dark matter is not possible at current collider experiments. However, the light axion-like states, which play a crucial role in determining the cosmic ray spectra, are kinematically accessible. We briefly describe some of the collider signatures for the axion-like state a.

The discovery potential for the axion-like state depends strongly on its mass and decay constant. Since we are considering decay constants in the range $f_a \approx O(1 - 100\text{ TeV})$, the coupling of a to the standard model is small, so discovery relies on the axion-like state having a clean decay mode. For $2m_e < m_a < 2m_\mu$, the decay length is generically greater than a kilometer, so any axion-like state produced in a collision will decay outside of the detector. In mass range $2m_\mu < m_a \lesssim 800$ MeV, a decays into $\mu^+\mu^-$ with a possible displaced vertex, offering a promising discovery channel. For $2m_\tau < m_a < 2m_b$, a decays promptly into taus, but neither leptonic taus nor hadronic taus are particularly clean channels. Similarly, there are large hadronic backgrounds to $a \to \pi^+\pi^-\pi^0$. Interestingly, while the $\tau^+\tau^-$ and $\pi^+\pi^-\pi^0$ channels are challenging in the collider context, they are precisely the ones that give the most striking diffuse γ-ray signal as seen in Section 3.4.2. In contrast, the $\mu^+\mu^-$ final state yields less dramatic diffuse γ-ray flux, but relatively clean collider signatures.

Direct production of a's at the LHC was considered in Ref. [88], where the a is produced in association with a hard ($p_T > 100$ GeV) jet via the gluon-gluon-a coupling. Since the a is boosted from the production, the resulting muon tracks from a decay have a mrad opening angle. If the decay constant $f_a \gtrsim (3 - 10)$ TeV, then the axion-like state lives sufficiently long that the decay $a \to \mu^+\mu^-$ happens with an $O(\text{cm})$ displaced vertex. As long as the decay constant $f_a \lesssim (15 - 30)$ TeV, then the production rate is sufficiently large to compete with the $B^0 \to D^\pm\mu^\mp\nu \to \mu^+\mu^-\nu\nu$ background. Therefore, direct production of a is a promising possibility for $f_a \sim 10$ TeV.

An alternative production mechanism for a's is via the Higgs boson. For the R and PQ symmetries considered in Section 3.2.3, the axion-like state has couplings to the Higgs fields, allowing the Higgs boson to decay into two axion-like states. For simplicity, we will focus on the decoupling limit as in Eq. (3.22). The Higgs decay width into two a's is then given by

$$\Gamma(h \to aa) = \frac{c_1^2}{64\pi}\frac{v^2 m_h^2}{f_a^4}, \tag{3.51}$$

where $c_1 = (1/4)\sin^2 2\beta$, and m_h is the Higgs boson mass. For a light Higgs boson, the dominant decay mode is into $b\bar{b}$ with (taking $m_b/m_h \to 0$)

$$\Gamma(h \to b\bar{b}) = \frac{3}{16\pi} m_h \left(\frac{m_b}{v}\right)^2. \tag{3.52}$$

Therefore, the branching ratio into two axion-like states is

$$\mathrm{Br}(h \to aa) \simeq \frac{c_1^2}{12}\frac{m_h^2 v^4}{m_b^2 f_a^4} \simeq 1.3 \times 10^{-5} \left(\frac{m_h}{120\ \mathrm{GeV}}\right)^2 \left(\frac{10\ \mathrm{TeV}}{f_a \tan\beta}\right)^4, \tag{3.53}$$

where we have used the large $\tan\beta$ approximation, $\sin 2\beta \approx 2/\tan\beta$, in the last equation. We see that the branching fraction for $h \to aa$ depends strongly on the decay constant as f_a^{-4}, and a sizable branching fraction can be obtained as f_a approaches 1 TeV. Since the decay constant is naturally expected to be somewhat ($\approx 4\pi$) smaller than the dynamical scale Λ as we saw in Eq. (3.14), this makes observation of the $h \to aa \to 4\mu$ signal at the LHC an interesting possibility [11]. The recent analysis of Ref. [124] focused on the $h \to aa \to 2\mu 2\tau$ channel in the case of $m_a \sim 5$ GeV. They find that generic event selection has an efficiency around 10%. Assuming a similar efficiency for $h \to aa \to 4\mu$ events, and taking the Higgs production at the LHC of ~ 50 pb, at least 10 events could be seen with 300 fb^{-1} of data for $f_a \tan\beta \lesssim 10$ TeV. In this way, direct a production (for larger values of f_a) and a production through the Higgs boson (for smaller values of f_a) are complementary. For larger m_a, the $h \to aa \to 6\pi$ and $h \to aa \to 4\tau$ channels may be visible if the background can be controlled. Note that the recent DØ analysis in Ref. [125] already gives the constraint $f_a \tan\beta \gtrsim 2$ TeV for $a \to \mu^+\mu^-$.

There has also been recent interest in looking for light bosons in low-energy high-luminosity lepton colliders [126, 127] as well as in fixed-target experiments [127]. From Eq. (3.19), the coupling of the axion-like state to electrons is proportional to m_e/f_a, which is smaller than 10^{-6} for $f_a > 1$ TeV, making the process $e^+e^- \to \gamma a$ beyond the reach of current lepton colliders. The feasibility of a fixed-target experiment to discover a depends on the a lifetime. If a decays promptly, then one must contend with a huge standard model background of prompt charged particle production, though Ref. [127] suggests that a coupling as small as 10^{-6} might be testable if a decays into $\mu^+\mu^-$. If a decays with a displaced vertex, then it could be discovered in traditional electron or proton beam dump experiments. Given the bounds from Figure 3.2 and the lifetimes in Eqs. (3.27, 3.28, 3.29), the possible values of $c\tau$ spans a huge range from tens of kilometers to less than a nanometer. If $a \to \mu^+\mu^-$, then $c\tau$ is plausibly in the millimeter to centimeter range, and could likely be discovered in an upgraded version of the experiment from Ref. [102].

3.6 Discussion and Conclusions

The origin of dark matter is one of the greatest mysteries in particle physics and cosmology. From the theoretical point of view, attentions have been focused on the WIMP paradigm: dark matter has mass $m_{\mathrm{DM}} \approx O(100\ \mathrm{GeV} - 1\ \mathrm{TeV})$ and couplings of weak interaction strength $g \approx O(1)$, leading to an annihilation cross section that gives the correct thermal relic abundance, $\Omega_{\mathrm{DM}} \simeq 0.2$. However, since the annihilation cross section depends on the combination g^2/m_{DM}, it should be equally convincing to consider the case where m_{DM} is heavier than the weak scale as long as the coupling g is larger. Such a situation arises naturally if dark matter is a composite state of some strong interaction, since the typical coupling g is expected to be larger than order unity and m_{DM} can be $O(10\ \mathrm{TeV})$.

Suppose that dark matter indeed arises from some strongly interacting sector. Then its stability may be the result of compositeness, and not of some exact symmetry imposed on the theory. This is precisely analogous to the case of the proton in the standard model embedded in some unified theory. If the proton (and pions) were elementary, it would immediately decay into e^+ and π^0 through a Lagrangian term $\mathcal{L} \sim pe\pi^0$. Since it is composite, however, the leading operator causing proton decay is already dimension six, $\mathcal{L} \sim qqql/M_*^2$, and the resulting lifetime is of order 10^{36} years for M_* of order the unification scale. In the case of composite dark matter, dimension six operators yield a lifetime of order 10^{25} sec for $m_{\mathrm{DM}} \approx 10$ TeV and $M_* \approx 10^{17}$ GeV. Decay of galactic dark matter could then have currently observable consequences.

The story just described implies that there is new strongly coupled physics beyond the weak scale, at $\approx O(10 - 100\ \mathrm{TeV})$. Interestingly, we already know an attractive framework where such a situation occurs—weak scale supersymmetry with low energy dynamical supersymmetry breaking. Since the superparticle masses in this framework arise at loop level, the scale of the strong sector is naturally larger than the weak scale by a one-loop factor $\approx 16\pi^2$. This picture is very much consistent with what is implied by the LEP precision electroweak data, namely that physics at the weak scale itself is weakly coupled. Yet such a setup can still explain the large hierarchy between the weak and Planck scales in, arguably, the simplest manner via dimensional transmutation.

It is interesting that this picture of dark matter arises precisely in the scenario where conventional LSP dark matter is lost—the LSP is now the very light gravitino. In fact, a gravitino with mass $m_{3/2} \lesssim O(10\ \mathrm{eV})$, implied by $\Lambda \approx O(10 - 100\ \mathrm{TeV})$, avoids various cosmological difficulties faced by other supersymmetry breaking scenarios. This allows us to consider the "standard" cosmological paradigm, based on inflation at a very early epoch with subsequent baryogenesis at high energies, consistently with supersymmetry. The standard virtues of weak scale supersymmetry, such as the stability of the weak scale and gauge coupling unification, are all preserved.

While composite dark matter in low-scale supersymmetry breaking already offers a consistent picture, this may not be the end of the story. Since dark matter is a part of a strongly interacting sector, it is possible that it feels additional dynamical effects. In particular, it is quite plausible that the sector spontaneously breaks an accidental global symmetry, leading to a light pseudo Nambu-Goldstone boson—again as in QCD. This raises the possibility that dark matter decays mainly into these light states (possibly through some other state), which then decay into standard model particles. In supersymmetric theories there is a natural candidate for such symmetry, an R symmetry, whose existence is suggested by a certain genericity argument associated with supersymmetry breaking. The mass of these light states can easily be in the MeV to 10 GeV range if explicit breaking arises from dimension five operators. Except in the mass range $m_a \simeq 1.9 - 3.6$ GeV, the decay products of the light states are naturally "leptonic" (specifically, e^+e^-, $\mu^+\mu^-$, $\pi^+\pi^-\pi^0$, or $\tau^+\tau^-$), with little nucleonic activity.

An illustrative model of this class was given in Section 3.3, and the required symmetry structure for the supersymmetry breaking sector was summarized in Table 3.1. Remarkably, the properties we have just obtained (with a little adjustment of parameters), are precisely what is needed to explain the recent cosmic ray data through dark matter physics:

- Dark matter mass is of $O(10$ TeV$)$,
- Dark matter lifetime is of $O(10^{26}$ sec$)$,
- Dark matter decays through (long) cascades,
- Dark matter decay final states are leptonic.

As we saw in Section 3.4, various mysterious features in the data—an unexpected rise of the positron fraction between ≈ 10 and 100 GeV in the PAMELA data, nonobservation of any anomaly in the PAMELA antiproton data, and a broad excess of the combined $e^\pm$ flux in the FERMI data—are all beautifully explained by the properties of dark matter discussed in this chapter. The resulting $e^\pm$ spectra are also consistent with the recent H.E.S.S. result. The success is quite remarkable, especially in view of the fact that the data is difficult to explain in terms of conventional WIMP annihilation—the mass scale suggested does not seem natural, the observed rate requires a large boost factor, and typical WIMP annihilation produces more antiprotons than indicated by PAMELA.

While dark matter with mass of order 10 TeV will not be produced at the LHC, the present scenario still has potential collider signatures. Since the light states generically have interactions with standard model gauge bosons, they may be produced at the LHC, and the leptonic decay of the light state could lead to visible signatures, especially if the dominant decay is into muons. The Higgs boson may also decay into the light states, producing a clean four lepton final state. Future astrophysical observations could also probe this scenario. For example, measurements of diffuse γ-ray could discriminate e/μ final states from τ/π final states. Moreover, the present framework may explain the discrepancy between the measured ^{7}Li abundance and the standard big-bang nucleosynthesis prediction by dimension five decay of some of the states in the supersymmetry breaking sector, e.g. (composite) messenger fields. Analysis of all these experimental data could provide important information about the structure of the supersymmetry breaking sector.

We finally mention that while in this chapter we focused on the case where dark matter arises from a strongly interacting supersymmetry breaking sector and decays through light states, some of our results apply in wider contexts. For example, quasi-stable dark matter in the supersymmetry breaking sector may decay directly into the SSM sector particles through dimension six operators. For example, quasi-stable mesons can decay into SSM (s)leptons $L_{\rm SSM}$ through the Kähler potential operators $K \sim Q_i^\dagger Q^j L_{\rm SSM}^\dagger L_{\rm SSM}/M_*^2 + \bar{Q}^{\dagger\bar{\imath}} \bar{Q}_{\bar{\jmath}} L_{\rm SSM}^\dagger L_{\rm SSM}/M_*^2$. In these cases, the final states of the decay are determined by a combination of gravitational scale physics and TeV-scale superparticle spectra, not through cascades associated with light states. However, all other points regarding compositeness, long lifetime, relatively large mass, and thermal abundance still persist. The dynamics of dark matter discussed here can also be applied in non-supersymmetric theories—all we need is some strong dynamics at $\approx O(10 - 100 \text{ TeV})$ satisfying the properties of Table 3.1. Examples of such theories may include ones in which the Higgs fields arise as pseudo Nambu-Goldstone bosons of some strong dynamics [128].

As the LHC starts running this year, we anticipate great discoveries. A possible connection between weak scale physics and dark matter is one of the major themes to be explored at the high energy frontier. The standard expectation is to study the properties of a dark matter particle by producing it at the LHC. Although the scenario presented in this chapter does not allow this, important physics associated with the dark sector may still be probed. With many new particle physics and astrophysics observations on the horizon, the next decade will certainly be exciting for potentially understanding the origin and properties of dark matter. While nature may not show us the "standard" WIMP dark matter story, it may still reveal a beautiful connection between dark matter and the weak scale through hidden sector dynamics.

Chapter 4

A Definitive Signal of Multiple Supersymmetry Breaking

4.1 Introduction

At first glance, particle colliders do not appear particularly well-suited to the task of probing the fundamental structure of gravity. Indeed, given the intrinsic energy limitations of present day and future machines, any direct experimental handle on Planck scale physics continues to be a rather remote possibility. Nevertheless, weak scale supersymmetry (SUSY) may provide a unique window into genuinely gravitational physics because SUSY is a symmetry of spacetime.

In particular, if SUSY is realized as a local symmetry, namely supergravity (SUGRA), then there necessarily exists a spin-3/2 superpartner of the graviton: the gravitino. The gravitino has a mass, $F/\sqrt{3}M_{\rm Pl}$, and couplings to observable sector fields, $\sim 1/F$, which obey a fixed relationship determined by the Planck scale, $M_{\rm Pl}$. Because the existence of the gravitino is mandatory, it is an attractive possibility that this state comprises the dark matter of the universe. In this case, the lightest observable-sector supersymmetric particle (LOSP) may be charged, and precision studies of the LOSP decay into the gravitino can provide a robust test of the expected gravitino mass/interaction relation and therefore an indirect measurement of $M_{\rm Pl}$ [129, 130]. This would offer compelling evidence for the validity of SUGRA as well as a genuine probe of gravitational physics at particle colliders.

Unfortunately, this most spectacular signal is in direct conflict with big bang nucleosynthesis (BBN). At colliders, $M_{\rm Pl}$ can only be measured if the gravitino is sufficiently heavy: $m_{3/2} \gtrsim O(0.1) m_{\rm LOSP}$. However, unless the gravitino is sufficiently light, $m_{3/2} \lesssim O(1-10 \text{ GeV})$, then late-time charged LOSP decays destroy the successful predictions for the abundance of light elements [131, 132]. Thus, if the gravitino is to be heavy enough for a successful collider measurement, one must resort to a rather non-standard cosmology in which the thermal history is modified below a tempera-

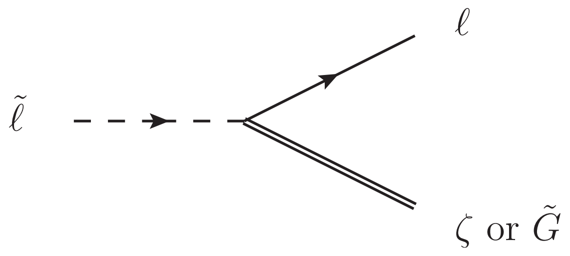

Figure 4.1: Slepton LOSP decay into a goldstino or a gravitino.

ture of $O(0.1)m_{\text{LOSP}}$. Additionally, thermal leptogenesis [74]—arguably the simplest mechanism for baryogenesis—does not work for the small values of $m_{3/2}$ required by the BBN constraint unless the gravitino is extremely light ($m_{3/2} \lesssim 10$ eV). This is a consequence of gravitino overproduction from the high temperature plasma [70, 133] and constraints from structure formation [73].

It is interesting to note, however, that the BBN bound actually has nothing to do with the gravitino itself—it has to do with the late decaying LOSP injecting energies during or after BBN. Therefore, if there is an additional state to which the LOSP can decay more quickly, then the constraint from BBN may be avoided. However, this new state often introduces its own cosmological problems, and is not necessarily theoretically motivated.

In this paper, we show that a promising new state does in fact exist: an uneaten goldstino. This mode arises naturally in the general framework of Ref. [134], where multiple sectors separately break SUSY, yielding a corresponding multiplicity of goldstini. In this framework, the gravitino couplings are not modified, but the LOSP can decay faster to an uneaten goldstino, nullifying the usual BBN constraint. Moreover, in the limit where the SUSY breaking sectors are mutually sequestered, the goldstini acquire a mass from SUGRA effects which is exactly twice the gravitino mass. Intriguingly, this factor of 2 is entirely fixed by the symmetries of SUGRA.

As we will see, the scenario outlined above leads to completely consistent cosmologies with a heavy gravitino $m_{3/2} \approx O(10 - 100 \text{ GeV})$. This allows one to probe SUGRA via precision studies of charged LOSP decays at the LHC. Furthermore, the LOSP will generically have non-negligible branching fractions into both the gravitino and a goldstino (see Fig. 4.1), allowing for a measurement of the relative factor of 2 between their masses. Measuring M_{Pl} and observing this "smoking gun" factor of 2 would reveal a number of exceedingly deep facts about our universe—not only that SUGRA is correct, but also that SUSY breaking is a generic phenomenon and sequestering is realized in nature. These in turn suggest the existence of extra dimensions in which sequestering is naturally realized.

We find it remarkable that consistent cosmological histories happen to favor regions of parameter space in which dramatic LHC signatures are accessible. In fact, by requiring thermal leptogenesis, the gravitino mass must be larger than ≈ 10 GeV, with the right abundance for gravitino dark matter obtained for reheating temperatures $T_R \approx (10^9 - 10^{10})$ GeV. This setup is possible if the goldstino interactions satisfy certain simple conditions, namely that they preserve an R symmetry. More generally, consistent cosmologies are obtained with T_R as high as $\approx 10^7$ GeV, in which case dark matter is dominantly the goldstino. In both these cases, cosmology prefers the LOSP branching ratios into gravitinos and goldstinos to be not too dissimilar.

The remainder of the paper is organized as follows. We review the collider tests of SUGRA and their tension with BBN in Sec. 4.2, and show how modified LOSP decays can simply relieve this tension. In Sec. 4.3, we summarize the framework of multiple SUSY breaking and the important properties of the resulting goldstini [134]. The collider phenomenology of gravitinos/goldstinos is discussed in Sec. 4.4, and their cosmology is studied in Sec. 4.5, where the relevant calculation of goldstino relic abundance is summarized in the Appendix. The possibility of colored LOSPs is discussed in Sec. 4.6. Finally, we conclude in Sec. 4.7.

4.2 BBN and the LHC

Testing the relationship between the mass and interaction strength of the gravitino requires precision collider measurements which are only feasible if the LOSP is charged. Typically, the LOSP is taken to be a long-lived slepton (most commonly a stau) because this is favored in many SUSY breaking mediation schemes. While other charged states are also possible, we will mostly focus on a slepton LOSP in this paper, leaving a discussion of other possibilities to Sec. 4.6.

At the LHC, quasi-stable charged sleptons may be copiously produced at the end of SUSY cascade decays. Most of them will exit the interaction region appearing as "heavy muons." The slepton mass can then be determined from a combination of time-of-flight and momentum information [135]. Through ionization energy loss, a fraction of the produced sleptons will also be trapped inside the main detector [136] or in a separate stopper detector [137, 130], where their decays can be precisely studied.

The decay rate of the slepton is measured by observing the lifetime of stopped sleptons. In the conventional SUSY setup, a slepton decays to a lepton and a gravitino, with a width given by

$$\Gamma_{\tilde{\ell}\to\ell\tilde{G}} \simeq \frac{m_{\tilde{\ell}}^5}{16\pi F_{\rm tot}^2}, \tag{4.1}$$

where $F_{\rm tot}$ is the scale of SUSY breaking, and we have ignored the relatively unimportant phase space factor. From the energy spectrum of the outgoing lepton and the measured slepton mass, one can also determine the gravitino mass, which is fixed by theory to be

$$m_{3/2} \simeq \frac{F_{\rm tot}}{\sqrt{3}M_{\rm Pl}}. \tag{4.2}$$

The gravitino mass/interaction relation can then be tested [129] by combining the measured values of $\Gamma_{\tilde{\ell}\to\ell\tilde{G}}$ and $m_{3/2}$ to form the Planck scale $M_{\rm Pl}$

$$M_{\rm Pl}^2 \simeq \frac{m_{\tilde{\ell}}^5}{48\pi\Gamma_{\tilde{\ell}\to\ell\tilde{G}}m_{3/2}^2}, \tag{4.3}$$

and comparing it with the value obtained in long distance measurements of gravity.

However, an indirect measurement of $M_{\rm Pl}$ is only possible if the mass of the gravitino is sufficiently heavy that it can be experimentally determined. In particular, for a given slepton decay, $m_{3/2}$ is reconstructed from the slepton mass and the energy of the outgoing lepton E_ℓ according to

$$m_{3/2} = \sqrt{m_{\tilde{\ell}}^2 + m_\ell^2 - 2m_{\tilde{\ell}}E_\ell}. \tag{4.4}$$

Thus, the error in $m_{3/2}$ is given by

$$\frac{\mathit{\Delta} m_{3/2}}{m_{3/2}} \simeq \frac{m_{\tilde{\ell}}^2}{2m_{3/2}^2}(\mathit{\Delta}_m \oplus \mathit{\Delta}_E), \tag{4.5}$$

where $\mathit{\Delta}_m \equiv \mathit{\Delta} m_{\tilde{\ell}}/m_{\tilde{\ell}}$ and $\mathit{\Delta}_E \equiv \mathit{\Delta} E_\ell/E_\ell$. With sufficient statistics, we expect that $\mathit{\Delta} m_{\tilde{\ell}}$ and $\mathit{\Delta}_E$ can reach the level of (0.1 – 1)% at the LHC [135, 138]. This implies that the $M_{\rm Pl}$ measurement is possible for

$$m_{3/2} \gtrsim (0.05 - 0.2)m_{\tilde{\ell}}, \tag{4.6}$$

where we have required $\mathit{\Delta} m_{3/2} \ll m_{3/2}$. Of course, the precise numbers are subject to the level of experimental accuracy which may ultimately be achieved.

In standard SUSY, the mass and interaction strength of the gravitino obey a fixed relation, so any theory with a gravitino heavy enough to satisfy Eq. (4.6) will have commensurately long-lived sleptons. As a consequence, this class of theories is in direct tension with BBN. Specifically, sleptons produced in the early universe will decay during or after BBN and potentially alter the abundances of light elements. As seen in Ref. [132], the BBN constraint on late-decaying slepton LOSPs implies

$$m_{3/2} \lesssim \begin{cases} 0.35\ \text{GeV}\left(\frac{m_{\tilde{\ell}}}{100\ \text{GeV}}\right)^{2.3} & \text{for } m_{\tilde{\ell}} \lesssim 400\ \text{GeV}, \\ 20\ \text{GeV}\left(\frac{m_{\tilde{\ell}}}{1\ \text{TeV}}\right)^{1.0} & \text{for } m_{\tilde{\ell}} \gtrsim 400\ \text{GeV}. \end{cases} \tag{4.7}$$

Here a typical primordial slepton yield of $Y_{\tilde{\ell}} \simeq 7 \times 10^{-14}(m_{\tilde{\ell}}/100\ \text{GeV})$ was assumed, but the bound depends only weakly on this value. Thus, one sees that the criterion for measuring $M_{\rm Pl}$ at colliders, Eq. (4.6), is in conflict with the BBN bound in conventional SUSY theories. Note that the couplings of the gravitino are completely fixed by $m_{3/2}$, so there is no freedom to modify the slepton decay width to the gravitino.

Nevertheless, while the *partial width* of the slepton into the gravitino is fixed by SUGRA, it is of course possible to change the *total width* of the slepton. By introducing a new light degree of freedom ζ and a new decay mode

$$\tilde{\ell} \to \ell\zeta, \tag{4.8}$$

the slepton can decay much more quickly and thus evade constraints from BBN. In fact, a new field ζ arises quite naturally in the framework of multiple sector SUSY breaking, where ζ is identified as an *uneaten* goldstino. We will review this framework in the next section.

In order to test the gravitino mass/interaction relation at the LHC, it is necessary that the slepton has a non-negligible branching fraction to gravitinos. Assuming that there are $O(10^3 - 10^4)$ stopped LOSPs (which correspond to relatively light superpartners with $(100 - 1000)$ fb^{-1} of integrated luminosity [130]) we need $\mathrm{Br}_{\tilde{\ell}\to\ell\tilde{G}} \gtrsim O(10^{-4} - 10^{-3})$.

In summary, in order to measure $M_{\rm Pl}$ at colliders and simultaneously evade constraints from BBN, the following conditions must be satisfied:

$$\Gamma_{\tilde{\ell}\to\ell\zeta} \gtrsim \begin{cases} 9.1\times 10^{-29}\ \text{GeV}\left(\frac{m_{\tilde{\ell}}}{100\ \text{GeV}}\right)^{0.4} & (m_{\tilde{\ell}} \lesssim 400\ \text{GeV}), \\ \\ 2.8\times 10^{-27}\ \text{GeV}\left(\frac{m_{\tilde{\ell}}}{1\ \text{TeV}}\right)^{3.0} & (m_{\tilde{\ell}} \gtrsim 400\ \text{GeV}), \end{cases} \tag{4.9}$$

$$\frac{\Gamma_{\tilde{\ell}\to\ell\tilde{G}}}{\Gamma_{\tilde{\ell}\to\ell\zeta}} \gtrsim O(10^{-4} - 10^{-3}), \tag{4.10}$$

$$m_{3/2} \gtrsim (0.05 - 0.2) m_{\tilde{\ell}}, \tag{4.11}$$

where the first condition has been translated from Eq. (4.7) and so has a mild dependence on the primordial LOSP yield $Y_{\tilde{\ell}}$.

As shown in Ref. [134] and reviewed below, the mass of an uneaten goldstino is fixed by the symmetries of SUGRA to be $2m_{3/2}$. Consequently, if the gravitino mass is heavy enough to be determined at colliders, then so too is the mass of the goldstino. Thus, we are presented with the intriguing prospect of measuring *both* decay channels to gravitino and goldstino, as well as the remarkable factor of 2 in the mass relation.

4.3 Review of Goldstini Framework

In principle, any light mode ζ which couples with sufficient strength to the LOSP can nullify BBN constraints. Here we will focus on the framework introduced in Ref. [134], where ζ is an uneaten goldstino which arises in the context of multiple sector SUSY breaking. We find this a particularly attractive possibility both because it is well-motivated from top-down considerations and because it allows for a direct experimental probe of the fundamental properties of spacetime at colliders. In what follows, we briefly review the case of two sectors which independently break SUSY, and refer the interested reader to Ref. [134] for a significantly more detailed treatment.

Consider two sectors which separately experience F-term SUSY breaking at the scales F_1 and F_2, yielding two corresponding goldstini fields, η_1 and η_2. (We take $F_1 > F_2$ without loss of generality.) Because SUSY is a local symmetry, a diagonal combination of these goldstini is eaten by the gravitino via the super-Higgs mechanism, while the remaining orthogonal mode persists as a physical degree of freedom. We can go to the physical mass basis via the transformation

$$\begin{pmatrix} \eta_1 \\ \eta_2 \end{pmatrix} = \begin{pmatrix} \cos\theta & -\sin\theta \\ \sin\theta & \cos\theta \end{pmatrix} \begin{pmatrix} \eta_{\text{long}} \\ \zeta \end{pmatrix}, \tag{4.12}$$

where $\tan\theta = F_2/F_1$. Here η_{long} is the longitudinal mode of the gravitino, while ζ is the uneaten goldstino which remains in the spectrum. Since the overall scale of SUSY breaking is $F_{\text{tot}} = \sqrt{F_1^2 + F_2^2}$, the gravitino mass is $m_{3/2} = F_{\text{tot}}/\sqrt{3}M_{\text{Pl}}$.

The couplings of each goldstino to chiral and vector superfields of the supersymmetric standard model (SSM) are

$$\mathcal{L}_\phi = \left(\frac{\tilde{m}_1^2}{F_1}\eta_1 + \frac{\tilde{m}_2^2}{F_2}\eta_2\right)\psi\phi^\dagger + \text{h.c.}, \tag{4.13}$$

$$\mathcal{L}_\lambda = -\frac{i}{\sqrt{2}}\left(\frac{M_1}{F_1}\eta_1 + \frac{M_2}{F_2}\eta_2\right)\sigma^{\mu\nu}\lambda F_{\mu\nu} + \text{h.c.}, \tag{4.14}$$

where ϕ, ψ, and λ represent SSM scalars, fermions, and gauginos, respectively. The soft mass terms $\tilde{m}_{1,2}^2$ and $M_{1,2}$ are the contributions to the scalar squared masses and gaugino masses from sectors 1 and 2, respectively. We primarily consider a regime in which the SUSY breaking scale of sector 1 is sufficiently larger than that of sector 2, so that $F_{\text{tot}} \approx F_1 \gg F_2$. In this limit, the couplings are

$$\mathcal{L}_\phi \approx \left(\frac{\tilde{m}_1^2 + \tilde{m}_2^2}{F_{\text{tot}}}\eta_{\text{long}} + \frac{\tilde{m}_2^2}{F_2}\zeta\right)\psi\phi^\dagger + \text{h.c.}, \tag{4.15}$$

$$\mathcal{L}_\lambda \approx -\frac{i}{\sqrt{2}}\left(\frac{M_1 + M_2}{F_{\text{tot}}}\eta_{\text{long}} + \frac{M_2}{F_2}\zeta\right)\sigma^{\mu\nu}\lambda F_{\mu\nu} + \text{h.c.} \tag{4.16}$$

As long as $\tilde{m}_2^2$ and M_2 are not too small, the SSM fields will couple more strongly to the uneaten goldstino ζ than to the longitudinal mode of the gravitino η_{long}, allowing for substantial departures from usual SUGRA signatures.

In Ref. [134], it was shown that ζ (and more generally, any additional uneaten goldstini) acquires a mass

$$m_\zeta = 2m_{3/2} + \delta m, \tag{4.17}$$

where δm vanishes in the limit that sectors 1 and 2 are sequestered from each other. We note that the ratio $m_\zeta/m_{3/2} = 2$ is truly a SUGRA prediction, and measuring this ratio would give valuable insight into the structure of spacetime, independent of details of the mechanism of SUSY breaking.

Below we will also consider scenarios in which sectors 1 and 2 both couple to the SSM, in which case the sequestered limit is only an approximation. While direct interactions between sectors 1 and 2 are induced through loops of SSM fields, the resulting δm is generally a loop factor or more down in size from SSM soft masses [134] and can be ignored in most of the parameter regions we will be interested.

4.4 Gravitino and Goldstini at Colliders

In this section, we will consider the collider phenomenology of LOSP decays to gravitinos and goldstini. For simplicity, we focus on the case of two SUSY breaking sectors, with $F_1 > F_2$. We will be concerned with the regime in which $\tilde{m}_1^2 \lesssim \tilde{m}_2^2$, so that the SSM fields couple more strongly to the uneaten goldstino ζ than to the gravitino $\tilde{G}$. The opposite regime has phenomenology which is essentially identical to that of standard SUSY.

Consider the limiting case $\tilde{m}_1^2 \ll \tilde{m}_2^2$; extensions to more general cases are straightforward. In this limit, the partial widths of the LOSP into the gravitino and the goldstino take particularly simple forms. As in Sec. 4.2, we assume a charged slepton LOSP, so

$$\Gamma_{\tilde{\ell}\to\ell\tilde{G}} \simeq \frac{m_{\tilde{\ell}}^5}{16\pi F_{\rm tot}^2}, \tag{4.18}$$

$$\Gamma_{\tilde{\ell}\to\ell\zeta} \simeq \frac{m_{\tilde{\ell}}^5}{16\pi F_2^2}, \tag{4.19}$$

where we have dropped phase space factors for simplicity. Using the formulas from Sec. 4.2, let us now determine the region of parameter space in which the BBN bound is satisfied and the gravitino (and goldstino) masses can be measured at the LHC. As discussed in Ref. [134], the decay rate of goldstinos to gravitinos is cosmological and therefore irrelevant for our discussions here.

The regions of parameter space which satisfy Eqs. (4.9) and (4.11) are shown in Fig. 4.2 (Fig. 4.3) for $m_{\tilde{\ell}} = 100$ GeV (300 GeV). The left and right panels depict these allowed regions in the $m_{3/2}$–$\tau_{\tilde{\ell}}$ and F_1–F_2 planes, respectively, where $\tau_{\tilde{\ell}}$ is the LOSP lifetime. In producing these plots, we have included the phase space factors and higher order terms in F_2/F_1 which are omitted in Eqs. (4.18) and (4.19). In each plot, the region below the solid line is allowed by BBN, while the regions right of the vertical, dashed lines satisfy Eq. (4.11) (with the two lines corresponding to $m_{3/2}/m_{\tilde{\ell}} = 0.05$ and 0.2). The two dotted lines represent the cosmological bound discussed in the next section. The labeled contours denote the branching ratio of $\Gamma_{\tilde{\ell}\to\ell\tilde{G}}/\Gamma_{\tilde{\ell}\to\ell\zeta}$, which must be sufficiently large if we are to be able to see LOSP decays to both gravitinos and goldstinos.

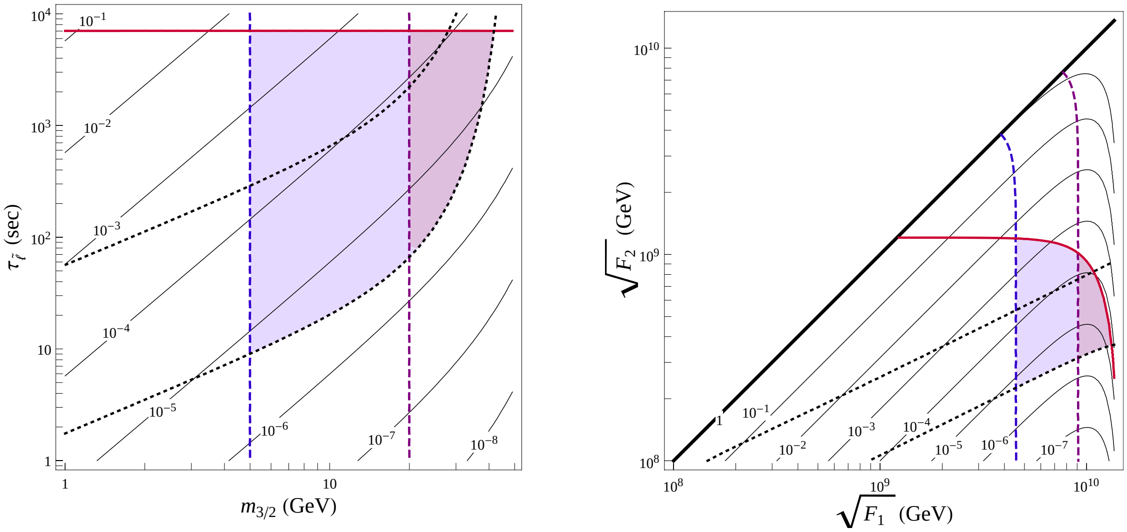

$\Gamma_{\tilde{\ell}\to\ell\tilde{G}}/\Gamma_{\tilde{\ell}\to\ell\zeta}$ for $m_{\tilde{\ell}} = 100$ GeV

Figure 4.2: Contours of the branching ratio $\Gamma_{\tilde{\ell}\to\ell\tilde{G}}/\Gamma_{\tilde{\ell}\to\ell\zeta}$ (labeled, solid black) together with constraints from cosmology and collider physics for $m_{\tilde{\ell}} = 100$ GeV, shown in the $m_{3/2}$-$\tau_{\tilde{\ell}}$ plane (left) and in the $\sqrt{F_1}$-$\sqrt{F_2}$ plane (right). The BBN bound excludes the parameter regions above the solid red lines, while goldstino overproduction from SSM sfermion decays excludes the regions below the dotted lines (the two dotted lines in each plot correspond to $r \equiv m_{\tilde{Q}}/m_{\tilde{L}} = 3$ (lower) and 10 (upper); see Sec. 4.5.1). Demanding that the gravitino is heavy enough to be measured at colliders places a lower bound on the gravitino mass depending on experimental resolutions, restricting to the regions right of the vertical dashed lines (blue for $m_{3/2} > 0.05 m_{\tilde{\ell}}$ and purple for $m_{3/2} > 0.2 m_{\tilde{\ell}}$). The parameter regions consistent with all the constraints are shaded. To read off analogous bounds on the conventional SUSY setup, simply restrict to the line $F_1 = F_2 \equiv F$.

A number of important facts are evident from these plots. In particular, we can immediately see the direct conflict between collider signatures and BBN in conventional SUSY by considering the plot on the right panel and restricting to the diagonal line $F_1 = F_2 \equiv F$. As expected, along this line, there is no region of parameter space in which the gravitino is heavy enough to be measured at colliders and also simultaneously consistent with BBN constraints. However, moving down and to the right (regions with $F_2 < F_1$), we find that a viable parameter space does open up. Nonetheless, even this region of parameter space is limited by cosmological considerations, as we will see in the next section. The viable parameter space is thus a finite region in the F_1–F_2 (and $m_{3/2}$–$\tau_{\tilde{\ell}}$) plane, so that the branching ratio $\Gamma_{\tilde{\ell}\to\ell\tilde{G}}/\Gamma_{\tilde{\ell}\to\ell\zeta}$ has a lower bound, which is of $O(10^{-5})$ or so. This value is not far from the limit of LHC observability, given in Eq. (4.10). It is also interesting that resulting LOSP lifetimes,

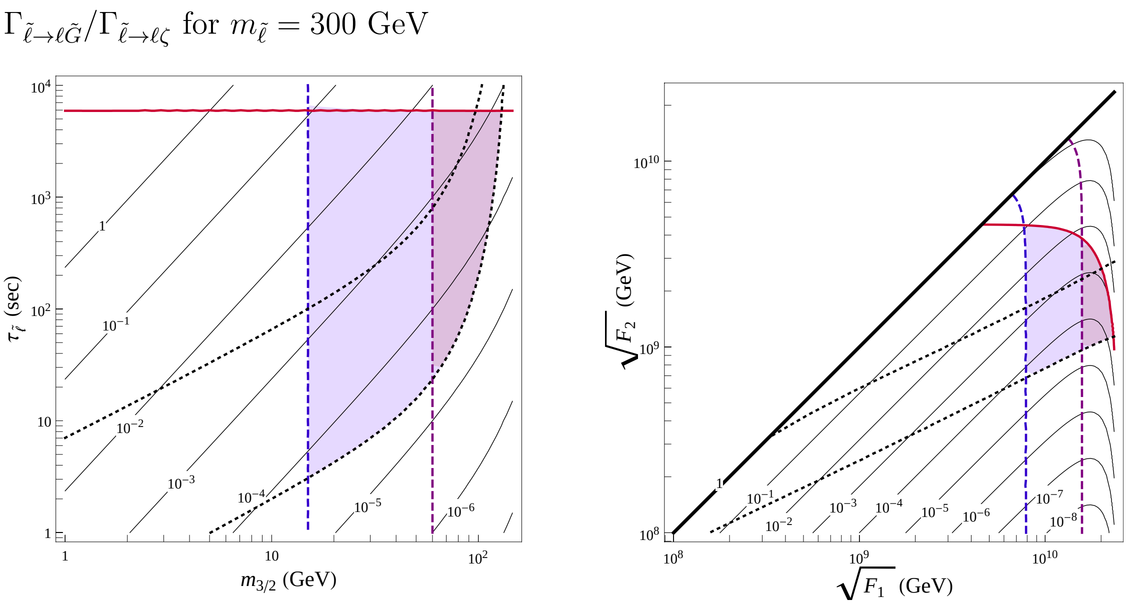

Figure 4.3: The same as Fig. 4.2 but for $m_{\tilde{\ell}} = 300$ GeV.

$\tau_{\tilde{\ell}} \approx O(1 - 10^4 \text{ sec})$, are within the range in which stopped LOSP decays may be observed in the main detector [136].

In order to measure the Planck scale from decays of long-lived charged LOSPs, we form a combination of the LOSP mass and lifetime and the mass of the invisible LOSP decay product; see Eq. (4.3). If the decay product is indeed the gravitino, this should reproduce the true Planck scale, $M_{\rm Pl}$. In our case, however, the LOSP decays mainly into ζ, so that the measured "Planck scale", "$M_{\rm Pl}$", will deviate from $M_{\rm Pl}$ by

$$\text{“}M_{\rm Pl}\text{”}^2 \equiv \frac{m_{\tilde{\ell}}^5}{48\pi\Gamma_{\tilde{\ell}\to\ell\zeta}m_\zeta^2} = M_{\rm Pl}^2 \frac{\Gamma_{\tilde{\ell}\to\ell\tilde{G}}}{\Gamma_{\tilde{\ell}\to\ell\zeta}} \frac{m_{\tilde{G}}^2}{m_\zeta^2}, \tag{4.20}$$

where again we have dropped phase space factors for the sake of clarity. Consequently, we expect to measure a value for "$M_{\rm Pl}$" which is slightly (one or two orders of magnitude) lower than $M_{\rm Pl}$. Interestingly, the measured value of "$M_{\rm Pl}$" can be used to *precisely* fix the branching ratio of the LOSP to the gravitino

$$\frac{\Gamma_{\tilde{\ell}\to\ell\tilde{G}}}{\Gamma_{\tilde{\ell}\to\ell\zeta}} \simeq 4\left(\frac{\text{“}M_{\rm Pl}\text{”}}{M_{\rm Pl}}\right)^2, \tag{4.21}$$

where $m_\zeta \simeq 2m_{3/2}$ has been used. Thus, by measuring "$M_{\rm Pl}$" we know how many stopped LOSPs are necessary to observe the second peak in E_ℓ which corresponds to the gravitino. The Planck scale constructed from this second peak should then reproduce the value obtained by macroscopic measurements, $M_{\rm Pl}$.

4.5 Viable Cosmologies

It is reasonable to ask to what extent the collider signature discussed in the previous section is consistent with cosmology. For example, if the reheating temperature, T_R, is smaller than the SSM superparticle mass scale, then the only constraints on the masses and couplings of gravitinos and goldstinos come from BBN. If T_R is smaller than the LOSP freezeout temperature, then even the constraint from BBN disappears.

However, most standard cosmologies require a significantly higher reheating temperature, in which case one must evade constraints from the overproduction of gravitinos and goldstinos as well as the BBN bound. We discuss these constraints in Sec. 4.5.1, and present a number of consistent cosmological scenarios with high T_R in the subsequent subsections. In each setup, either the goldstino or the gravitino could comprise the dark matter of the universe. Throughout this section, we assume the absence of significant entropy production below T_R, which is indeed the case for most standard cosmologies.

4.5.1 Reheating Bounds on Goldstini Couplings

Avoiding goldstino/gravitino overproduction in the early universe may provide bounds on T_R and their interactions. In the case of the gravitino, this sets a robust upper bound on T_R as a function of $m_{3/2}$ [70, 133]. In contrast, the bounds from goldstino overproduction depend on the goldstino interactions with the SSM fields—unlike the gravitino, the goldstino can have couplings to the SSM which are not universal.

Suppose that sector 2 provides soft mass contributions to all the SSM superparticles. In this case, the goldstino couples to SSM fields (almost) universally. Since its couplings are larger than those of the gravitino by a factor of $F_{\rm tot}/F_2$, the overproduction bound is correspondingly more stringent. In particular, the standard gravitino overproduction bound can be straightforwardly translated into a bound on goldstino overproduction via Ref. [134]

$$T_R^{\rm max} \approx 10^5 \text{ GeV} \left(\frac{10 \text{ GeV}}{m_\zeta}\right) \left(\frac{\sqrt{F_2}}{10^9 \text{ GeV}}\right)^4, \tag{4.22}$$

for $T_R^{\rm max}$ larger than the SSM superparticle masses. As in the case of the gravitino, the production of goldstinos in this case is dominated at high temperatures by processes involving gauge–gaugino–goldstino vertices. This is because these vertices are dimension 5 operators.

As shown in Sec. 4.5.3, however, the gauge–gaugino–goldstino interactions can be effectively removed using an R symmetry. In this case, the bound from cosmological goldstino overproduction is far milder, since the goldstino couples very weakly to the gauginos. Instead, the leading overproduction bound arises from processes involving

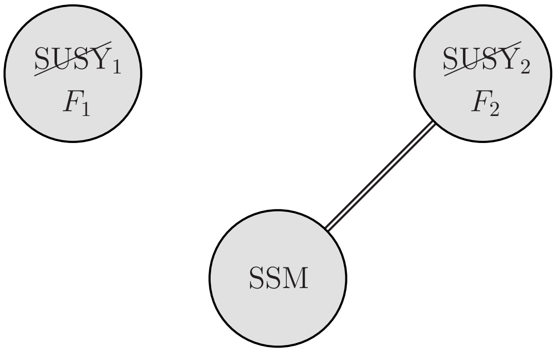

Figure 4.4: Minimal setup in which a standard SUSY breaking scheme (SSM + sector 2) is augmented by an additional sequestered sector which happens to break SUSY at some higher scale (sector 1).

the scalar–fermion–goldstino couplings, which are dimension 4 interactions. Since the strength of these interactions do not grow with temperature, the production of goldstinos through decays and scatterings involving SSM states is dominated by the infrared. Thus, the primary constraint from goldstino overproduction is a T_R-independent bound on the scalar–fermion–goldstino couplings.

As discussed in the Appendix, the leading contribution to goldstino production through scalar–fermion–goldstino vertices comes from superparticle decays. Since the relevant amplitudes scale with $1/F_2$, this sets a lower bound on $m_\zeta/F_2^2 \propto F_{\rm tot}/F_2^2$. The precise bound depends on the spectrum of superparticles (since the goldstino couplings depend on the superparticle masses), and for concreteness, we consider $m_{\tilde{Q}} = r m_{\tilde{L}}$ with $r = 3$ and 10, where $m_{\tilde{Q},\tilde{L}}$ are the squark and slepton masses taken, for simplicity, to be universal at the weak scale. These bounds are depicted in Figs. 4.2 and 4.3 as dotted lines, and given roughly by

$$\frac{F_2^2}{F_{\rm tot}} \gtrsim 10^{14}\ {\rm GeV}^2 \left(\frac{m_{\tilde{Q}}}{300\ {\rm GeV}}\right)^3. \tag{4.23}$$

4.5.2 The Minimal Goldstini Scenario

In the minimal goldstini scenario, the SSM couples directly to sector 2 but not to sector 1, so that $\tilde{m}_1^2$ and M_1 both vanish (see Fig. 4.4). This corresponds to a setup in which a standard SUSY breaking scheme (i.e. SSM + sector 2) is augmented by a single sequestered sector which happens to break SUSY at some higher scale (i.e. sector 1). Such constructions are expected to arise rather naturally from ultraviolet theories.

Since this minimal setup contains gauge–gaugino–goldstino vertices, the bound on the reheating temperature from Eq. (4.22) applies. Consequently, the scalar–fermion–goldstino couplings are important only when $T_R^{\rm max}$ is close to the SSM superparticle

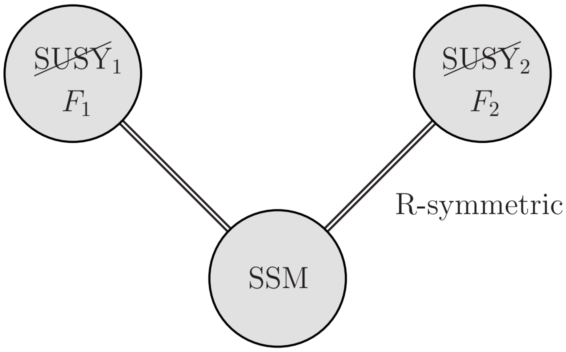

Figure 4.5: Setup in which both sector 1 and sector 2 couple directly to the SSM. By construction, couplings between sector 2 and the SSM are R symmetric, so gaugino masses arise solely from sector 1. For the same reason, the goldstino has suppressed couplings to gauginos.

masses, yielding $O(1)$ corrections to Eq. (4.22). For low enough T_R, only the T_R-independent bound from Eq. (4.23) is relevant, as depicted in Figs. 4.2 and 4.3.

When the bound of Eq. (4.22) is saturated, $T_R \approx T_R^{\max}$, the goldstino comprises all of the dark matter in the universe. The production is dominated by the ultraviolet and is thus sensitive to the value of T_R. Comparing Eq. (4.22) to the allowed regions in Figs. 4.2 and 4.3, we find that T_R as high as $\approx 10^7$ GeV (corresponding to $m_\zeta \simeq \text{few} \times 10$ GeV, $F_2 \simeq \text{few} \times 10^9$ GeV) can be consistent with the BBN bound and the collider measurement of M_{Pl}. Such a high reheating temperature allows for high temperature mechanisms for baryogenesis that would otherwise not work with $T_R \lesssim m_{\text{LOSP}}/20$, although it is still too low for thermal leptogenesis. Note that the gravitino abundance is small, $\Omega_{3/2} \approx (F_2/F_{\text{tot}})^2 \Omega_\zeta$, and that the goldstino energy density coming from late decays of the LOSP after LOSP freezeout is also typically subdominant.

4.5.3 SUSY Breaking with R Symmetries

Copious production of goldstinos at very high temperatures is not inevitable. In particular, since the bound on the reheating temperature Eq. (4.22) is wholly determined by the goldstino couplings to the gauginos, it can be evaded by imposing an R symmetry. This allows for an alternative cosmological scenario with non-thermal gravitino dark matter.

Consider the setup depicted in Fig. 4.5, where sector 2 preserves an R symmetry. In this case, the sfermion masses receive a contribution from sector 2, $\tilde{m}_2^2 \neq 0$, but not the gaugino masses, $M_2 = 0$. Sector 1, which does not preserve an R symmetry, generates both $\tilde{m}_1^2$ and M_1. For simplicity, we consider that the resulting sfermion and gaugino masses are of the same order, which can easily happen if $\tilde{m}_2^2$ is not much larger than M_1^2. Our analysis below assumes that the dominant contribution to the sfermion masses comes from sector 2, although the existence of a comparable contribution from sector 1 does not change our essential conclusions.

In this R-symmetric setup, the bound from goldstino overproduction is quite mild because the goldstino couples very weakly to the gauginos. The only relevant interactions are the scalar–fermion–goldstino couplings, so we need only consider the T_R-independent bound from Eq. (4.23) which are shown in Figs. 4.2 and 4.3. It is interesting that this cosmological bound leads to a lower limit on the branching fraction $\Gamma_{\tilde{\ell}\to\ell\tilde{G}}/\Gamma_{\tilde{\ell}\to\ell\zeta} \gtrsim O(10^{-5})$, which favors the possibility of observing both $\tilde{G}$ and ζ at the LHC.

Since the coupling strength of the gauginos to the goldstino is a factor of F_2/F_1 weaker than to the gravitino in the present setup, the constraint from goldstino overproduction through these couplings is weaker than that from gravitino overproduction. From Figs. 4.2 and 4.3, parameter regions we are interested in are roughly $F_2 \sim 10^9$ GeV and $F_{\rm tot} \approx F_1 \sim 10^{10}$ GeV. The bound on T_R from gravitino overproduction in these parameter regions is rather weak [70, 133]

$$T_R^{\rm max} \approx O(10^8 - 10^{10}\ {\rm GeV}), \tag{4.24}$$

so that it can even be compatible with thermal leptogenesis, which typically requires $T_R \gtrsim 10^9$ GeV. If the bound of Eq. (4.24) is saturated, we have gravitino dark matter.

Note that in conventional SUSY breaking scenarios, gravitino dark matter with a high reheating temperature such as in Eq. (4.24) is not possible, due to stringent constraints from BBN. In our case, however, the LOSP decays to the goldstino faster than to the gravitino as long as $\tilde{m}_2^2/F_2$ is sufficiently large. This allows us to evade the BBN bound consistently with gravitino dark matter and thermal leptogenesis.

4.5.4 Late Decay Case

So far, we have assumed that the relic density of goldstinos arising from late LOSP decays is small. This is true in most of the natural parameter regions, but in certain corners of parameter space, goldstinos from late LOSP decays may saturate the observed dark matter abundance.

Suppose that the slepton freezeout abundance is completely controlled by annihilation into gauge bosons (which will be the case if the neutralinos and heavy Higgs bosons are sufficiently heavier than the slepton). In this case, the yield of the (mostly right-handed) slepton before its decay is given by $Y_{\tilde{\ell}} \simeq 2\times 10^{-13}(m_{\tilde{\ell}}/100\ {\rm GeV})$ [139]. This leads to the goldstino relic abundance

$$\Omega_\zeta \simeq 0.2 \left(\frac{m_\zeta}{200\ {\rm GeV}}\right)\left(\frac{m_{\tilde{\ell}}}{1\ {\rm TeV}}\right), \tag{4.25}$$

so that if the slepton is very heavy, dark matter goldstinos may mostly come from late slepton decays. Such heavy sleptons, however, may be problematic for LHC measurements.

4.6 Other LOSPs

In the previous discussion, we have considered the case where the LOSP is a (mostly right-handed) charged slepton. In this section, we briefly discuss other possibilities.

To achieve the signatures discussed in this paper, there must be a quasi-stable charged state which is stopped either in the main detector or in a stopper detector. This immediately eliminates the possibility of a (mostly) bino LOSP. Similarly, wino, Higgsino or left-handed slepton LOSPs typically do not lead to the relevant signatures, since a mass splitting between the charged and neutral components (induced by radiative corrections, tree-level mixings, or the D-term effect) are so large that the charged component decays with lifetime shorter than $\approx 10^{-6}$ sec (see however [140]). With the constraint from overproduction in Sec. 4.5.1, the branching fraction of a charged component to the goldstino is then tiny, $\lesssim 10^{-6}$.

This leaves only the possibility of a gluino or squark LOSP. In the early universe these states freeze out at a temperature of $O(0.1 m_{\rm LOSP})$, with an abundance determined by perturbative strong interaction processes, $Y_{\rm LOSP,pert} \approx 10^{-13}(m_{\rm LOSP}/1~{\rm TeV})$. For the gluino $\tilde{g}$, this abundance will be reduced significantly by nonperturbative annihilations occurring after the QCD phase transition, $Y_{\tilde{g}} \approx 10^{-20}(m_{\tilde{g}}/1~{\rm TeV})^{1/2}$ [141]. On the other hand, for squarks $\tilde{q}$, nonperturbative processes lead to a significant fraction of $\tilde{q}\tilde{q}\tilde{q}$ bound states, which are not subject to enhanced annihilations. Therefore, the squark abundance may not be much reduced from the perturbative value, $Y_{\tilde{q}} \approx O(10^{-14} - 10^{-13})(m_{\tilde{q}}/1~{\rm TeV})$.

With the relic abundance given above, the gluino LOSP does not suffer from the BBN constraint.[1] On the other hand, squark LOSPs are subject to the BBN constraint coming from hadronic energy injections; conservatively it is $\tau_{\tilde{q}} \lesssim 100$ sec [142]. For a fixed LOSP mass, the constraint from goldstino overproduction can be weaker for gluino/squark LOSPs than for slepton LOSPs, since the masses of colored superparticles, which mainly control the goldstino abundance, can be smaller. A conservative constraint is given by Eq. (4.23) with $m_{\tilde{Q}}$ replaced by $m_{\rm LOSP}$, which corresponds to taking $r \simeq 1$.

Gluino/squark LOSPs can be produced at the LHC either directly or through decays of heavier superparticles. After being produced, they hadronize by picking up a gluon g or up/down quarks $q = u, d$. For the gluino, the relevant bound states are $\tilde{g}g$, $\tilde{g}\bar{q}q$, and $\tilde{g}qqq$. While the precise spectrum of bound states is not obvious, a fraction of gluinos is stopped in the detector under reasonable assumptions [143], allowing for gluino decay measurements (assuming that tracks can be reconstructed despite charge oscillation). The mass of the gluino can also be measured using charged gluino bound states traversing the muon system. The measurement of the Planck scale will thus

---

[1] This implies that if the gluino is the LOSP, the collider measurement of $M_{\rm Pl}$ can be consistent with the BBN bound even in the conventional SUSY framework. The measurement of gluino decays will be discussed below.

be feasible for the gluino LOSP. The situation for squark LOSPs is similar, where the relevant bound states are $\tilde{q}\bar{q}$ and $\tilde{q}qq$.

The visible decay products of gluino/squark LOSPs are jets, with an energy resolution expected to be $\mathit{\Delta}_E \approx O(1\%)$. Therefore, to be able to perform the measurements discussed in this paper, the masses of the gravitino and goldstino must be larger than $\approx O(0.1) m_{\rm LOSP}$; see Eq. (4.5).

In summary, the parameter regions in which the goldstino/gravitino collider signals are obtained consistently with high reheating temperatures (i.e. satisfying both the BBN and overproduction constraints) are

$$\tau_{\tilde{g}} \gtrsim \tau_{\rm min}, \qquad m_{3/2} \gtrsim O(0.1) m_{\rm LOSP}, \tag{4.26}$$

for a gluino LOSP, and

$$\tau_{\rm min} \lesssim \tau_{\tilde{q}} \lesssim 100 \text{ sec}, \qquad m_{3/2} \gtrsim O(0.1) m_{\rm LOSP}, \tag{4.27}$$

for a squark LOSP. Here,

$$\tau_{\rm min} = 0.2 \text{ sec} \left(\frac{300 \text{ GeV}}{m_{\rm LOSP}} \right) \left(\frac{m_{3/2}/m_{\rm LOSP}}{0.1} \right), \tag{4.28}$$

is obtained by translating Eq. (4.23) into a bound on LOSP lifetimes ignoring the phase space factor, which, however, would become important when $m_\zeta \approx m_{\rm LOSP}$.

4.7 Conclusions

The LHC may offer an unprecedented opportunity to probe the fundamental structure of spacetime at colliders. In particular, if the LOSP is charged, then precision measurements of its decays to the gravitino could provide a genuine collider measurement of $M_{\rm Pl}$ and a dramatic confirmation of SUGRA. Unfortunately, this decay process is directly constrained by BBN in the early universe. Thus, there must be some modification of the conventional SUSY framework to allow for high reheat temperatures $T_R \gtrsim$ TeV to be consistent with collider probes of SUGRA.

In this paper, we have shown that the goldstini framework introduced in Ref. [134] provides precisely such a modification. Multiple sources of SUSY breaking yield a corresponding multiplicity of goldstini which can easily couple more strongly to the SSM than the gravitino. Thus, the LOSP decays to goldstini fast enough to avoid the BBN bound, while the gravitino mass can still be measured in colliders via the LOSP decay to the gravitino. In fact, the regions in parameter space where this occurs are favored by cosmology.

Intriguingly, within this setup colliders will first measure the LOSP decay to the goldstino. Initially, this will almost certainly be interpreted as a LOSP decay to a gravitino, which will in turn result in a mismeasurement of $M_{\rm Pl}$ (one or two orders of magnitude below the value obtained from long-distance gravity). As we have shown, the degree of the discrepancy actually fixes the LOSP branching ratio into the gravitino, and hence the amount of integrated luminosity needed to discover the gravitino. Once this target luminosity is reached, our framework can be tested unambiguously. In particular, one may measure the masses of both the gravitino and goldstino, and if these satisfy $m_\zeta = 2m_{3/2}$ as predicted in Ref. [134], then this would provide a smoking gun signature of the goldstini setup. Specifically, we would learn not only that SUGRA is a symmetry of nature, but also that SUSY is broken multiple times and that sequestering is a real phenomenon. This would in turn suggest the existence of compact extra dimensions in which sequestering naturally emerges.

The scenarios described here are consistent with standard cosmology with high reheating temperatures. In particular, if the sector giving the goldstino preserves an R symmetry, then the bound from goldstino overproduction does not lead to an extra constraint on T_R beyond that from gravitino overproduction. This allows for thermal leptogenesis with LSP (gravitino) dark matter, which is not possible in the standard SUSY framework with R-parity.

Bibliography

[1] For a review see G. Bertone, D. Hooper, J. Silk, Phys. Rept. **405**, 279-390 (2005). [hep-ph/0404175].

[2] J. Mardon, Y. Nomura, D. Stolarski, J. Thaler, JCAP **0905**, 016 (2009). [arXiv:0901.2926 [hep-ph]].

[3] J. Mardon, Y. Nomura, J. Thaler, Phys. Rev. **D80**, 035013 (2009). [arXiv:0905.3749 [hep-ph]].

[4] C. Cheung, J. Mardon, Y. Nomura, J. Thaler, JHEP **1007**, 035 (2010). [arXiv:1004.4637 [hep-ph]].

[5] O. Adriani *et al.* [PAMELA Collaboration], Nature **458**, 607 (2009) [arXiv:0810.4995 [astro-ph]].

[6] J. Chang *et al.*, Nature **456**, 362 (2008).

[7] See, for example, D. Hooper, P. Blasi and P. D. Serpico, arXiv:0810.1527 [astro-ph]; H. Yüksel, M. D. Kistler and T. Stanev, arXiv:0810.2784 [astro-ph]; S. Profumo, arXiv:0812.4457 [astro-ph]; K. Ioka, arXiv:0812.4851 [astro-ph]; H- B. Hu, Q. Yuan, B. Wang, C. Fan, J.-L. Zhang and X.-J. Bi, arXiv:0901.1520 [astro-ph].

[8] See, for example, P.-f. Yin, Q. Yuan, J. Liu, J. Zhang, X.-j. Bi, S.-h. Zhu and X. Zhang, arXiv:0811.0176 [hep-ph]; C.-R. Chen, M. M. Nojiri, F. Takahashi and T. T. Yanagida, arXiv:0811.3357 [astro-ph]; E. Nardi, F. Sannino and A. Strumia, arXiv:0811.4153 [hep-ph]; K. Ishiwata, S. Matsumoto and T. Moroi, arXiv:0811.4492 [astro-ph]; arXiv:0811.0250 [hep-ph]; A. Arvanitaki, S. Dimopoulos, S. Dubovsky, P. W. Graham, R. Harnik and S. Rajendran, arXiv:0812.2075 [hep-ph]; K. Hamaguchi, S. Shirai and T. T. Yanagida, arXiv:0812.2374 [hep-ph]; F. Takahashi and E. Komatsu, arXiv:0901.1915 [astro-ph].

[9] See, for example, M. Cirelli, M. Kadastik, M. Raidal and A. Strumia, Nucl. Phys. B **813**, 1 (2009) [arXiv:0809.2409 [hep-ph]].

[10] N. Arkani-Hamed, D. P. Finkbeiner, T. Slatyer and N. Weiner, arXiv:0810.0713 [hep-ph].

[11] Y. Nomura and J. Thaler, arXiv:0810.5397 [hep-ph].

[12] I. Cholis, G. Dobler, D. P. Finkbeiner, L. Goodenough and N. Weiner, arXiv:0811.3641 [astro-ph].

[13] See, for example, M. Fairbairn and J. Zupan, arXiv:0810.4147 [hep-ph]; A. E. Nelson and C. Spitzer, arXiv:0810.5167 [hep-ph]; R. Harnik and G. D. Kribs, arXiv:0810.5557 [hep-ph]; Y. Bai and Z. Han, arXiv:0811.0387 [hep-ph]; P. J. Fox and E. Poppitz, arXiv:0811.0399 [hep-ph]; K. M. Zurek, arXiv:0811.4429 [hep-ph]; E. J. Chun and J. C. Park, arXiv:0812.0308 [hep-ph]; R. Allahverdi, B. Dutta, K. Richardson-McDaniel and Y. Santoso, arXiv:0812.2196 [hep-ph]; D. Hooper, A. Stebbins and K. M. Zurek, arXiv:0812.3202 [hep-ph]; C.-R. Chen, K. Hamaguchi, M. M. Nojiri, F. Takahashi and S. Torii, arXiv:0812.4200 [astro-ph]; I. Gogoladze, R. Khalid, Q. Shafi and H. Yüksel, arXiv:0901.0923 [hep-ph].

[14] D. P. Finkbeiner, Astrophys. J. **614**, 186 (2004) [arXiv:astro-ph/0311547]; G. Dobler and D. P. Finkbeiner, Astrophys. J. **680**, 1222 (2008) [arXiv:0712.1038 [astro-ph]].

[15] D. P. Finkbeiner, arXiv:astro-ph/0409027; D. Hooper, D. P. Finkbeiner and G. Dobler, Phys. Rev. D **76**, 083012 (2007) [arXiv:0705.3655 [astro-ph]].

[16] I. Cholis, L. Goodenough and N. Weiner, arXiv:0802.2922 [astro-ph].

[17] J. Zhang, X.-j. Bi, J. Liu, S.-M. Liu, P.-f. Yin, Q. Yuan and S.-h. Zhu, arXiv:0812.0522 [astro-ph].

[18] N. F. Bell and T. D. Jacques, arXiv:0811.0821 [astro-ph].

[19] G. Bertone, M. Cirelli, A. Strumia and M. Taoso, arXiv:0811.3744 [astro-ph].

[20] L. Bergström, G. Bertone, T. Bringmann, J. Edsjö and M. Taoso, arXiv:0812.3895 [astro-ph].

[21] J. Hisano, M. Kawasaki, K. Kohri and K. Nakayama, arXiv:0812.0219 [hep-ph].

[22] J. Liu, P.-f. Yin and S.-h. Zhu, arXiv:0812.0964 [astro-ph].

[23] O. Adriani *et al.* [PAMELA Collaboration], Phys. Rev. Lett. **102**, 051101 (2009) [arXiv:0810.4994 [astro-ph]].

[24] F. Aharonian *et al.*, Phys. Rev. Lett. **97**, 221102 (2006) [Erratum-ibid. **97**, 249901 (2006)] [arXiv:astro-ph/0610509].

[25] F. Aharonian *et al.*, Nature **439**, 695 (2006) [arXiv:astro-ph/0603021].

[26] F. Aharonian *et al.*, Astropart. Phys. **29**, 55 (2008) [arXiv:0711.2369 [astro-ph]].

[27] J. Hisano, S. Matsumoto and M. M. Nojiri, Phys. Rev. Lett. **92**, 031303 (2004) [arXiv:hep-ph/0307216]; J. Hisano, S. Matsumoto, M. M. Nojiri and O. Saito, Phys. Rev. D **71**, 063528 (2005) [arXiv:hep-ph/0412403]; M. Cirelli, A. Strumia and M. Tamburini, Nucl. Phys. B **787**, 152 (2007) [arXiv:0706.4071 [hep-ph]]; J. March-Russell, S. M. West, D. Cumberbatch and D. Hooper, JHEP **0807**, 058 (2008) [arXiv:0801.3440 [hep-ph]]; M. Lattanzi and J. Silk, arXiv:0812.0360 [astro-ph].

[28] M. Pospelov and A. Ritz, arXiv:0810.1502 [hep-ph]; J. March-Russell and S. M. West, arXiv:0812.0559 [astro-ph]; W. Shepherd, T. M. P. Tait and G. Zaharijas, arXiv:0901.2125 [hep-ph].

[29] S. Desai *et al.* [Super-Kamiokande Collaboration], Phys. Rev. D **70**, 083523 (2004) [Erratum-ibid. D **70**, 109901 (2004)] [arXiv:hep-ex/0404025].

[30] M. Pospelov, A. Ritz and M. Voloshin, Phys. Lett. B **662**, 53 (2008) [arXiv:0711.4866 [hep-ph]].

[31] D. P. Finkbeiner and N. Weiner, Phys. Rev. D **76**, 083519 (2007) [arXiv:astro-ph/0702587].

[32] P. Picozza *et al.*, Astropart. Phys. **27**, 296 (2007) [arXiv:astro-ph/0608697].

[33] T. G. Guzik *et al.*, Adv. Space Res. **33**, 1763 (2004).

[34] T. Delahaye, R. Lineros, F. Donato, N. Fornengo and P. Salati, Phys. Rev. D **77**, 063527 (2008) [arXiv:0712.2312 [astro-ph]].

[35] J. N. Bahcall and R. M. Soneira, Astrophys. J. Suppl. **44**, 73 (1980).

[36] J. F. Navarro, C. S. Frenk and S. D. M. White, Astrophys. J. **490**, 493 (1997) [arXiv:astro-ph/9611107].

[37] J. F. Navarro *et al.*, Mon. Not. Roy. Astron. Soc. **349**, 1039 (2004) [arXiv:astro-ph/0311231].

[38] J. Hisano, S. Matsumoto, O. Saito and M. Senami, Phys. Rev. D **73**, 055004 (2006) [arXiv:hep-ph/0511118].

[39] J. Lavalle, J. Pochon, P. Salati and R. Taillet, arXiv:astro-ph/0603796.

[40] I. V. Moskalenko and A. W. Strong, Astrophys. J. **493**, 694 (1998) [arXiv:astro-ph/9710124], as parameterized in E. A. Baltz and J. Edsjö, Phys. Rev. D **59**, 023511 (1999) [arXiv:astro-ph/9808243].

[41] High Energy Stereoscopic System (H.E.S.S.), `http://www.mpi-hd.mpg.de/hfm/HESS/`

[42] F. Aharonian *et al.*, Phys. Rev. Lett. **101**, 261104 (2008) [arXiv:0811.3894 [astro-ph]].

[43] A. Birkedal, K. T. Matchev, M. Perelstein and A. Spray, arXiv:hep-ph/0507194.

[44] G. D. Mack, T. D. Jacques, J. F. Beacom, N. F. Bell and H. Yüksel, Phys. Rev. D **78**, 063542 (2008) [arXiv:0803.0157 [astro-ph]].

[45] N. W. Evans, F. Ferrer and S. Sarkar, Phys. Rev. D **69**, 123501 (2004) [arXiv:astro-ph/0311145].

[46] R. D. Davies, D. Walsh and R. S. Booth, Mon. Not. Roy. Astron. Soc. **177**, 319 (1976).

[47] A. A. Dutton, F. C. van den Bosch, A. Dekel and S. Courteau, Astrophys. J. **654**, 27 (2006) [arXiv:astro-ph/0604553].

[48] D. Merritt, M. Milosavljević, L. Verde and R. Jimenez, Phys. Rev. Lett. **88**, 191301 (2002) [arXiv:astro-ph/0201376].

[49] J. Diemand, M. Kuhlen, P. Madau, M. Zemp, B. Moore, D. Potter and J. Stadel, arXiv:0805.1244 [astro-ph]; J. F. Navarro *et al.*, arXiv:0810.1522 [astro-ph].

[50] E. Borriello, A. Cuoco and G. Miele, arXiv:0809.2990 [astro-ph]; arXiv:0812.2932 [astro-ph].

[51] A. de Oliveira-Costa, M. Tegmark, B. M. Gaensler, J. Jonas, T. L. Landecker and P. Reich, arXiv:0802.1525 [astro-ph].

[52] S. Ritz and D. Seckel, Nucl. Phys. B **304**, 877 (1988).

[53] C. Amsler *et al.* [Particle Data Group], Phys. Lett. B **667**, 1 (2008).

[54] V. Barger, W.-Y. Keung, G. Shaughnessy and A. Tregre, Phys. Rev. D **76**, 095008 (2007) [arXiv:0708.1325 [hep-ph]].

[55] H. L. Lai *et al.*, Eur. Phys. J. C **12**, 375 (2000) [arXiv:hep-ph/9903282].

[56] S. Fukuda *et al.*, Nucl. Instrum. Meth. A **501**, 418 (2003).

[57] S. Desai, private communication.

[58] M. Kamionkowski and S. Profumo, Phys. Rev. Lett. **101**, 261301 (2008) [arXiv:0810.3233 [astro-ph]].

[59] Y. B. Zel'dovich, A. A. Klypin, M. Y. Khlopov and V. M. Chechetkin, Sov. J. Nucl. Phys. **31**, 664 (1980) [Yad. Fiz. **31**, 1286 (1980)].

[60] E. Aslanides *et al.*, arXiv:astro-ph/9907432.

[61] J. Ahrens *et al.*, Astropart. Phys. **20**, 507 (2004) [arXiv:astro-ph/0305196].

[62] A. Kappes, arXiv:0711.0563 [astro-ph].

[63] J. Buckley *et al.*, arXiv:0810.0444 [astro-ph].

[64] Fermi Gamma-ray Space Telescope (formerly GLAST), `http://fermi.gsfc.nasa.gov/`

[65] P. Meade, M. Papucci and T. Volansky, arXiv:0901.2925 [hep-ph].

[66] Y. Kuno and Y. Okada, Rev. Mod. Phys. **73**, 151 (2001) [arXiv:hep-ph/9909265].

[67] G. G. Raffelt, Phys. Rept. **198**, 1 (1990).

[68] S. Weinberg, Phys. Rev. Lett. **48**, 1303 (1982); M. Y. Khlopov and A. D. Linde, Phys. Lett. B **138** (1984) 265; M. Kawasaki, K. Kohri, T. Moroi and A. Yotsuyanagi, Phys. Rev. D **78**, 065011 (2008) [arXiv:0804.3745 [hep-ph]].

[69] G. D. Coughlan, W. Fischler, E. W. Kolb, S. Raby and G. G. Ross, Phys. Lett. B **131**, 59 (1983); T. Banks, D. B. Kaplan and A. E. Nelson, Phys. Rev. D **49**, 779 (1994) [arXiv:hep-ph/9308292].

[70] T. Moroi, H. Murayama and M. Yamaguchi, Phys. Lett. B **303**, 289 (1993).

[71] M. Kawasaki, F. Takahashi and T. T. Yanagida, Phys. Lett. B **638**, 8 (2006) [arXiv:hep-ph/0603265]; Phys. Rev. D **74**, 043519 (2006) [arXiv:hep-ph/0605297].

[72] H. Pagels and J. R. Primack, Phys. Rev. Lett. **48**, 223 (1982).

[73] M. Viel, J. Lesgourgues, M. G. Haehnelt, S. Matarrese and A. Riotto, Phys. Rev. D **71**, 063534 (2005) [arXiv:astro-ph/0501562].

[74] M. Fukugita and T. Yanagida, Phys. Lett. B **174**, 45 (1986).

[75] M. Dine and W. Fischler, Phys. Lett. B **110**, 227 (1982); Nucl. Phys. B **204**, 346 (1982); L. Alvarez-Gaumé, M. Claudson and M. B. Wise, Nucl. Phys. B **207**, 96 (1982); S. Dimopoulos and S. Raby, Nucl. Phys. B **219**, 479 (1983).

[76] M. Dine, A. E. Nelson and Y. Shirman, Phys. Rev. D **51**, 1362 (1995) [arXiv:hep-ph/9408384]; M. Dine, A. E. Nelson, Y. Nir and Y. Shirman, Phys. Rev. D **53**, 2658 (1996) [arXiv:hep-ph/9507378].

[77] C. Csáki, A. Falkowski, Y. Nomura and T. Volansky, Phys. Rev. Lett. **102**, 111801 (2009) [arXiv:0809.4492 [hep-ph]].

[78] Z. Komargodski and N. Seiberg, JHEP **0903**, 072 (2009) [arXiv:0812.3900 [hep-ph]].

[79] H. P. Nilles, M. Srednicki and D. Wyler, Phys. Lett. B **120**, 346 (1983); J.-M. Frère, D. R. T. Jones and S. Raby, Nucl. Phys. B **222**, 11 (1983); J.-P. Derendinger and C. A. Savoy, Nucl. Phys. B **237**, 307 (1984).

[80] S. Dimopoulos, G. F. Giudice and A. Pomarol, Phys. Lett. B **389**, 37 (1996) [arXiv:hep-ph/9607225]; Y. Nomura and B. Tweedie, Phys. Rev. D **72**, 015006 (2005) [arXiv:hep-ph/0504246]; K. Hamaguchi, S. Shirai and T. T. Yanagida, Phys. Lett. B **654**, 110 (2007) [arXiv:0707.2463 [hep-ph]].

[81] A. E. Nelson and N. Seiberg, Nucl. Phys. B **416**, 46 (1994) [arXiv:hep-ph/9309299].

[82] J. Bagger, E. Poppitz and L. Randall, Nucl. Phys. B **426**, 3 (1994) [arXiv:hep-ph/9405345].

[83] I. Cholis, L. Goodenough and N. Weiner, arXiv:0802.2922 [astro-ph]; N. Arkani-Hamed, D. P. Finkbeiner, T. R. Slatyer and N. Weiner, Phys. Rev. D **79**, 015014 (2009) [arXiv:0810.0713 [hep-ph]].

[84] X. Chen, arXiv:0902.0008 [hep-ph].

[85] E. Nardi, F. Sannino and A. Strumia, JCAP **0901**, 043 (2009) [arXiv:0811.4153 [hep-ph]]; A. Arvanitaki, S. Dimopoulos, S. Dubovsky, P. W. Graham, R. Harnik and S. Rajendran, arXiv:0812.2075 [hep-ph], and references therein.

[86] A. A. Abdo *et al.* [The Fermi LAT Collaboration], arXiv:0905.0025 [astro-ph.HE].

[87] F. Aharonian *et al.* [H.E.S.S. Collaboration], arXiv:0905.0105 [astro-ph.HE].

[88] H.-S. Goh and M. Ibe, JHEP **0903**, 049 (2009) [arXiv:0810.5773 [hep-ph]].

[89] P. Meade, N. Seiberg and D. Shih, arXiv:0801.3278 [hep-ph].

[90] S. Dimopoulos, M. Dine, S. Raby and S. D. Thomas, Phys. Rev. Lett. **76**, 3494 (1996) [arXiv:hep-ph/9601367].

[91] E. Witten, Nucl. Phys. B **188**, 513 (1981).

[92] K. Hamaguchi, E. Nakamura, S. Shirai and T. T. Yanagida, arXiv:0811.0737 [hep-ph].

[93] J. L. Jones, arXiv:0812.2106 [hep-ph].

[94] M. A. Luty, Phys. Rev. D **57**, 1531 (1998) [arXiv:hep-ph/9706235]; A. G. Cohen, D. B. Kaplan and A. E. Nelson, Phys. Lett. B **412**, 301 (1997) [arXiv:hep-ph/9706275].

[95] M. Dine, W. Fischler and M. Srednicki, Phys. Lett. B **104**, 199 (1981); A. P. Zhitnitskiĭ, Sov. J. Nucl. Phys. **31**, 260 (1980) [Yad. Fiz. **31**, 497 (1980)].

[96] L. J. Hall and T. Watari, Phys. Rev. D **70**, 115001 (2004) [arXiv:hep-ph/0405109].

[97] I. Antoniadis and T. N. Truong, Phys. Lett. B **109**, 67 (1982).

[98] V. V. Anisimovsky *et al.* [E949 Collaboration], Phys. Rev. Lett. **93**, 031801 (2004) [arXiv:hep-ex/0403036]; S. Adler *et al.* [E787 Collaboration], Phys. Rev. Lett. **88**, 041803 (2002) [arXiv:hep-ex/0111091].

[99] H. K. Park *et al.* [HyperCP Collaboration], Phys. Rev. Lett. **88**, 111801 (2002) [arXiv:hep-ex/0110033].

[100] B. Aubert *et al.* [BABAR Collaboration], arXiv:0905.4539 [hep-ex].

[101] W. Love *et al.* [CLEO Collaboration], Phys. Rev. Lett. **101**, 151802 (2008) [arXiv:0807.1427 [hep-ex]].

[102] F. Bergsma *et al.* [CHARM Collaboration], Phys. Lett. B **157**, 458 (1985).

[103] M. Altmann, Y. Declais, F. v. Feilitzsch, C. Hagner, E. Kajfasz, and L. Oberauer, Z. Phys. C **68**, 221 (1995).

[104] J. Engel, D. Seckel and A. C. Hayes, Phys. Rev. Lett. **65**, 960 (1990); E. L. Chupp, W. T. Vestrand and C. Reppin, Phys. Rev. Lett. **62**, 505 (1989).

[105] For a review, G. F. Giudice and R. Rattazzi, Phys. Rept. **322**, 419 (1999) [arXiv:hep-ph/9801271].

[106] For a review, K. Intriligator and N. Seiberg, Nucl. Phys. Proc. Suppl. **45BC**, 1 (1996) [arXiv:hep-th/9509066].

[107] K. Griest and D. Seckel, Phys. Rev. D **43**, 3191 (1991).

[108] K.-I. Izawa, F. Takahashi, T. T. Yanagida and K. Yonekura, arXiv:0902.3854 [hep-th].

[109] Z. Komargodski and D. Shih, JHEP **0904**, 093 (2009) [arXiv:0902.0030 [hep-th]].

[110] K.-I. Izawa, Y. Nomura, K. Tobe and T. Yanagida, Phys. Rev. D **56**, 2886 (1997) [arXiv:hep-ph/9705228].

[111] A. Arvanitaki, S. Dimopoulos, S. Dubovsky, P. W. Graham, R. Harnik and S. Rajendran, in Ref. [85]; S. Bailly, K. Jedamzik and G. Moultaka, arXiv:0812.0788 [hep-ph], and references therein.

[112] J. Chang *et al.* [ATIC Collaboration], Nature **456**, 362 (2008).

[113] S. Torii *et al.* [PPB-BETS Collaboration], arXiv:0809.0760 [astro-ph].

[114] See, for example, S. Profumo, arXiv:0812.4457 [astro-ph].

[115] See, for example, L. Bergström, J. Edsjö and G. Zaharijas, arXiv:0905.0333 [astro-ph.HE]; D. Grasso *et al.*, arXiv:0905.0636 [astro-ph.HE].

[116] P. Meade, M. Papucci, A. Strumia and T. Volansky, arXiv:0905.0480 [hep-ph].

[117] M. Ibe, Y. Nakayama, H. Murayama and T. T. Yanagida, arXiv:0902.2914 [hep-ph].

[118] T. Banks and J.-F. Fortin, arXiv:0901.3578 [hep-ph]; T. Banks, J. D. Mason and D. O'Neil, Phys. Rev. D **72**, 043530 (2005) [arXiv:hep-ph/0506015].

[119] See, for example, G. Bertone, M. Cirelli, A. Strumia and M. Taoso, JCAP **0903**, 009 (2009) [arXiv:0811.3744 [astro-ph]]; P. Meade, M. Papucci and T. Volansky, arXiv:0901.2925 [hep-ph].

[120] T. Sjöstrand, P. Edén, C. Friberg, L. Lönnblad, G. Miu, S. Mrenna and E. Norrbin, Comput. Phys. Commun. **135**, 238 (2001) [arXiv:hep-ph/0010017]; T. Sjöstrand, S. Mrenna and P. Skands, Comput. Phys. Commun. **178**, 852 (2008) [arXiv:0710.3820 [hep-ph]].

[121] E. A. Baltz *et al.* [GLAST-LAT Collaboration], JCAP **0807**, 013 (2008) [arXiv:0806.2911 [astro-ph]].

[122] M. Regis and P. Ullio, arXiv:0904.4645 [astro-ph.GA].

[123] L. Bergström, P. Ullio and J. H. Buckley, Astropart. Phys. **9**, 137 (1998) [arXiv:astro-ph/9712318].

[124] M. Lisanti and J. G. Wacker, arXiv:0903.1377 [hep-ph].

[125] V. M. Abazov *et al.* [DØ Collaboration], arXiv:0905.3381 [hep-ex].

[126] B. Batell, M. Pospelov and A. Ritz, arXiv:0903.0363 [hep-ph]; R. Essig, P. Schuster and N. Toro, arXiv:0903.3941 [hep-ph]; P.-f. Yin, J. Liu and S.-h. Zhu, arXiv:0904.4644 [hep-ph].

[127] M. Reece and L.-T. Wang, arXiv:0904.1743 [hep-ph].

[128] D. B. Kaplan and H. Georgi, Phys. Lett. B **136**, 183 (1984); N. Arkani-Hamed, A. G. Cohen and H. Georgi, Phys. Lett. B **513**, 232 (2001) [arXiv:hep-ph/0105239]; R. Contino, Y. Nomura and A. Pomarol, Nucl. Phys. B **671**, 148 (2003) [arXiv:hep-ph/0306259].

[129] W. Buchmüller, K. Hamaguchi, M. Ratz and T. Yanagida, Phys. Lett. B **588**, 90 (2004) [arXiv:hep-ph/0402179].

[130] K. Hamaguchi, M. M. Nojiri and A. de Roeck, JHEP **03**, 046 (2007) [arXiv:hep-ph/0612060].

[131] M. Y. Khlopov and A. D. Linde, Phys. Lett. B **138**, 265 (1984); J. Ellis, J. E. Kim and D. V. Nanopoulos, Phys. Lett. B **145**, 181 (1984).

[132] M. Kawasaki, K. Kohri, T. Moroi and A. Yotsuyanagi, Phys. Rev. D **78**, 065011 (2008) [arXiv:0804.3745 [hep-ph]].

[133] V. S. Rychkov and A. Strumia, Phys. Rev. D **75**, 075011 (2007) [arXiv:hep-ph/0701104].

[134] C. Cheung, Y. Nomura and J. Thaler, JHEP **03**, 073 (2010) [arXiv:1002.1967 [hep-ph]].

[135] I. Hinchliffe and F. E. Paige, Phys. Rev. D **60**, 095002 (1999) [arXiv:hep-ph/9812233]; S. Ambrosanio, B. Mele, S. Petrarca, G. Polesello and A. Rimoldi, JHEP **01**, 014 (2001) [arXiv:hep-ph/0010081]; J. R. Ellis, A. R. Raklev and O. K. Øye, JHEP **10**, 061 (2006) [arXiv:hep-ph/0607261].

[136] S. Asai, K. Hamaguchi and S. Shirai, Phys. Rev. Lett. **103**, 141803 (2009) [arXiv:0902.3754 [hep-ph]]; CMS Collaboration, http://cms-physics.web.cern.ch/cms-physics/public/EXO-09-001-pas.pdf

[137] K. Hamaguchi, Y. Kuno, T. Nakaya and M. M. Nojiri, Phys. Rev. D **70**, 115007 (2004) [arXiv:hep-ph/0409248]; J. L. Feng and B. T. Smith, Phys. Rev. D **71**, 015004 (2005) [Erratum-ibid. D **71**, 0109904 (2005)] [arXiv:hep-ph/0409278].

[138] ATLAS Collaboration, *ATLAS Physics TDR*, http://atlas.web.cern.ch/Atlas/GROUPS/PHYSICS/TDR/TDR.html; CMS Collaboration, *CMS Physics TDR*, http://cmsdoc.cern.ch/cms/cpt/tdr/index.html

[139] C. F. Berger, L. Covi, S. Kraml and F. Palorini, JCAP **10**, 005 (2008) [arXiv:0807.0211 [hep-ph]].

[140] G. D. Kribs, A. Martin and T. S. Roy, JHEP **01**, 023 (2009) [arXiv:0807.4936 [hep-ph]].

[141] J. Kang, M. A. Luty and S. Nasri, JHEP **09**, 086 (2008) [arXiv:hep-ph/0611322].

[142] M. Kawasaki, K. Kohri and T. Moroi, Phys. Rev. D **71**, 083502 (2005) [arXiv:astro-ph/0408426].

[143] A. Arvanitaki, S. Dimopoulos, A. Pierce, S. Rajendran and J. G. Wacker, Phys. Rev. D **76**, 055007 (2007) [arXiv:hep-ph/0506242].

[144] A. De Simone, M. Garny, A. Ibarra and C. Weniger, arXiv:1004.4890 [hep-ph].

Appendix A

Cascade Energy Spectra

In this appendix, we present formulae for the energy spectra used in the text. In general, the energy spectra of final state particles in cascade annihilations are functions of all the intermediate masses and helicities. In the limit of large mass hierarchies and scalar decays, however, the energy spectra greatly simplify, and we use these simplified formulae in our analysis.

Consider cascading fields ϕ_i of mass m_i ($m_{i+1} > 2m_i$) and a final state ψ with mass m_ψ. Cascade annihilation occurs through $\phi_{i+1} \to \phi_i\phi_i$ ($i = 1, 2, \cdots$), and in the last stage, ϕ_1 decays into $\psi + X$. Let the energy of ψ in the ϕ_1 rest frame be E_0. Defining

$$x_0 = \frac{2E_0}{m_1}, \qquad \epsilon_0 = \frac{2m_\psi}{m_1}, \tag{A.1}$$

the ψ energy spectrum is a function of x_0 and ϵ_0

$$\frac{d\tilde{N}_\psi}{dx_0} = \frac{d\tilde{N}_\psi}{dx_0}(x_0, \epsilon_0), \tag{A.2}$$

where $\epsilon_0 \leq x_0 \leq 1$. In the case where dark matter χ annihilates directly into $\psi + X$, we can regard ϕ_1 as the initial state of dark matter annihilation, $\chi\chi$. In this case $d\tilde{N}_\psi/dx_0$ is the primary injection spectrum with $m_1 = 2m_{\rm DM}$.

Now consider the previous step in the cascade annihilation, $\phi_2 \to \phi_1\phi_1$, with *one of the* ϕ_1 decaying into $\psi + X$. Let the energy of ψ in the ϕ_2 rest frame be E_1 and define

$$x_1 = \frac{2E_1}{m_2}, \qquad \epsilon_1 = \frac{2m_1}{m_2}. \tag{A.3}$$

Assuming isotropic scalar decays, the ψ energy spectrum in the ϕ_2 rest frame is

$$\frac{d\tilde{N}_\psi}{dx_1} = \int_{-1}^{1} d\cos\theta \int_{\epsilon_0}^{1} dx_0\, \frac{d\tilde{N}_\psi}{dx_0}\, \delta\left(2x_1 - x_0 - \cos\theta\sqrt{x_0^2 - \epsilon_0^2}\sqrt{1-\epsilon_1^2}\right), \tag{A.4}$$

where θ is the angle between the ψ momentum and the ϕ_1 boost axis as measured in the ϕ_1 rest frame.

Equation (A.4) is complicated to solve in general, but in the limit $\epsilon_i \to 0$ ($i = 0, 1, \cdots$), it reduces to a simple convolution:

$$\frac{d\tilde{N}_\psi}{dx_1} = \int_{x_1}^{1} \frac{dx_0}{x_0} \frac{d\tilde{N}_\psi}{dx_0} + \mathcal{O}(\epsilon_i^2), \tag{A.5}$$

where $0 \le x_1 \le 1$ up to $\mathcal{O}(\epsilon_i^2)$ effects. This convolution can be iterated as many times as necessary to build up the desired energy spectrum for an n-step cascade decay:

$$\frac{d\tilde{N}_\psi}{dx_n} = \int_{x_n}^{1} \frac{dx_{n-1}}{x_{n-1}} \frac{d\tilde{N}_\psi}{dx_{n-1}} + \mathcal{O}(\epsilon_i^2), \tag{A.6}$$

where $x_{n-1} = 2E_{n-1}/m_n$ with E_{n-1} being the energy of ψ in the ϕ_n rest frame, and $0 \le x_n \le 1$ up to $\mathcal{O}(\epsilon_i^2)$ effects. Note that we here adopt the normalization convention of

$$\int_0^1 dx_n \frac{d\tilde{N}_\psi}{dx_n} = 1, \tag{A.7}$$

regardless of the value of n, so that the injection spectra per dark matter annihilation must be multiplied by the multiplicity of ψ in the final state.

A.0.1 Direct electron spectra

Here we derive the spectra of electrons/positrons arising directly from ϕ_1 decay, $\phi_1 \to e^+e^-$ (or dark matter annihilation, $\chi\chi \to e^+e^-$). Ignoring the effect of final state radiation to smooth the spectrum, the electron energy spectrum is given by

$$\frac{d\tilde{N}_e}{dx_0} = \delta(1 - x_0), \tag{A.8}$$

where we have adopted the convention $\int_0^1 dx_0 \, \delta(1 - x_0) = 1$. The positron energy spectrum is identical.

Applying the simplified convolution formula in Eq. (A.6) for an n-step cascade annihilation, we then find

$$\frac{d\tilde{N}_e}{dx_1} = 1, \tag{A.9}$$

$$\frac{d\tilde{N}_e}{dx_2} = \ln\frac{1}{x_2}, \tag{A.10}$$

$$\frac{d\tilde{N}_e}{dx_n} = Q_n(x_n), \tag{A.11}$$

where we have defined

$$Q_n(x) \equiv \frac{1}{(n-1)!}\left(\ln\frac{1}{x}\right)^{n-1}. \tag{A.12}$$

Note that these are energy spectra for *one* of the electrons (or positrons), so that the electron (or positron) injection spectra per dark matter annihilation $\chi\chi \to 2\phi_n \to \cdots \to 2^n(e^+e^-)$ are

$$\frac{dN_e}{dx_n} = 2^n \frac{d\tilde{N}_e}{dx_n}, \tag{A.13}$$

where $x_n = E_e/m_{\rm DM}$ with E_e being the electron (positron) energy in the center-of-mass frame for dark matter annihilation. The direct annihilation case, $\chi\chi \to e^+e^-$, corresponds to $n = 0$.

A.0.2 Electron and neutrino spectra from muon decay

Here we discuss the spectra of electrons, positrons and neutrinos arising from muon decay. Consider $\phi_1 \to \mu^+\mu^-$ (or $\chi\chi \to \mu^+\mu^-$) followed by $\mu \to e\nu_e\nu_\mu$. (One of the neutrinos here should be an anti-neutrino. We omit the particle-antiparticle identification here and below.) Assuming a massless electron, the (unpolarized) spectra of electrons and neutrinos in the rest frame of the muon are

$$\frac{d\tilde{N}_{\mu\to e}}{dx_{-1}} = \frac{d\tilde{N}_{\mu\to\nu_\mu}}{dx_{-1}} = 6(x_{-1})^2 - 4(x_{-1})^3, \tag{A.14}$$

$$\frac{d\tilde{N}_{\mu\to\nu_e}}{dx_{-1}} = 12(x_{-1})^2 - 12(x_{-1})^3, \tag{A.15}$$

where we are using the notation $x_{-1} = 2E_{-1}/m_\mu$, with E_{-1} being the energy in the muon rest frame.

Applying the cascade convolution for electrons and muon neutrinos

$$\frac{d\tilde{N}_{\mu\to e}}{dx_0} = \frac{d\tilde{N}_{\mu\to\nu_\mu}}{dx_0} = \frac{5}{3} - 3x_0^2 + \frac{4}{3}x_0^3, \tag{A.16}$$

$$\frac{d\tilde{N}_{\mu\to e}}{dx_1} = \frac{d\tilde{N}_{\mu\to\nu_\mu}}{dx_1} = -\frac{19}{18} + \frac{3}{2}x_1^2 - \frac{4}{9}x_1^3 + \frac{5}{3}Q_2(x_1), \tag{A.17}$$

$$\frac{d\tilde{N}_{\mu\to e}}{dx_2} = \frac{d\tilde{N}_{\mu\to\nu_\mu}}{dx_2} = \frac{65}{108} - \frac{3}{4}x_2^2 + \frac{4}{27}x_2^3 - \frac{19}{18}Q_2(x_2) + \frac{5}{3}Q_3(x_2), \tag{A.18}$$

and for electron neutrinos

$$\frac{d\tilde{N}_{\mu\to\nu_e}}{dx_0} = 2 - 6x_0^2 + 4x_0^3, \tag{A.19}$$

$$\frac{d\tilde{N}_{\mu\to\nu_e}}{dx_1} = -\frac{5}{3} + 3x_1^2 - \frac{4}{3}x_1^3 + 2Q_2(x_1), \tag{A.20}$$

$$\frac{d\tilde{N}_{\mu\to\nu_e}}{dx_2} = \frac{19}{18} - \frac{3}{2}x_2^2 + \frac{4}{9}x_2^3 - \frac{5}{3}Q_2(x_2) + 2Q_3(x_2). \tag{A.21}$$

Again, these are energy spectra for *one* of the electrons, positrons or (anti-)neutrinos. To obtain the injection spectra per dark matter annihilation, we must multiply the multiplicity factor, 2^n for n-step, and set $x_n = E/m_{\rm DM}$. Here, E is the energy of a particle in the center-of-mass frame for dark matter annihilation.

For comparison, the corresponding formulae in the approximation of isotropic three-body decays are

$$\frac{d\tilde{N}_{\mu\to e}}{dx_{-1}} \simeq 2x_{-1}, \tag{A.22}$$

$$\frac{d\tilde{N}_{\mu\to e}}{dx_n} \simeq (-1)^{n+1}\left(2x_n + 2\sum_{i=1}^{n+1}(-1)^i Q_i(x_n)\right) \equiv \overline{Q}_{n+1}(x_n). \tag{A.23}$$

As a rough rule of thumb, the electron spectrum for an n-step muon cascade has a shape between $(n+1)$- and $(n+2)$-step electron cascades.

A.0.3 Gamma ray spectra from final state radiation

Primary gamma rays come from final state radiation in the decay $\phi_1 \to \ell^+\ell^-\gamma$. In principle, one could do an exact calculation to $\mathcal{O}(\alpha_{\rm EM})$ of the gamma ray spectrum, which would have the full $\epsilon_0 \equiv 2m_\ell/m_1$ dependence. Since we are using the simplified convolution formula in Eq. (A.6), it is not consistent to keep $\mathcal{O}(\epsilon_0^2)$ corrections in the exact gamma ray calculation, and it suffices to use twice the Altarelli-Parisi splitting formula

$$\frac{d\tilde{N}_\gamma}{dx_0} = \frac{\alpha_{\rm EM}}{\pi}\frac{1+(1-x_0)^2}{x_0}\left\{-1+\ln\left(\frac{4(1-x_0)}{\epsilon_0^2}\right)\right\}, \tag{A.24}$$

where the normalization of $\tilde{N}_\gamma$ is such that $\int dx_n\, d\tilde{N}_\gamma/dx_n$ gives the (average) number of photons per ϕ_1 decay. Note that the expression of Eq. (A.24) becomes negative at $x_0 > 1 - e\,\epsilon_0^2/4$, which does not correspond to the kinematic threshold. The error from this, however, is formally an $\mathcal{O}(\epsilon_0^2)$ effect.

Applying the simplified convolution formula, we obtain

$$\frac{d\tilde{N}_\gamma}{dx_1} = \frac{\alpha_{\rm EM}}{\pi}\frac{1}{x_1}\left\{\left(-1+\ln\frac{4}{\epsilon_0^2}\right)R_1(x_1) + S_1(x_1)\right\}, \tag{A.25}$$

$$\frac{d\tilde{N}_\gamma}{dx_2} = \frac{\alpha_{\rm EM}}{\pi}\frac{1}{x_2}\left\{\left(-1+\ln\frac{4}{\epsilon_0^2}\right)R_2(x_2) + S_2(x_2)\right\}, \tag{A.26}$$

where

$$\begin{aligned} R_1(x) &= 2 - x - x^2 + 2x\ln x, && \text{(A.27)}\\ R_2(x) &= 2 - 3x + x^2 + x\ln x - x(\ln x)^2, && \text{(A.28)}\\ S_1(x) &= \left(\frac{\pi^2}{3} - 1\right)x + x^2 + 2x\ln x + (2 - x - x^2)\ln(1-x) - 2x\,\mathrm{Li}_2(x), && \text{(A.29)}\\ S_2(x) &= \left(\frac{\pi^2}{6} + 2 - 2\zeta(3)\right)x - 2x^2 - \left(\frac{\pi^2}{3} - 3\right)x\ln x + (2 - 3x + x^2)\ln(1-x)\\ &\quad -x(\ln x)^2 - x\,\mathrm{Li}_2(x) + 2x\,\mathrm{Li}_3(x). && \text{(A.30)} \end{aligned}$$

The photon injection spectra *per dark matter annihilation* are then given by

$$\frac{dN_\gamma}{dx_n} = 2^n\,\frac{d\tilde{N}_\gamma}{dx_n}, \tag{A.31}$$

where $x_n = E_\gamma/m_{\mathrm{DM}}$, with E_γ being the photon energy in the center-of-mass frame for dark matter annihilation. Here, $\epsilon_0 = m_\ell/m_{\mathrm{DM}}$ for direct annihilation and $\epsilon_0 = 2m_\ell/m_1$ otherwise.

For the hardest gamma rays near $x_n \to 1$, the behavior of $d\tilde{N}_\gamma/dx_n$ is

$$\begin{aligned} \frac{d\tilde{N}_\gamma}{dx_0} &\simeq \frac{\alpha_{\mathrm{EM}}}{\pi}\frac{1}{x_0}\ln\left(\frac{4(1-x_0)}{\epsilon_0^2}\right), && \text{(A.32)}\\ \frac{d\tilde{N}_\gamma}{dx_1} &\simeq \frac{\alpha_{\mathrm{EM}}}{\pi}\frac{1-x_1}{x_1}\ln\left(\frac{4(1-x_1)}{\epsilon_0^2}\right), && \text{(A.33)}\\ \frac{d\tilde{N}_\gamma}{dx_2} &\simeq \frac{\alpha_{\mathrm{EM}}}{\pi}\frac{(1-x_2)^2}{2x_2}\ln\left(\frac{4(1-x_2)}{\epsilon_0^2}\right). && \text{(A.34)} \end{aligned}$$

Compared to direct annihilation into leptons, a 1-step cascade annihilation gives a gamma ray spectrum that is suppressed not only by $\ln(2m_\ell/m_1)/\ln(m_\ell/m_{\mathrm{DM}})$ but also by an additional suppression factor of $(1-x)$ for the highest energy gamma rays.

A.0.4 Gamma ray subtlety for muons

There are actually two contributions to the gamma ray spectrum for $\phi_1 \to \mu^+\mu^-\gamma$. In addition to final state radiation from muons, there is the radiative decay of the muon $\mu \to e\nu_e\nu_\mu\gamma$. Formally, this contribution is suppressed by a factor of $1/\ln(m_\mu/m_1)$ or $(1-x_n)^2$, but for $m_1 \approx m_\mu$, it is an important effect.

The gamma ray spectrum in the muon rest frame is known in the limit that $r = m_e^2/m_\mu^2$ is small [66]. Assuming unpolarized muons, we can derive the 0-step cascade annihilation spectrum from the muon rest frame spectrum

$$\frac{d\tilde{N}_{\mu\to\gamma}}{dx_{-1}} = \frac{\alpha_{\rm EM}}{3\pi}\frac{1}{x_{-1}}\left(T_{-1}(x_{-1})\ln\frac{1}{r} + U_{-1}(x_{-1})\right), \tag{A.35}$$

$$\frac{d\tilde{N}_{\mu\to\gamma}}{dx_{0}} = \frac{\alpha_{\rm EM}}{3\pi}\frac{1}{x_{0}}\left(T_{0}(x_{0})\ln\frac{1}{r} + U_{0}(x_{0})\right), \tag{A.36}$$

where

$$T_{-1}(x) = (1-x)(3-2x+4x^2-2x^3), \tag{A.37}$$

$$T_0(x) = 3+\frac{2}{3}x-6x^2+3x^3-\frac{2}{3}x^4+5x\ln x, \tag{A.38}$$

$$U_{-1}(x) = (1-x)\left(-\frac{17}{2}+\frac{23}{6}x-\frac{101}{12}x^2+\frac{55}{12}x^3+(3-2x+4x^2-2x^3)\ln(1-x)\right) \tag{A.39}$$

$$U_0(x) = -\frac{17}{2}-\frac{3}{2}x+\frac{191}{12}x^2-\frac{23}{3}x^3+\frac{7}{4}x^4+\left(3+\frac{2}{3}x-6x^2+3x^3-\frac{2}{3}x^4\right)\ln(1-x)$$
$$-\frac{28}{3}x\ln x+5x\ln(1-x)\ln x+5x\,{\rm Li}_2(1-x). \tag{A.40}$$

The convolutions for 1- and 2-step decays are straightforward to derive.

Note again that $\int dx_n\, d\tilde{N}_{\mu\to\gamma}/dx_n$ give the (average) number of photons per muon decay. The photon spectra from radiative muon decay *per dark matter annihilation* are then given by $2^n d\tilde{N}_{\mu\to\gamma}/dx_n$. The total photon injection spectra per dark matter annihilation are given by

$$\frac{dN_\gamma}{dx_n} = 2^n\left(\frac{d\tilde{N}_\gamma}{dx_n}+2\frac{d\tilde{N}_{\mu\to\gamma}}{dx_n}\right), \tag{A.41}$$

where $x_n = E_\gamma/m_{\rm DM}$, with E_γ being the photon energy in the center-of-mass frame for dark matter annihilation.

A.0.5 Rare modes in the axion portal

In Section 2.6, we consider bounds on rare $a\to\gamma\gamma$ and $a\to\pi^+\pi^-\pi^0$ decay modes in axion portal models. The axion portal has both a 1-step and a 2-step component, and the gamma ray spectrum for each can be calculated straightforwardly. The $a\to\gamma\gamma$ spectra are identical (up to normalization) to the $\phi_1\to e^+e^-$ spectra already calculated:

$$\frac{d\tilde{N}_{a\to\gamma}}{dx_1} = 2, \tag{A.42}$$

$$\frac{d\tilde{N}_{a\to\gamma}}{dx_2} = 2\ln\frac{1}{x_2}, \tag{A.43}$$

where the normalization of $\tilde{N}_{a\to\gamma}$ is such that $\int dx_n\, d\tilde{N}_{a\to\gamma}/dx_n$ gives the number of photons per a decay.

For $a \to \pi^+\pi^-\pi^0$ followed by $\pi^0 \to \gamma\gamma$, we can use the $\overline{Q}_n$ function from Eq. (A.23) if we assume that $m_a \gg m_\pi$ and that the $a \to 3\pi$ decay is isotropic:

$$\frac{d\tilde{N}_{a\to\pi^0\to\gamma}}{dx_1} \simeq 2\overline{Q}_2(x_1), \tag{A.44}$$

$$\frac{d\tilde{N}_{a\to\pi^0\to\gamma}}{dx_2} \simeq 2\overline{Q}_3(x_2), \tag{A.45}$$

where again the normalization of $\tilde{N}_{a\to\pi^0\to\gamma}$ is such that $\int dx_n\, d\tilde{N}_{a\to\pi^0\to\gamma}/dx_n$ gives the number of photons per a decay. One should keep in mind that $m_a \simeq 3m_\pi$ in the region of interest, but the hierarchical cascade approximation is still reasonably representative of the true energy spectrum.

Appendix B

Leptonic Axion Portal

In the minimal axion portal construction, the axion has large hadronic couplings, and is therefore strongly constrained by beam dump and rare meson decay experiments. In particular, the axion is forced to decay primarily into muons, and, as we saw in Section 2.5, there is some degree of tension between a muon annihilation scenario and the absence of galactic neutrinos. Also, we saw in Section 2.6 that there are strong gamma ray bounds on the $a \to \pi^+\pi^-\pi^0$ decay mode, which in the minimal axion portal arises from axion-pion mixing.

Since the decay properties of the axion are irrelevant for dark matter freezeout, we can easily modify the couplings of the axion to standard model fields without losing the good features of this scenario. In particular, we can construct a leptonic axion portal model where the axion has no hadronic couplings. While such a leptonic axion could decay into muons as in the minimal axion portal, in the text we consider the less constrained case where the leptonic axion decays primarily into electrons.

The simplest example for the leptonic axion portal can be constructed as follows. Vector-like fermion dark matter ψ/ψ^c obtains a mass from spontaneous symmetry breaking through the vacuum expectation value of a complex scalar S_ℓ:

$$\mathcal{L} = -\xi S_\ell \psi \psi^c + \text{h.c.}, \qquad S_\ell = \left(f_a + \frac{s_\ell}{\sqrt{2}} \right) e^{i a_\ell / \sqrt{2} f_a}, \tag{B.1}$$

where a_ℓ is the pseudoscalar axion, s_ℓ is a light scalar, and f_a is the axion decay constant, which is assumed to be of order TeV. As in the minimal axion portal, the masses of s_ℓ and a_ℓ can be considered as free parameters. In order for a_ℓ to decay into leptons, S_ℓ must be charged under a leptonic symmetry (which is softly broken to give a mass to a_ℓ). This requires introducing separate electron-type and neutrino-type Higgses:

$$\mathcal{L} = -\lambda_e \ell h_e e^c - \lambda_\nu \ell h_\nu \nu^c - A_\ell S_\ell h_e h_\nu + \text{h.c.} \tag{B.2}$$

These interactions force the standard model leptons to carry axial leptonic charges. (Small neutrino masses can be obtained through the standard see-saw mechanism, and it is straightforward to extend the model to incorporate supersymmetry.)

In order to eliminate the hadronic couplings of a_ℓ, the standard model quarks are assumed not to carry charges under the leptonic symmetry. This requires introducing one or more new Higgses for the quark sector, which must also be singlets under the leptonic symmetry. As long as the potential for these Higgses preserves the leptonic symmetry, then a_ℓ will have no hadronic couplings and cannot mix with the neutral mesons after the leptonic symmetry is spontaneously broken.

The absence of hadronic couplings allows m_{a_ℓ} to be lighter than $2m_\mu$, and thus a_ℓ to decay dominantly into electrons while satisfying beam dump and rare meson decay constraints. Also, the leptonic axion a_ℓ has no $a_\ell \to \pi^+\pi^-\pi^0$ decay mode, reducing the gamma ray constraints in the case that $m_{a_\ell} > 3m_\pi$ (where a_ℓ dominantly decays into muons). Since the strongest astrophysical bounds on light degrees of freedom come from hadronic couplings [67], m_{a_ℓ} might even be as light as $2m_e$, although a detailed study of the constraints on the leptonic axion is beyond the scope of this chapter.

As an example of the quark sector interactions, there could be separate up-type and down-type Higgses. In this case, it is natural to assume a hadronic symmetry under which the quarks carry axial charges:

$$\mathcal{L} = -\lambda_u q h_u u^c - \lambda_d q h_d d^c - A_q S_q h_u h_d + \text{h.c.} \tag{B.3}$$

The axion contained in the field S_q could then be the QCD axion and solve the strong CP problem. To avoid astrophysical constraints, however, the vacuum expectation value of S_q must be $\gtrsim 10^{10}$ GeV, much larger than $\langle S_\ell \rangle = O(\text{TeV})$. Explicit breaking of the hadronic symmetry must also be much smaller than that of the leptonic symmetry.

Appendix C

Infrared-Dominated Goldstino Production

The late-time goldstino yield can be computed with a standard Boltzmann equation calculation. The yield is defined as $Y_\zeta \equiv n_\zeta / s$, where n_ζ is the goldstino number density and s is the total entropy density, and is constant once goldstino production is completed. There are three potentially relevant goldstino production mechanisms: superparticle decays and $2 \to 2$ scattering processes in the early thermal bath, and late decays of relic LOSPs after LOSP freezeout. If the goldstino does not couple to gauge multiplets, as occurs in the R-symmetric setup described in Sec. 4.5.3, then the goldstino production is dominated by scalar decays at $T \sim \tilde{m}$, and is insensitive to T_R. This is in contrast to the standard gravitino production calculation [70], where the goldstino abundance grows linearly with T_R.

Here, we briefly describe the calculation of the contribution from superparticle decays in this scenario. The contribution from $2 \to 2$ scattering can be calculated in a similar (but more involved) manner, but we find it to be subdominant and omit it from our analysis. The contribution from late LOSP decays can be taken directly from the LOSP freezeout abundance used to determine the BBN bound [132]. For a slepton LOSP, for example, $Y_\zeta^{(\mathrm{LOSP-decay})} = 7 \times 10^{-14} (m_{\tilde{\ell}}/100\text{ GeV})$, which is not significant unless $m_{\tilde{\ell}} \gtrsim 700$ GeV.

The goldstino yield from decays in the thermal bath is found by solving the Boltzmann equation:

$$\dot{n}_\zeta + 3 H n_\zeta = \sum_i n_i \left\langle \frac{1}{\gamma} \right\rangle_i \Gamma_{i \to \zeta}, \tag{C.1}$$

where dots indicate derivatives with respect to time, the sum is over unstable species, n_i and $\Gamma_{i \to \zeta}$ are their number densities and decay rates to goldstinos, and $\langle 1/\gamma \rangle$ is the thermally averaged relativistic time-dilation factor to account for out-of-rest-frame decay rates. Using the fact that the entropy per comoving volume is constant, we have the relations

$$\dot{Y}_\zeta = \frac{1}{s}\left(\dot{n}_\zeta + 3Hn_\zeta\right), \tag{C.2}$$

and

$$\frac{dt}{dT} = -\frac{1}{HT}\left(1 + \frac{1}{3}\frac{d\log g_S(T)}{d\log T}\right), \tag{C.3}$$

where T is temperature and $g_S(T)$ is the effective number of relativistic species. The goldstino yield is thus

$$Y_\zeta = \int_{T_R}^{0} dT \frac{dt}{dT}\dot{Y}_\zeta. \tag{C.4}$$

For concreteness, we assume the simple spectrum $m = m_{\rm LOSP}$ for non-colored particles and $m = rm_{\rm LOSP}$ for colored particles, with r a free parameter. Squark decays dominate the production process, with a decay width

$$\Gamma_{\tilde{Q}\to Q\zeta} \simeq \frac{1}{16\pi}\frac{m_{\tilde{Q}}^5}{F_2^2}. \tag{C.5}$$

Parametrically, for decays

$$\dot{Y}_\zeta^{\rm decay} \simeq \frac{m_{\tilde{Q}}^5}{F_2^2}\theta(T - m_{\tilde{Q}}), \qquad \frac{dt}{dT} \sim -\frac{M_{\rm Pl}}{T^3}. \tag{C.6}$$

Solving the Boltzmann equations numerically, keeping the full temperature dependence, we find:

$$Y_\zeta^{\rm decay} \approx 0.0013\frac{M_{\rm Pl}r^3m_{\rm LOSP}^3}{F_2^2}. \tag{C.7}$$

Here, we show only the leading order dependence on F_1, F_2 and r, but we keep the full dependence in Figs. 4.2 and 4.3. The goldstino overabundance bound is set by requiring $m_\zeta Y_\zeta < 3.8 \times 10^{-10}$ GeV [53], so that the goldstino abundance is not in conflict with the observed dark matter density.